Dynamic Stall on Airfoils with Leading-Edge Tubercles

Characterization of the Dynamic Stall Vortex by Simulations and Experiments

Pere Valls Badia

Delft University of Technology

TU Delft

Dynamic Stall on Airfoils with Leading-Edge Tubercles

Characterization of the Dynamic Stall Vortex by Simulations and Experiments

by

Pere Valls Badia

to obtain the degree of Master of Science
at the Delft University of Technology,
to be defended publicly on Thursday May 23, 2024 at 9:30 AM.

Student number:	5457408
Thesis supervisors:	Dr. M. Li
	Dr. Ir. F. Scarano
Institution:	Delft University of Technology
Place:	Faculty of Aerospace Engineering, Delft

An electronic version of this thesis is available at `http://repository.tudelft.nl/`.

TU Delft

Abstract

Inspired by the leading-edge protuberances found on the flippers of humpback whales, tubercles have drawn significant interest for improving airfoil aerodynamic performance. In static conditions, airfoils with tubercles exhibit a softer onset of stall and increased lift in post-stall regime, though with a reduced maximum lift coefficient. However, their impact under dynamic conditions is less understood, particularly how they affect the formation and convection of the dynamic stall vortex (DSV), which is crucial to the dynamic stall process. Therefore, this study aims to investigate how tubercles affect the development and behavior of the DSV during dynamic stall conditions. To deliberately trigger the formation of the DSV and thereby force the airfoil into dynamic stall conditions, this study employed a pitch-up and hold motion starting at a zero angle of attack and increasing to final angles of 30 and 55 degrees. Two pitching rates of k=0.05 and 0.1 were investigated, providing a comprehensive analysis of how these conditions influence the aerodynamic characteristics of the airfoils across a wide range of dynamic stall scenarios.

To assess the impact of leading-edge tubercles on airfoil aerodynamics under dynamic stall conditions, a series of wind tunnel experiments was conducted, involving two tubercled airfoils and a smooth leading-edge airfoil. These experiments were performed at a Reynolds number Re=3.3×10^4, determined by the chord length and free-stream velocity. Employing particle tracking velocimetry (PTV), the velocity field on the suction side of each airfoil was measured, while ensuring precise airfoil positioning within the flow-field through the use of white tracking markers. Detailed monitoring of the DSV core location and circulation was conducted using the normalized angular momentum (NAM) criterion, also referred to as Γ_1 method. This approach provided quantitative insights into the influence of the tubercles on the DSV. Due to the experimental setup limitations in directly measuring aerodynamic forces, computational fluid dynamics (CFD) simulations were conducted using OpenFOAM. These simulations employed a sliding mesh technique, which facilitated the consistent application of the same computational framework for various tubercle geometries and pitching conditions. The accuracy and reliability of the simulations were rigorously validated against the experimental data.

The results reveal that leading-edge tubercles significantly influence the aerodynamic performance of airfoils under dynamic stall conditions. It has been found that tubercles modify the onset and severity of dynamic stall by reducing the strength of the DSV and shifting its formation closer to the trailing-edge. These changes result in a weaker and shorter lift overshoot, facilitating a quicker transition to the deep stall regime where tubercles enhance the lift provided by the airfoil. This alteration in the dynamic stall process has been consistently observed across all tested pitching motions, with the effects of the tubercles found to be proportional to their amplitude. These findings suggest that tubercles serve as dynamic stall mitigation devices, potentially benefiting applications where dynamic stall frequently occurs and can compromise structural integrity.

Preface

This report not only summarizes the work I have done over the last 9 months but also marks the final milestone in a long journey, representing the conclusion of my master's degree and my university education. With it, I fulfill the graduation requirements for the Master of Science in Aerospace Engineering at TU Delft.

First and foremost, I extend my heartfelt gratitude to my supervisors, Morgan and Fulvio, for their invaluable guidance. Their advice and continuous feedback were paramount in the progress and success of this work. Special appreciation also goes to Stefan for offering his support and expertise with the simulations. I was also privileged to have the assistance of all the technicians at the HSL. In particular, I want to thank Frits Donker Duyvis, Peter Duyndam, and Stefan Bernardy for their help in manufacturing the airfoil supports, setting up the test section, and implementing the LabView software, which was essential for the PTV measurements. A shout-out to Octavian for sharing those two long and stressful weeks of wind tunnel testing with me; we made it.

Thanks to my amazing friends here in Delft, not only for sharing the long hours in the faculty and library to meet those thesis deadlines, but more importantly, for all the moments we have spent together during these three years. From dinners at Foulkes to Bouwpub Thursdays, and the trip to Colombia, just to name a few, it's been a blast. Your friendship has truly made my time here unforgettable, and I couldn't be more thankful for it.

Als amics de Cabrera, moltes gràcies. Quina sort de tenir els amics que tinc! A la meva família, mil gràcies. Mama, papa, Júlia i Mariona, sou els millors. Gràcies per creure en mi, pel vostre suport incondicional i per animar-me a perseguir els meus somnis. Ho hem aconseguit i tot és gràcies a vosaltres.

Pere Valls Badia
Delft, May 2024

Contents

List of Figures

List of Tables

Nomenclature

Abbreviations

Abbreviation	Definition
BL	Boundary Layer
BSL	Baseline
CFD	Computational Fluid Dynamics
DSV	Dynamic Stall Vortex
FSU	Fluid Supply Unit
HFSB	Helium-Filled Soap Bubbles
LE	Leading-Edge
LES	Large Eddy Simulation
LEV	Leading Edge Vortex
LPT	Lagrangian Particle Tracking
LSB	Laminar Separation Bubble
MAVs	Micro Air Vehicles
MART	Multiplicative Algebraic Reconstruction Technique
MTV	Molecular Tagging Velocimetry
NACA	National Advisory Committee for Aeronautics
PIV	Particle Image Velocimetry
PLA	Polylactic Acid
PTU	Programmable Timing Unit
PTV	Particle Tracking Velocimetry
RANS	Reynolds-Averaged Navier–Stokes
SLV	Shear-Layer Vortex
STB	Shake-The-Box
TE	Trailing-Edge
URANS	Unsteady Reynolds-Averaged Navier–Stokes

Symbols

Symbol	Definition	Unit
c	Chord	[m]
$\overline{c}$	Mean aerodynamic chord	[m]
C_l	Lift coefficient	[−]
$C_{l,max}$	Maximum lift coefficient	[−]
C_p	Pressure coefficient	[−]
d_τ	Effective particle diameter	[m]
d_p	Physical particle diameter	[m]
d_{diff}	Particle diameter increase due to diffraction	[m]
f_{osc}	Frequency of the oscillation	[Hz]
$f_\#$	F number	[−]
k	Reduced frequency	[−]
k_{turb}	Turbulence kinetic energy	[m^2/s^2]
M	Magnification factor	[−]
p_k	Kinematic pressure	[m^2/s^2]
r_{core}	DSV core radius	[m]
R_w	Waviness ratio	[−]
Re	Reynolds number	[−]
$t_{upstroke}$	Upstroke pause	[s]
t^*	Normalized convective time tU_∞/c	[−]
U_x	Velocity in x direction	[m/s]
U_∞	Freestream Velocity	[m/s]
V	Velocity in y direction	[m/s]
W	Velocity in z direction	[m/s]
$x_{_{AF}}/c$	x coordinate in airfoil frame of reference	[m]
$y_{_{AF}}/c$	y coordinate in airfoil frame of reference	[m]
α	Angle of attack	[deg]
α_0	Mean angle of the oscillation	[deg]
α_1	Amplitude of the oscillation	[deg]
α_{ss}	Static stall angle of attack	[deg]
$\dot{\alpha}$	Pitch rate (angular velocity)	[deg/s]
Γ_{const}	DSV circulation computed with constant area	[m^2/s]
Γ_{core}	DSV circulation computed with core size	[m^2/s]
Γ_1	Normalized angular momentum (NAM) criterion	[-]
λ	Tubercles wavelength	[m]
λ^*	Distance between consecutive stall cells	[m]
μ	Dynamic viscosity coefficient	[kg/ms]
τ_w	Wall shear stress	[kg/ms^2]
ω	Turbulence specific dissipation rate	[1/s]
ω_x	Streamwise vorticity	[1/s]
ω_z	Spanwise vorticity	[1/s]

1

Introduction

Tubercles, a passive flow control device inspired by the unique protuberances along the leading-edge of humpback whale (*Megaptera novaeangliae*) flippers, serve as a compelling example of biomimicry in aerodynamics. Despite reaching lengths of up to 19 meters and weights exceeding 53 tons, humpback whales demonstrate exceptional agility, executing incredibly tight underwater maneuvers during their feeding routines. This remarkable maneuverability is attributed to the hydrodynamic advantages provided by the leading-edge tubercles, a feature not observed in other whale species.

Studies on airfoils under static conditions have shown that tubercles significantly alter aerodynamic performance, softening stall evolution, reducing maximum lift, and improving post-stall performance compared to smooth leading-edge counterparts. These alterations have been associated with counter-rotating streamwise vortices generated by the tubercles, which are believed to enhance boundary layer mixing and compartmentalize flow separation regions in stall cells.

Recent observations of humpback whales in their natural habitat have revealed that these whales perform rapid movements with their flippers during lunging maneuvers toward prey. The frequencies of these flapping strokes clearly fall within the realm of unsteady aerodynamics, suggesting that tubercles may exert a more significant effect under dynamic stall conditions. This unsteady aerodynamic phenomenon occurs when rapid changes in the angle of attack lead to the formation of a leading-edge vortex, known as the dynamic stall vortex (DSV), which temporarily boosts the airfoil's lift due to the low-pressure core of the vortex. This observation represents a paradigm shift, suggesting that examining tubercles solely under static conditions may not fully capture their benefits, as they may also play a significant role in the development of the dynamic stall phenomenon.

1.1. Research scope

The flow mechanisms induced by tubercles on airfoils under static conditions are well-established. In the context of dynamic stall, it is broadly agreed that the emergence of the DSV precedes the onset of dynamic stall and significantly contributes to subsequent lift overshoot. However, the effects of tubercles on the DSV and the overall dynamic stall process remain less understood. Upon examination of the available research, two main research gaps have been identified:

- **Effects of tubercles on dynamic stall:** The role of tubercles as either lift enhancement or dynamic stall mitigation devices is still uncertain. Most research in this field has focused on airfoils subjected to sinusoidal pitching oscillations near the static stall angle of attack, with findings typically suggesting that tubercles reduce both the lift peak and hysteresis, thus acting as dynamic stall mitigation devices. However, observations made by Segre et al. (2017) of humpback whales performing lunging maneuvers suggest that tubercled flippers may actually enhance lift, rather than mitigating dynamic stall. Supporting this hypothesis, Hrynuk and Bohl (2020) found out that tubercles delay the formation of the DSV at higher angles of attack and increase its circulation, also indicating that tubercles might act as lift enhancement devices.

- **Flowfield characteristics of tubercled airfoils in dynamic stall:** Although the flow mechanisms of tubercles under static conditions have been thoroughly elucidated through computation fluid dynamics (CFD) and wind tunnel experiments, extending this knowledge to the dynamic regime remains a challenge. Available research on dynamic stall with tubercled airfoils heavily relies on CFD, with most efforts aimed at characterizing the temporal evolution of unsteady aerodynamic forces, particularly the effects on lift overshoot and hysteresis. Consequently, little attention has been given to the flowfield itself. It is unclear whether the counter-rotating streamwise vortices generated by the tubercles persist during rapid pitching motions or how they impact the DSV in dynamic stall conditions. While Hrynuk and Bohl (2020) provides a comprehensive flowfield analysis for an airfoil with tubercles, measurements are limited to two planes aligned with a trough and a peak, assuming without empirical evidence that these planes represent the flow behavior along the entire airfoil span. Additionally, limiting the flowfield measurements to only two planes restricts understanding of the flow during deep stall conditions.

In this context, the objective of this research can be defined as:

> **Explore the influence of leading-edge tubercles on the aerodynamic performance of airfoils during dynamic stall. This investigation will involve a DSV characterization utilizing particle tracking velocimetry and computational fluid dynamics.**

1.2. Research methodology

This thesis adopts a dual approach to investigate the aerodynamic effects of leading-edge tubercles on airfoils undergoing dynamic stall. The methodology combines experimental wind tunnel tests with CFD simulations, providing a comprehensive analysis of this unsteady phenomenon.

A novel aspect of this research is the use of the Shake-the-box (STB) particle tracking velocimetry (PTV) technique to characterize the flowfield, a method not previously applied to tubercled airfoils under dynamic conditions. This advanced technique enables the acquisition of time-resolved, three-dimensional flowfield data during the dynamic stall cycle of the airfoil. During the experiments, a specially designed airfoil pitching system, comprising an actuator and an encoder has been used. The actuator facilitated precise control over the airfoil's motion, while the encoder monitored the airfoil's angle of attack. This setup initiated PTV measurements at the beginning of the pitch-up phase, ensuring phase-locked data acquisition.

The experimental setup, however, did not facilitate the direct measurement of aerodynamic forces. To bridge this gap, CFD simulations have been developed to complement the experimental data, offering a temporal analysis of lift throughout the airfoil's motion. These simulations have also enhanced the understanding of the flowfield, providing superior resolution and enabling the computation of the pressure field, which is not achievable through experimental means alone.

Collectively, these methodologies establish a robust framework for exploring the dynamic stall behavior of tubercled airfoils. This approach integrates direct experimental observations with detailed theoretical predictions derived from CFD analyses. Based on this integrated methodology, the main research questions and subsequent sub-questions are presented.

1. **How do tubercles affect the dynamic stall phenomenon?**
   - 1.1. Do tubercles delay the formation of the DSV?
   - 1.2. Do tubercles affect the strength of the DSV?
   - 1.3. Do tubercles alter the convection of the DSV?
2. **Is the stall compartmentalization mechanism still observable under dynamic stall conditions?**
3. **What is the impact of the tubercle amplitude on dynamic stall mitigation?**

1.3. Report outline

Chapter 2 reviews existing literature, setting the theoretical foundation for this research. It begins by introducing the topic of dynamic stall and explores its impact on the aerodynamic performance of airfoils. This chapter then delves into the concept of leading-edge tubercles, discussing their morphology and analyzing the associated flow physics, and concludes with the impact of tubercles on airfoils during dynamic stall. Following this, Chapter 3 describes the experimental setup and numerical simulations used for data collection and analysis, providing a detailed overview of the methodologies employed in this research. Subsequently, Chapter 4 presents both experimental and simulation results, offering a comparative analysis to evaluate the impact of tubercles on aerodynamic performance during dynamic stall. Finally, Chapter 5 summarizes the findings, draws conclusions, and suggests recommendations for further research, effectively concluding the study.

2

Background

This chapter serves as a critical and comprehensive summary and analysis of existing research, peer-reviewed articles, and books which reflects the current status of the field of dynamic stall and leading-edge tubercles. It outlines the key themes, debates, and findings on both the steady and unsteady aerodynamics of the tubercles when used on airfoils and wings.

This chapter is organized into three main sections. Section 2.1 begins with an extensive overview of dynamic stall, delving into its effects on the lift characteristics of airfoils and discussing the factors that influence the unsteady aerodynamics associated with this aerodynamic phenomenon. Section 2.2 shifts focus to leading-edge tubercles, examining their morphology and effects on airfoil and wing aerodynamics. This section also explores the flow physics of tubercles, summarizing their impact on aerodynamic performance, particularly under static conditions. Finally, Section 2.3 discusses the influence of leading-edge tubercles on dynamic stall characteristics, noting that this is an area with limited existing research.

2.1. Dynamic stall

Dynamic stall is an unsteady aerodynamic phenomenon observed when an airfoil or wing experiences rapid alterations in its apparent angle of attack. It occurs when a lifting surface, such as an aircraft wing or rotor blade, abruptly alters its orientation, causing sudden disruptions in the steady flowfield around it. This dynamic change in apparent angle of attack leads to the formation of a strong and well defined leading-edge vortex known as dynamic stall vortex (DSV). The presence of this vortex has a notable effect on airfoil or wing performance, enhancing their maximum lift capabilities and delaying stall onset [Gendrich 1999]. For reference, Figure 2.1 showcases the formation and growth phases of the DSV for an airfoil pitching up at a constant rate.

Research has shown that the DSV lowers the pressure on the suction side of the airfoil which is known to increase the lift up to three times the static maximum while delaying the flow separation to angles of attack beyond the static angle of attack [Carr et al. 1977; Jumper et al. 1987; Gendrich 1999; Mulleners and Raffel 2013; Choudhry et al. 2014b]. However, it is important to note that this lift enhancement is transient because the DSV is eventually convected downstream inducing sudden variations in aerodynamic forces. As the DSV moves downstream closer to the trailing-edge, a strong nose-down pitching moment is induced which precipitously increases with the vortex getting closer to the trailing-edge. The lift coefficient reaches a maximum when the DSV is in the mid-chord position. Ultimately, the DSV moves away from the suction surface, and the lift is abruptly lost with the airfoil or wing entering in a deep stall regime.

Initial investigations of dynamic stall were focused on finding ways to alleviate or partially restrain the excessive lift and nose-down pitching moment caused by the DSV. Kramer (1932) first observed the unsteady phenomena linked to rapid changes in the angle of attack of an airfoil. Nevertheless, due to its limited applications at the time, little research in the dynamic stall field followed.

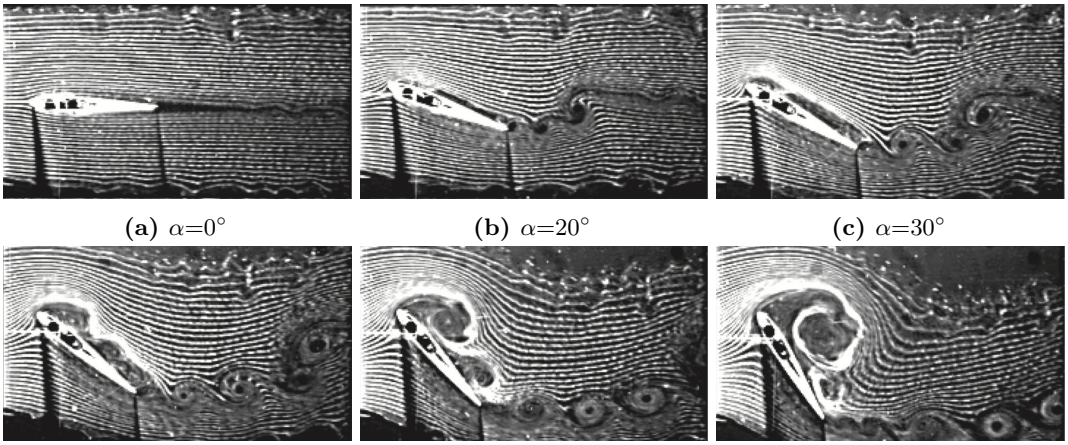

(a) α=0° **(b)** α=20° **(c)** α=30°

(d) α=40° **(e)** α=50° **(f)** α=60°

Figure 2.1: Airfoil pitching at k=0.1 and a freestream Reynolds number of 6700. Images extracted from [Choudhry et al. 2014b].

It wasn't until the late 1960s, when the problem was recognized on the retreating blades of helicopters, that dynamic stall regained focus. Significant regions of dynamic stall occur across the helicopter rotor disk during high-speed and maneuvering flights. When the rotor blades encounter dynamic stall conditions, there are notable increases in torsional stresses and rotor vibrations, leading to potentially fatal structural loads and also setting rigorous criteria for selecting the materials for the blade [Ham and Garelick 1968]. Since then, significant progress has been made towards understanding the dynamics stall process, and the flow mechanisms associated with rapidly pitching airfoils have been the subject of diverse experimental and numerical investigations [Carr et al. 1977; McCroskey 1981; Reynolds and Carr 1985]. More recently, research has also focused on mitigating the dynamic stall observed in wind turbines. Factors such as tower shadowing, upwind turbine wakes, yaw angles, and wind gusts can quickly change the angle of attack on the turbine blades, leading to the dynamic stall phenomenon. As a result, parts such as generators and blades often endure dynamic stresses well beyond their design limits, leading to excessive fatigue and potential failure, and thus resulting in elevated operational and maintenance expenses and eventually reducing the operating life of the wind turbines [Butterfield et al. 1991; Shipley et al. 1995].

In contrast to the earlier point of view, there is now an increasing research emphasis on effectively managing dynamic stall in order to optimize the additional lift that it offers. This is motivated by the exceptional performance of flapping flight observed in insects, certain birds, and bats, which often surpasses the capabilities of the most advanced human-made aircraft by a significant margin. As Shyy et al. (2007) point out in their book: "Birds can fly at 140 body lengths per second compared to the 32 body lengths per second of the Mach 3 SR-71 Blackbird and achieve roll rates far in excess of typical aerobatic aircraft". Because of this, extensive research has been conducted to comprehend this superiority and researchers have widely acknowledged that most insects, along with certain bird species, rely on generating a leading-edge vortex through dynamic stall during the flapping of their wings to achieve 2–3 times the amount of lift that conventional aerodynamics can explain [Ellington 1999]. A detailed image of the DSV along the leading-edge of a flapping bumble bee wing is presented in Figure 2.2. It is important to note that for larger insects, the average Reynolds number during hovering flight typically falls within the range of 5000 to 10000. In contrast, for the smallest insects, this number is around 10 [Ellington 1999].

The upper bound of this Reynolds number range coincides with the typical operational Reynolds number of micro air vehicles (MAVs), which are a type of emerging aerial vehicles with dimensions less than 15 cm in all directions and maximum flight speeds of approximately 10m/s, mainly used for surveillance and monitoring missions. This similarity in Reynolds numbers combined with the belief that insects benefit from dynamic stall lift, has motivated efforts to improve the maneuverability and thrust of these compact aerial vehicles by leveraging the DSV [Mueller 2000; Shyy et al. 2007].

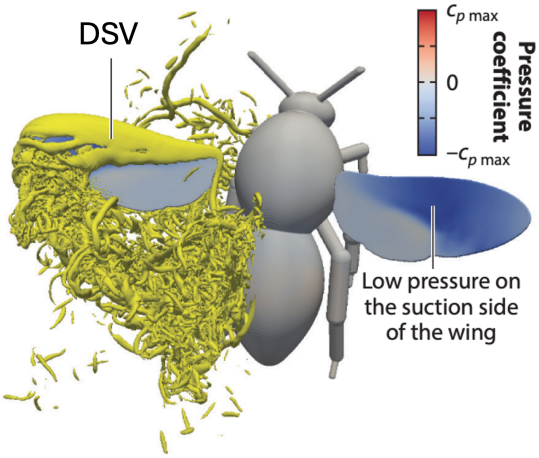

Figure 2.2: The leading-edge vortex over a flapping wing of a hovering bumble bee. Image extracted from [Liu et al. 2024].

Understanding dynamic stall remains a significant challenge in aerodynamics, despite extensive research efforts. The factors contributing to the formation of the dynamic stall vortex and the processes leading to its detachment are still debated and uncertain. A detailed understanding of this complex unsteady flow phenomenon is crucial for its prediction, control, and potential applications [Choudhry et al. (2014b) and Mulleners and Raffel (2012)].

2.1.1. Dynamic stall lift characteristics

The formation and growth of the dynamic stall vortex, a spanwise large-scale leading-edge vortex, is recognized as the mechanism that defines the onset and evolution of dynamic stall [Carr et al. 1977; Gendrich 1999; Mulleners and Raffel 2012; Choudhry et al. 2014b]. Thus, many investigators have made a significant effort to analyze this flow event to understand the fundamentals of the dynamic stall. In this context, Choudhry et al. (2014b) presented the unified theory, which is described in this chapter, to elucidate dynamic stall vortex shedding process and the subsequent lift generation. Additionally, compelling results and conclusions from other researchers are included in this section to supplement the aforementioned theory, thereby simplifying but also improving its comprehension.

For simplicity, an airfoil undergoing ramp-type pitching motion is used to assess and discuss the various phases of dynamic stall and their respective lift characteristics. This motion typically starts from a zero-degree angle and continues at constant pitching rates until reaching a predetermined maximum angle of attack. Unlike the sinusoidal scenario, where the airfoil returns to its minimum angle within each cycle, here the airfoil maintains the maximum angle of attack for an extended period, allowing deeper analysis of the stall phase. The pause after the upstroke phase also enables the DSV to be convected downstream without disturbance from the airfoil's motion. A more detailed explanation of the motions typically used for studying dynamic stall is provided in Section 2.1.2.

The flowfield around a NACA 0012 airfoil pitching from an angle of attack of 0° to 60° has been already shown in Figure 2.1. The lift curve associated with this airfoil, for both the steady and unsteady cases, is presented in Figure 2.3. Note that the unsteady case shows a higher lift coefficient during the onset of rotation phase. Choudhry et al. (2014b) attribute the increase in lift to the formation of the so-called starting vortex near the leading-edge. As this vortex convects downstream, it is diffused and the lift starts to decrease rapidly to steady-state levels. This flow mechanism and the subsequent lift response have not been observed in other experiments conducted with ramp-type pitching airfoils, which could indicate that if this starting vortex is present, its effect on the total lift may be almost negligible.

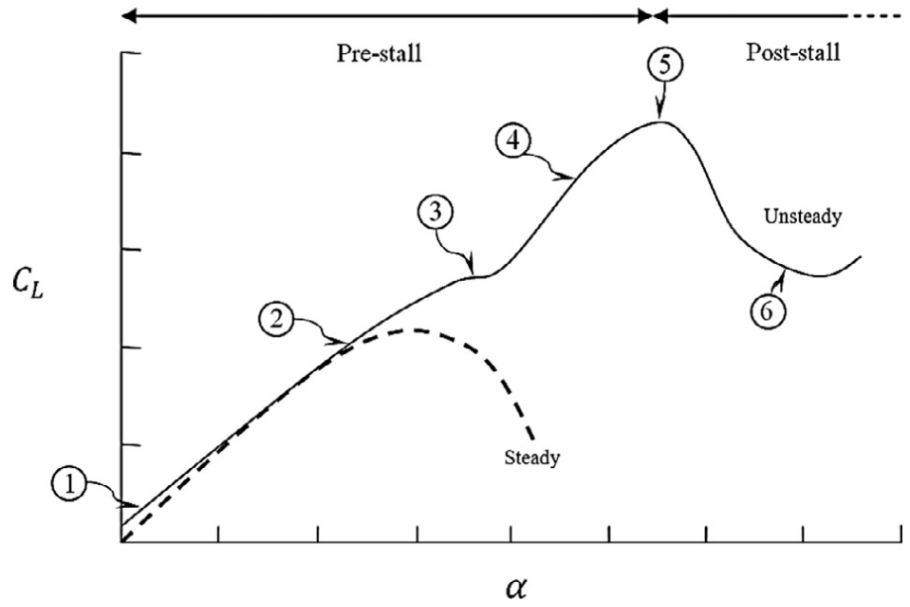

Figure 2.3: Comparison of the fundamental lift curves features between unsteady ramp-type dynamic stall and steady-state behavior. Plot extracted from [Choudhry et al. 2014b].

During the linear phase, the lift slope of both steady and unsteady lift curves are notably similar. Past the static stall angle of attack the unsteady lift keeps rising but with a reduced slope. According to Choudhry et al. (2014b), the reduction in the slope of the lift curve can be ascribed to an increase in the effective thickness of the airfoil. In Figures 2.1b and 2.4, the flow reversal inside the boundary layer can be observed. It can also be seen that the boundary layer is considerably thickened above the suction side near the leading-edge. However, the bulk flow still follows the contours of the airfoil, leading to an apparent thickness increase. It is well known that an increase in airfoil thickness results in a reduction in the lift slope, and therefore the thickening observed in Figure 2.4 could provide a valid explanation for the slope reduction observed between points 2 and 3 in Figure 2.3. Similarly, Carr et al. (1977) also attributed the slope reduction to the appearance of a reversal flow on the suction side of the airfoil, which was identified with smoke flow visualization. They pointed out that the recirculation region grows normal to the surface and extends upstream as the angle of attack increases beyond the stall angle of attack in static conditions. The reversal flow upstream evolution and normal growth can be identified when comparing Figures 2.1b and 2.1c. Highlight the fact, that within the recirculation region, the flow is separated and then reattached which does not necessarily mean that the bulk flow is separated. This is because although the recirculation region is present, the bulk flow still follows the contour of the airfoil.

The sustained generation of lift beyond static stall angles of attack can be explained by the formation of a counterclockwise vortex clearly visible in Figure 2.4 near the airfoil's trailing-edge as a result of the pitching motion. This vortex known as dynamic stall vortex, induces suction pressure on the separated shear layer at the trailing-edge, thus prolonging the attachment of the flow at higher angles of attack. Ericsson and Reding (1988) also argues that the lift overshoot could be caused by the so-called "leading-edge jet" effect. The authors suggested that the leading-edge of pitching airfoil is analogous to a leading-edge rotation cylinder which has proven to significantly increase the maximum lift coefficient and delay the onset of stall of several airfoils [Du et al. 2002; Salam et al. 2020]. This is because the pitching motion increases the tangential velocity of the leading-edge of the airfoil. In this way, the resistance to separation of the boundary layer is enhanced due to the momentum addition.

Prior to the formation of the DSV (point 3 in Figure 2.3), the flow reversal that at lower angles of attack started at the trailing-edge, spreads over the entire airfoil. The shear layer between the reverse flow region of the boundary layer and the free-stream flow is highly unstable and after a certain angle of attack, it evolves into a multitude of discrete clockwise vortices. As it can be seen in Figure 2.1d,

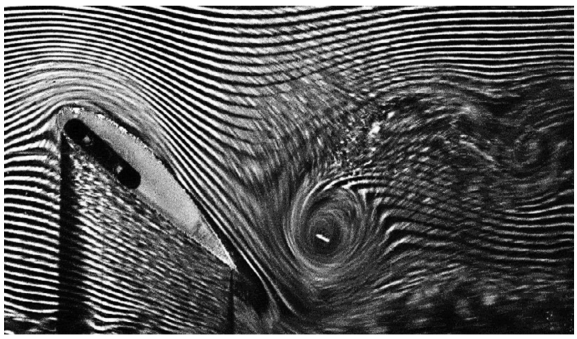

Figure 2.4: NACA 4418 airfoil pitched at a very high reduced frequency of k=2.04 is at the maximum angle of attack 40°. Image extracted from [Choudhry et al. 2014b].

the aft portion of these vorticity reorganizes into a shear-layer vortex (SLV), which is eventually convected downstream past the trailing-edge [McAlister and Carr 1979; Visbal and Garmann 2018; Hrynuk and Bohl 2020]. At the same time, the boundary layer near the leading-edge breaks down and separates from the airfoil's surface because it is not longer able to withstand the adverse pressure gradient. As this abrupt separation occurs, dynamic stall has begun [Carr et al. 1977]. Following the separation, the leading-edge shear layer undergoes a roll-up process, resulting in the formation of the dynamic stall vortex. As the pitching motion continues, the DSV grows in strength while it is still connected to its feeding sheet on the leading-edge. Through CFD and experimental flow visualization, it has been observed that between the DSV and the surface of the airfoil, a sheet vorticity with opposite sign to the DSV, which is also know as secondary vorticity, is generated due to the strong upstream flow motion induced by the DSV in this region [Mulleners and Raffel 2012; Visbal and Garmann 2018; Hrynuk and Bohl 2020]. The counterclockwise-rotating vortices initiate the onset of dynamic stall as they progress towards the leading-edge and encourage the detachment of the DSV from its feeding sheet [Mulleners and Raffel 2012].

The existence of the dynamic stall vortex leads to elevated suction pressures on the airfoil, resulting in a sudden augmentation of airfoil lift which can be attributed to the vortex low pressure core (see point 4 in Figure 2.3). When primary vortex is convected downstream and reaches the mid-chord position (see Figure 2.1f), the maximum lift is achieved as presented in point 5 in Figure 2.3 [Ham and Garelick 1968; Carr et al. 1977; Choudhry et al. 2014b]. The DSV can also be conceptualized as a rotating circular cylinder that provides additional circulation into the airfoil system by increasing the flow velocity on the suction side of the airfoil. In addition, it could be argued that the DSV increases the effective camber of the airfoil when it is located near the mid-chord position as indicated with the black discontinuous line in Figure 2.5. This is because the freestream follows the contour of the DSV inducing an increased apparent camber to the airfoil [Choudhry et al. 2014b].

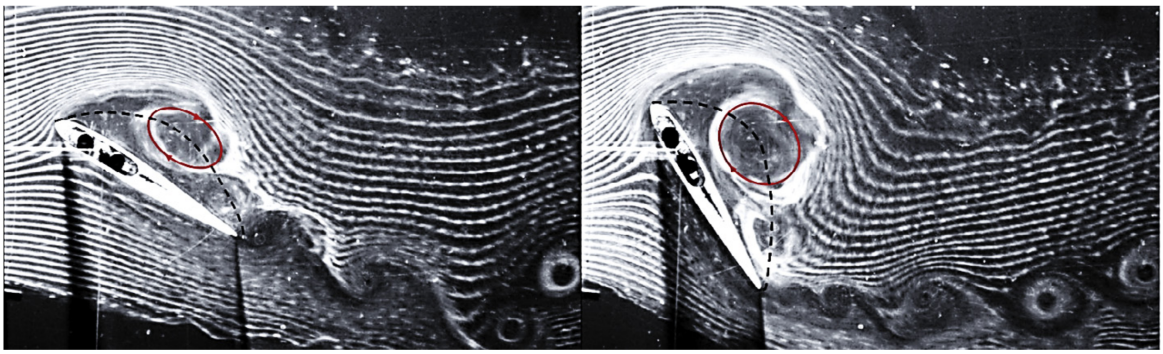

Figure 2.5: Apparent camber increase due to the presence of the dynamic stall vortex structure. Image extracted from [Choudhry et al. 2014b].

The airfoil enters the post-stall phase once the dynamic stall vortex has moved downstream and its low-pressure core no longer affects the airfoil. During this stall state, the flow on the suction side completely separates from the airfoil, resulting in a significant drop in the lift coefficient. This marks the onset of deep stall for the airfoil. To restore lift, the angle of attack must be substantially reduced until the flow reattaches to the suction side. It is important to note that this reattachment typically occurs at an angle of attack which is lower than the static stall angle of attack because it takes more time for the potential flow to return to its non-stalled state after the boundary layer reattaches.

The pitching moment and drag have usually received less attention in the dynamic stall research. This is because the lift coefficient overshoot is the most prominent feature of the dynamic stall phenomenon. Furthermore, the evolution of the pitching moment is strongly linked with the convection of the DSV. When the DSV is convected downstream beyond the pitch axis, the pitching moment begins to decrease drastically and the airfoil experiences a notable pitching down moment. This response is more significant as the DSV gets closer to the trailing-edge because its low-pressure core exerts more torque with respect to the center of rotation. The large increase in lift during the DSV convection phase is also accompanied by an equivalent increase in the drag due to the large angle of attack and the increased pressure over the suction side [Carr et al. 1977; McCroskey 1982; Jumper et al. 1987; Choudhry et al. 2014b].

2.1.2. Parameters of interest

Compared to its steady-state counterpart, dynamic stall is more difficult to analyze and model primarily because it relies on a significantly broader set of parameters [Choudhry et al. (2014b)]. Similarly to the static stall case, the main factors that affect stall behavior are the geometric parameters of the airfoil or wing, the Reynolds number, the Mach number, and the conditions of the incoming flow. However, the dynamic stall is also affected by several other parameters like the frequency and velocity of the changes in apparent angle of attack, and the location of the pitching axis, if it exists. Furthermore, pronounced unsteady aerodynamic loads can induce wing flexing and deformation, adding significant complexity to both experimental and numerical investigations of dynamic stall. Lastly, the offset of dynamic stall can be triggered by means of several movements: pitching at a constant rate, sinusoidal pitching, flapping, or plunging which is a periodic translation of the airfoil in a direction normal to the free stream. Hereinafter, the most significant parameters known to influence the dynamic stall phenomenon to varying extents are presented aiming to summarize and clarify their effects.

Reduced frequency

Reduced frequency is a parameter that is used to define the degree of unsteadiness of the flowfield. A basic formulation of this dimensionless number was first used by Kramer (1932) with the intention of characterizing the pitching oscillations of an airfoil with respect the incoming flow. It was suggested that its value should be preserved between flows with similar unsteadiness levels. The initial formulation evolved into the commonly used one shown in Equation 2.1, and it has been adopted by most of the subsequent research to this day. The reduced frequency is defined as the ratio of convective time scales (c/U) to the time scale of forced oscillation ($1/\dot{\alpha}$). For an airfoil of chord c, pitching at a constant pitch rate of $\dot{\alpha}$ [rad/s], the reduced frequency k can be calculated as Equation 2.1 where U_∞ is the freestream velocity. If, instead, the airfoil is pitching in a sinusoidal oscillation, then Equation 2.1 can be redefined using the constant angular velocity ω as $k = \omega c/2U_\infty$.

$$k = \frac{\dot{\alpha} c}{2U_\infty} \tag{2.1}$$

Throughout this work, this formulation will be adopted, as it is the most used in previous research [Carr et al. 1977; Gendrich 1999]. Nevertheless, it should be mentioned that other authors have used $k = \dot{\alpha} c/U_\infty$ [Visbal and Shang 1989]. This has been taken into account, thereby all the reduced frequencies presented hereinafter are calculated as Equation 2.1.

Initial research in the dynamic stall topic already identified the strong coupling between the reduced frequency and the flow unsteadiness associated with the dynamic stall phenomena. Researchers in the field have reached consistent conclusions, demonstrating a clear trend regarding the impact of reduced frequency on the dynamic stall process. As the reduced frequency increases, the airfoil is capable of generating greater lift forces beyond the static stall angle of attack regardless of the type of motion that induces the dynamic stall. Additionally, the onset of dynamic stall is delayed to higher angles of attack, resulting in an enhanced lifting potential for the airfoil or wing.

Ham and Garelick (1968) conduced a series of wind tunnel experiments with a NACA 0012 at a Reynolds number of 3.44×10^5. The airfoil was rapidly pitched from 0° to 30° at different constant pitching rates of k=0.005 and 0.02. It was observed that the strength of the lift overshoot was directly proportional to the pitching rate. Therefore it was suggested that the rate of change in angle of attack is the primary determinant of the vortex-induced peak lift experienced by an airfoil during dynamic stall. Carr et al. (1977) reached similar conclusions with a sinusoidally pitching NACA 0012 at reduced frequencies between k=0.02 and 0.05 and a Reynolds number of 2.5×10^6. Additionally, this study also suggested that the higher the reduced frequency, the later the stall occurs. Furthermore, it was pointed out that for the very low reduced frequencies tested, the DSV is shed and convected downstream even before the maximum amplitude of the oscillation is reached. These observations have been supported by subsequent research in the field [Jumper et al. 1987; Choudhry et al. 2014b], and it is widely accepted now that the onset of dynamic stall is delayed to higher angles of attack when the reduced frequency is increased, resulting in an enhanced lifting potential (see Figure 2.6).

Similarly, the effects of the reduced frequency on dynamic stall have been studied using CFD. Visbal and Shang (1989) successfully simulated a NACA 0015 airfoil pitching about a fixed axis from zero incidence to a maximum angle of attack of 60 degrees. The freestream chord Reynolds number was 1×10^4. The non-dimensional pitch rate was varied over the range k=0.05 to 0.3. The dynamic stall vortex was clearly observed, and it was concluded that increased pitching rates cause the dynamic stall vortex to form at a higher angle of attack.

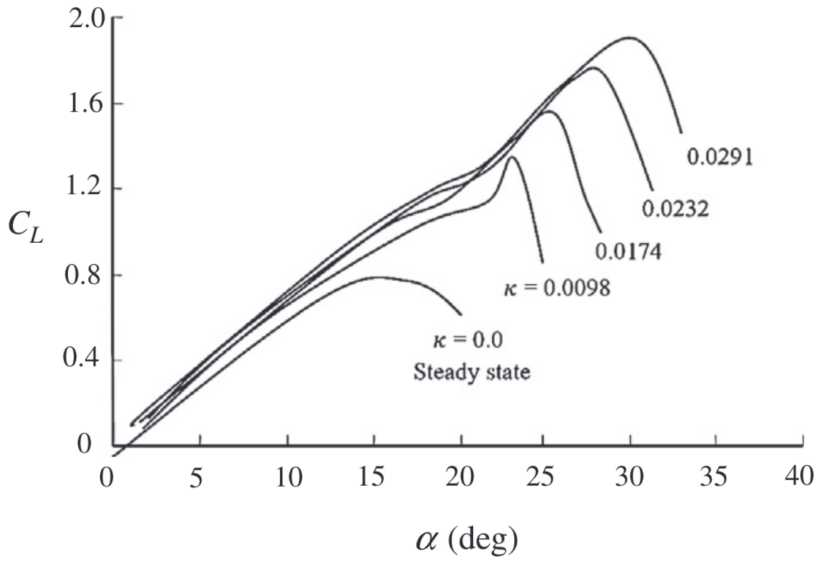

Figure 2.6: Effect of increasing reduced frequency on the lift curve of a NACA 0015 at Re=1.6×10^5. The plot is extracted from Choudhry et al. (2014b).

Reynolds number

Research on the dynamic stall of airfoils has extensively examined the effects of Reynolds number. For example, through experimental tests, Carr et al. (1977) studied a sinusoidally pitching NACA 0012 airfoil for a set of Reynolds numbers varying from 1×10^6 to 3.5×10^6. It was concluded that Reynolds number had a less dramatic effect compared to wing kinematics such as reduced frequency, oscillation amplitude, and mean angle of oscillation. Kiefer et al. (2022) measured the transient

pressure field around an airfoil undergoing ramp-type pitching motions at Reynolds numbers ranging from $0.5\times10^6<Re<5.5\times10^6$. Results indicated that the basic characteristics of stall development did not change significantly when increasing the Reynolds number, although there was a delay in stall progression and an increase in maximum lift coefficient. Choudhry et al. (2014b) found that both the maximum lift and the angle of attack at which dynamic stall occurs increased as the Reynolds number rose from 0.5×10^5 to 1.5×10^5. Several other research groups have thoroughly investigated the primary impact of the Reynolds number on the dynamic stall development, generally concluding that it has a minimal effect on the overall stall process, and although the maximum lift coefficient and the stall development are delayed in time, the overall evolution of the dynamic stall phenomenon remains unaltered [Walker et al. (1985), Jumper et al. (1987), Lorber and Carta (1987), and Conger and Ramaprian (1994)].

Further exploration into the unsteady flowfield revealed that the turbulent structures associated with the DSV diminish in size with increasing Reynolds numbers. Choudhuri and Knight (1996) demonstrated that increasing the Reynolds number from 10^4 to 10^5 slightly reduces these flow structures. It was also suggested that the DSV forms closer to the leading-edge and with increased strength as the Reynolds number increases. Zhang and Schlüter (2012) corroborated this by showing through CFD simulations that while the overall dynamic stall process remained consistent across Reynolds numbers from 440 to 2.1×10^4, the scale flow structures was inversely proportional to the Reynolds number as it can bee seen in Figure 2.7

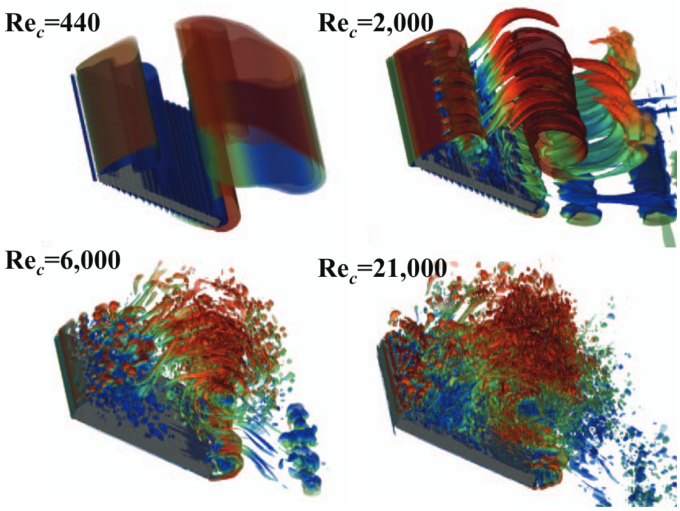

Figure 2.7: Flow visualization of the DSV using isosurfaces of the q-criterion. The image is extracted from Zhang and Schlüter (2012).

Airfoil geometry

Since the 1960s, investigations into dynamic stall focused on the retreating-blade stall observed in most modern helicopters. This phenomenon was recognized as a limitation on the high-speed performance of these aircraft. McCroskey et al. (1981) evaluated the dynamic stall process of six airfoil sections considered to be representative of contemporary helicopter rotor designs. These airfoils underwent experimental testing involving sinusoidal pitching oscillations under a wide range of unsteady flow conditions. As a result, the NACA 0012, which was among the selected airfoil sections, became a standard reference and has been widely adopted by subsequent researchers for their investigations, serving as a benchmark for comparing computational and experimental results. Additionally, some investigators preferred the NACA 0015 for their experiments due to its increased thickness, which facilitated the installation of pressure taps and transducers within the airfoil section. The widespread use of the NACA 0012 and 0015 airfoils in dynamic stall research has resulted in a lack of experimental and numerical results for other geometries. Consequently, the effect of the airfoil profile on the dynamic stall process has largely been ignored.

McCroskey et al. (1981) introduced two dynamic stall regimes, namely, light and deep dynamic stall, based on the difference between the maximum angle of attack achieved during the unsteady cycle and the stall angle of attack of the airfoil in static conditions. It was suggested that light dynamic stall occurs if the maximum dynamic angle of attack does not surpass the angle of attack at which the baseline airfoil stall in static scenarios. This categorization was also adopted by Mulleners and Raffel (2012), who further defined that the light stall occurs when the downstroke motion begins before the DSV has developed. The boundary between these light and deep dynamic stall regimes is somewhat broad and arbitrary. Nevertheless, specific aerodynamic characteristics can be associated with each regime. In the light dynamic stall regime, the aerodynamic loads typically exhibit significant hysteresis. However, the maximum values of lift and pitching moment coefficients usually remain similar to their static counterparts. In contrast, when the DSV is well defined, and unsteady fluctuations are substantial, the airfoil is considered to be in the deep dynamic stall regime. Under this condition, the aerodynamic loads are significantly higher than in the static case [McCroskey et al. 1981; Gendrich 1999; Mulleners and Raffel 2012].

The experimental study conducted by McCroskey et al. (1981) with six different airfoils concluded that the unsteady aerodynamic behavior resulting from the dynamic stall phenomenon tends to be sensitive to the geometry of the airfoil in the light stall regime. This is because both the leading and trailing-edge separation can be observed depending on the airfoil shape. For the first one, the separation starts at the trailing-edge and propagates upstream until it spreads over the whole chord of the airfoil. Contrarily, the leading-edge separation is typically associated with the busting of the LSB formed close the leading-edge after which the boundary layer is not able to stay attached to the airfoil's suction side. The fact that the stall can occur in different ways results in distinct unsteady aerodynamic loads response depending on the airfoil shape. On the other hand, McCroskey et al. (1981) pointed out that during deep dynamic stall, the differences between airfoils diminishes and the effect of the airfoil shape becomes irrelevant. Subsequent research has proved that to some extent this statement is true. Choudhry et al. (2014b) presents the dynamic stall process of three airfoils with significantly different shapes pitching at constant rate up to α=50°. The flow structures are very similar regardless of the airfoil section, with the DSV being clearly visible for all the cases. However, the angles at which the DSV is formed and its convection speed are considerably different. The authors conclude that an organized study towards understanding the effects of airfoil leading-edge radius, camber and thickness-to-chord ratio on the dynamic stall process is still lacking.

The thickness-to-chord ratio effect on the dynamic stall process has been studied by Leknys et al. (2016). PIV was employed to investigate the impact of the thickness of the airfoil. Within a water tunnel, two four-digit NACA airfoils (0021 and 0012) were examined. These airfoils underwent a ramp-up motion at a constant pitching rate, with the experiments maintaining a consistent Reynolds number of 2×10^4. The findings of this study indicated that when k<0.05, the thicker airfoil developed a more extensive laminar separation bubble and a weaker dynamic stall vortex. The thinner airfoil demonstrated greater susceptibility to abrupt separation, resulting in the formation of a stronger DSV. The development of flow structures remained relatively consistent for higher reduced frequencies. In line with these findings, Bangga et al. (2021) also observed through CFD that as the airfoil thickness increases, the strength and size of the leading-edge vortex decreases.

Airfoil kinematics

As mentioned earlier in Section 2.1, a key focus of dynamic stall research has been to minimize or mitigate, to some extent, the unsteady effects associated with this phenomenon. To do so, the evolution of the dynamic stall has to be fully understood, since both the DSV formation and convection phases, but also the posterior flow reattachment, which occurs during the pitching down phase, determine the unsteady response of the aerodynamic loads. To characterize all phases of this process, researchers have typically changed the angle of attack of airfoils and wings by dynamically pitching them under a sinusoidally motion instead of changing the direction of the incoming flow [Carr et al. 1977; McCroskey et al. 1981; Rival and Tropea 2010; Mulleners and Raffel 2013; Borg 2012]. The oscillating motion can be defined by a mean angle α_0, the amplitude of the oscillation α_1, and its frequency f_{osc}. These three parameters determine the unsteadiness of the simulated flow, but also the dynamic stall regime that occurs.

Constant pitch-rate motions have also received a great deal of attention, particularly for those studies aiming to profit from the lift enhancement resulting from the DSV with the ultimate goal of improving aircraft maneuverability or wind turbine performance. For this type of dynamic stall study, the airfoil typically starts from a rest position at an angle of attack of 0°. The motion usually begins with an initial acceleration phase until the desired pitch rate is achieved. Afterward, the airfoil maintains this pitch rate until it reaches a high angle of attack above the static stall angle of attack, typically from 30°to 60°. Ideally, the acceleration phase should be kept as brief as possible. However, it has been demonstrated that as long as the acceleration phase concludes before the onset of leading-edge separation, the acceleration phase has minimal to no impact on the dynamic stall process [Koochesfahani and Smiljanovski 1993]. This approach is inherently simpler than the sinusoidally pitching motion and therefore it has been widely used [Jumper et al. 1987; Gendrich 1999; Choudhry et al. 2014b; Kiefer et al. 2022]. The downside of this motion is that the reattachment phase during the downstroke phase cannot be studied.

The unsteady flow development over an airfoil pitching up at a constant rate is known to be remarkably similar to that of an oscillating airfoil [Gendrich 1999; Choudhry et al. 2014b]. The distinguished flow features within a full dynamic stall cycle are, in sequence: the emergence and spreading of flow reversal on the airfoil's suction side, the formation and convection of a large-scale DSV, significant flow separation after the DSV is convected beyond the trailing-edge, and reattachment which only occurs during the pitch-down phase. Because of the similarity between both types of motion, Mulleners and Raffel (2012) proposed a single parameter to describe the overall influence of the airfoil's unsteadiness on the onset of stall. For an oscillating airfoil, the onset of stall is a problem dependent on three parameters α_0, α_1 and f_{osc}. On the contrary, the ramp-type pitching motion can be described by the pitch rate $\dot{\alpha}$ and the final angle of attack that is analogous to α_1. In their work, Mulleners and Raffel (2012) suggested that the reduced frequency k should be calculated as $k = \omega c/U_\infty$ but instead of using the angular velocity of the pitching axis $\dot{\alpha}$, the instantaneous effective unsteadiness $\dot{\alpha}_{ss}$ should be used. This variable is defined as the rate of change of α at $t = t_{ss}$, which is the moment at which the static stall angle of attack is reached. This effective unsteadiness is simply the pitching rate in the constant pitching case.

2.2. Leading-edge tubercles

Flow control devices are widely utilized in various applications such as on airplane wings and turbine blades. These devices are categorized into two types: passive and active. Passive devices are constantly active and operate independently of the flow conditions, while active devices employ actuators that allow them to be activated or deactivated based on the operating conditions. The primary objective of both types of devices is to manipulate the flowfield, either through actuation or interaction, to elicit a desired change in flow behavior. This modification aims to enhance performance, with potential applications including jet noise reduction, improved aircraft maneuverability, and airfoil stall reduction.

The tubercles are a type of passive flow control device inspired by the unique protuberances along the leading-edge of the humpback whale (*Megaptera novaeangliae*) flippers as shown in Figure 2.8. An adult specimen can reach up to 19 m in length and exceed 53 tons in weight, yet this whale is extremely agile and capable of incredibly tight underwater maneuvers needed as part of its feeding routine [Fish 2020]. This outstanding maneuverability of the humpback whales was first attributed by Fish and Battle (1995) to their pectoral flippers and their leading-edge particular morphology not seen in any other whales.

Later research on this topic proved that the tubercles placed on the leading-edge of the flipper improve its overall aerodynamic performance. This improvement is most noticeable at high angles of attack, particularly near stall. By conducting a wind tunnel test using idealized models of a humpback whale flipper with and without tubercles, Miklosovic et al. (2004) found that the tubercles delay the stall angle approximately by 40% while increasing the lift and decreasing the drag after the stall. Similar effects of the leading-edge tubercles on the aerodynamic performance of a flipper have also been found by other researchers through experimental techniques [Weber et al. 2010] and computational fluid dynamics [Weber et al. 2011].

Figure 2.8: Humpback whale´s flipper featuring leading-edge tubercles. Extracted from [1]

Further research on full-span airfoil also found that tubercles have different effects on the aerodynamic performance of finite- and full-span wings. As pointed out by Miklosovic et al. (2007), tubercles lead to a delay in the onset of the stall and an increase in maximum lift on a 3D flipper, while a softened stall with lower maximum lift is observed on the (2D) full-span wing. Subsequent CFD research, shed some light on the 3D effects causing this disparity in performance. Carreira Pedro and Kobayashi (2008) found that the vorticity shed from the tubercles confines the tip separation to the outboard flipper region and therefore increases the performance of the wing.

2.2.1. Tubercles morphology

Over the past two decades, there has been an increased interest in the leading-edge tubercles on airfoils and wings. Since it was first claimed by Fish and Battle (1995) that pectoral flippers with leading-edge perturbations were responsible for the remarkable agility of the humpback whale, research has focused on understanding how tubercles work and how they potentially alter the flowfield around and airfoil or a wing.

The research conducted up to date has to be split into two main groups: full-span and finite wings, on which the addition of tubercles has been observed to have different effects. Hence, from now on, the term “full-span wing”, or just “airfoil” will represent a two dimensional wing with infinite span, while “wing” or “flipper” will refer to a finite span 3D wing. Figure 2.9 shows the two typical configurations used in the research. On the left, a full-span constant chord wing is enclosed by two sidewalls aiming to reduce the 3D aerodynamic effects to study the airfoil performance (i.e., essentially the 2-D effects). On the right side, a wing mounted in a closed test section. Highlight that wings resembling the pectoral flipper of a humpback whale have been mainly used to study the effect of the protuberances on finite wings.

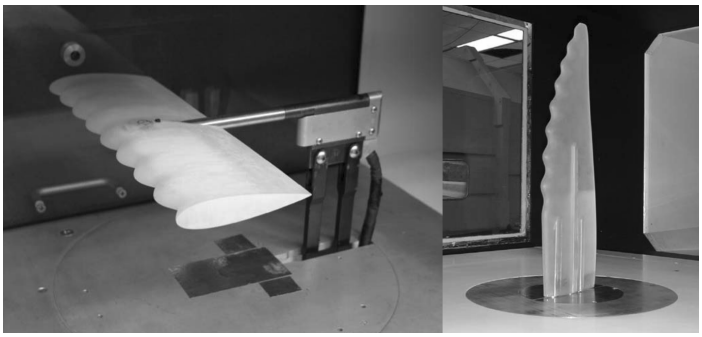

Figure 2.9: Typical full-span (left) and finite (right) wing models used by Miklosovic et al. [2004;2007].

[1] `https://www.australiangeographic.com.au/fact-file/fact-file-humpback-whale-megaptera-novaeangliae/` (Last accessed on 13 September 2023)

A prevalent trend in the selection of airfoil sections in existing literature is notable. In pioneering studies of humpback whale pectoral flippers, it was established that the NACA 63_4-021, closely resembles the flipper's cross-sectional profile [Fish and Battle 1995]. Subsequently, Johari et al. (2007) employed this airfoil in one of the initial experimental tests of a full-span wing equipped with tubercles in a water tunnel. This choice gained popularity, and numerous researchers adopted the NACA 63_4-021 airfoil to explore the influence of leading-edge protuberances. Conversely, Miklosovic et al. (2004) took a different approach by opting for the conventional NACA 0020 airfoil asserting that this section corresponds closely with the flipper cross-sectional profile of the humpback whale. The findings of these two researchers laid the groundwork for subsequent investigations, and thus, the NACA 63_4-021 and NACA 0020 airfoils persist as preferred options for studying the tubercles. A visual comparison of the humpback whale pectoral flipper cross section with the aforementioned airfoils is presented in Figure 2.10. It is worth noting that both airfoils are approximately 20% in thickness and commonly exhibit trailing-edge separation. These characteristics make them also suitable choices for addressing the dynamic stall problem investigated in this study [Choudhry et al. 2014a].

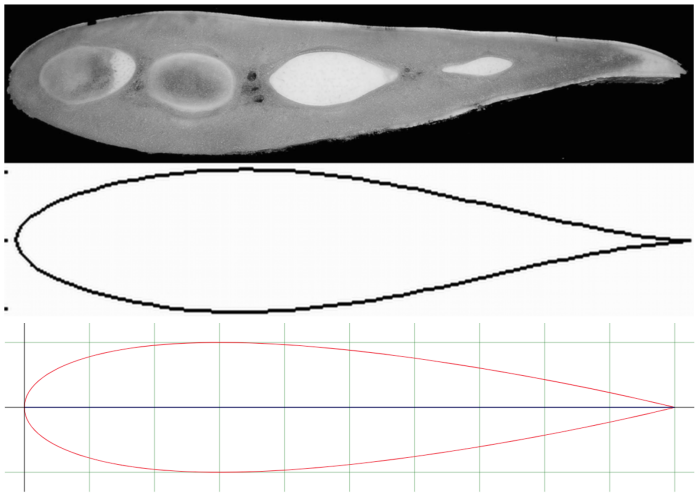

Figure 2.10: Comparison of a humpback whale pectoral flipper cross section with the NACA 63_4-021 and 0020 profiles. Shown top to bottom in this order [2007]. NACA 0020 extracted from [2]

Regardless of whether the leading-edge protuberances are used on a full of finite-span wings, the perturbations are commonly defined by a sinusoidal curve. The two main parameters widely used to characterize the sinusoidal shape are the amplitude A defined as half the chordwise distance between peak and valley, and the wavelength λ which is the spanwise distance between two consecutive peaks. In the present work the nomenclature proposed by Hansen et al. 2009 to designate the geometries of the tubercles is slightly modified. The amplitude A and wavelength λ are summarized in a single code. For example $A5\lambda8$ represents a tubercle array with amplitude of $A/\overline{c} = 0.05$ and wavelength of $\lambda/\overline{c} = 0.08$.

Although the amplitude and wavelength determine the shape of the tubercles, the shape of the final airfoil or wing is not fully defined with these two parameters and can vary depending on how the tubercles are added to the wing. Tubercles can be defined as added material onto the leading-edge requiring the thickness-to-chord ratio to change periodically in the spanwise direction. In this way, the rearward part of a peak and trough sections remain constant. This methodology has been used by Borg (2012) and Johari et al. (2007), among others. Instead, the tubercles can also be modeled employing a series of two-dimensional sections with varying chord and therefore preserving the original airfoil shape and its thickness-to-chord ratio. This design method results in a wing with valleys and ridges extending downstream in the chord direction. Although being less common method, it has been used by Hansen et al. [2009;2012]. The tubercle sections obtained with these two methods are presented in Figure 2.11. Whether, the tubercles are designed changing or maintaining the thickness-to-ratio spanwise, their impact of on the performance of any airfoil or wing is fairly similar [Bolzon et al. 2016].

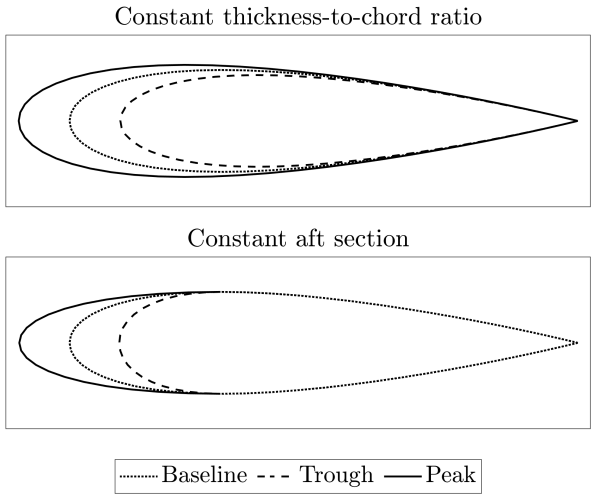

Figure 2.11: Constant thickness-to-chord ratio (top) and constant aft section (bottom) airfoil sections.

2.2.2. Flow physics

Ever since Miklosovic et al. (2004) confirmed through wind tunnels tests that a finite wing with tubercles could outperform a smooth leading-edge finite wing both in pre-stall and post-stall regimes, numerous researchers have focused their efforts on understanding how the leading-edge tubercles modify the flowfield around a wing and subsequently enhance its aerodynamics performance.

To date, it is clear that the tubercles shed a pair of streamwise counter-rotating vortices which can be seen in Figure 2.12. This phenomenon has been observed in the wind tunnel with PIV and dye flow visualization [Custodio 2007; Hansen 2012; Zhang et al. 2014]. Numerical simulations using CFD have given a more detailed visualization of these vortical structures [Rostamzadeh et al. 2014; Cai et al. 2017]. Although there is a broad consensus among researchers that these counter-rotating vortices change the stall performance of any airfoil or wing, it is still unclear how the surrounding flowfield is altered and what flow physics mechanisms are triggered with the presence of the streamwise vortices. Many attempts to shed some light on the tubercles flow physics have been done and numerous flow mechanisms have been proposed. Yet, none of them has been conclusive. Hereinafter, the more compelling and accepted tubercle mechanisms are presented and discussed.

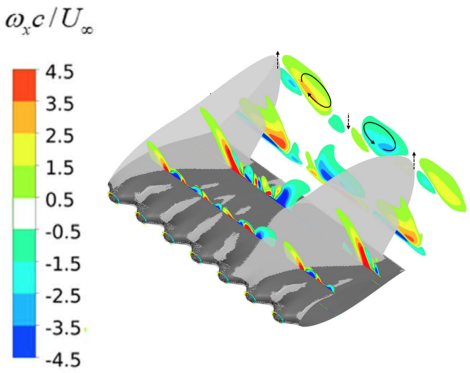

Figure 2.12: Streamwise vorticity and stall cells on a tubercled airfoil at α=16°[Cai et al. 2017].

Vortex generators

Miklosovic et al. (2004) argued that the leading-edge tubercles act as vortex generators, energizing the flow over the wing, subsequently inhibiting chordwise flow separation and ultimately resulting in delayed stall. Van Nierop et al. (2008) challenged this hypothesis stating that it is implausible that the leading-edge protuberances act as vortex generators since both the wavelength and amplitude of the peaks are typically much larger than the boundary layer thickness, while the height of a vortex generator is generally of the same order of magnitude as the boundary layer thickness.

[2] `http://airfoiltools.com/airfoil/naca4digit` (Last accessed on 13 September 2020)

As a counter-argument, Hansen (2012) proposed the so-called effective tubercle height h_{eff} which represents the height of the tubercle as seen by the flow and it can be calculated as $h_{eff} = Asin\alpha$ where α is the angle of attack of the airfoil. In this way, the obtained ratio of tubercle effective height to boundary layer thickness was typically less than one, which is in line with the more common vortex generators [Lin 2002]. Zhang et al. (2014) adopted this effective height ratio and proved that over an angle of attack range of 0° to 60°, the value of this ratio is typically between 0.1 and 0.6, and therefore claiming that this result imply that the leading-edge tubercles indeed work as vortex generators.

Vortex lift

The streamwise vortices shed by the tubercles are convected downstream over the suction side of the airfoil, generate alternating regions of increased downwash and upwash that extend in the chordwise direction. The upwash regions coincide with the troughs, whereas the downwash regions are aligned with the spanwise position of the peaks [Carreira Pedro and Kobayashi 2008; Custodio 2007; Hansen 2012].

Based on this flow phenomenon, Custodio (2007) suggested that the tubercles could be analogous to small delta wings producing vortex lift in the same way. The pair of counter-rotating vortices produce a net upwash in the valley regions increasing the effective angle of attack leading to earlier separation. On the other hand, the downwash over the spanwise position of each peak has the opposite effect and reduces the effective angle of attack, leading to reduced separation. It was also proposed that at pre-stall conditions, the amount of vortex lift generated by the streamwise vorticity is not enough to overcome the reduction in lift experienced at the troughs caused by the earlier onset of separation. After stall, it was postulated that the higher angle of attack would lead to a stronger streamwise vorticity increasing the amount of vortex lift generated. Considering that at post-stall regime the baseline airfoil is completely separated, the increased downwash aligned with the peaks could increase lift by improving attachment at the expense of worsened separation at the troughs.

Bolzon et al. (2016) challenged this hypothesis mentioning two main differences between tubercles and delta wings. First, a delta wing only creates two vortices which are shed along the leading-edges of the wing. Thus, there is a vortex located over the two swept back leading-edges. This pair of vortices increase the downwash on the whole wing suction side while the upwash areas are located away from the wing surface. As a result, the wing is only affected by the downwash, resulting in delayed stall. Note that each tubercle produces a pair of counter-rotating vortices. Therefore, it can be expected that vortex lift will be generated in the peaks where downwash is enhanced. On the other hand, the upwash will cause the flow to separate earlier in the troughs, equalizing the lift gained in the peaks. The second important difference is the fact that the shedding edge distance of a delta wing is considerably larger than the average size of the studied tubercles. This geometrical difference could potentially mean that the strength of the vortices created by the tubercles and a delta wing cannot be equal.

Compartmentalization

Carreira Pedro and Kobayashi (2008) studied the static performance of a humpback whale pectoral flipper through CFD and concluded that the tubercles confine the leading-edge separation to the tip region, justifying the enhanced performance of the flipper with tubercles when compared to the flipper with smooth leading-edge. It was claimed that the streamwise vorticity acts as virtual barrier to the span-wise flow motion which prevents the tip separation from growing towards the root. This is very similar to the working principle of wing fences, which imposes a physical rather than flow barrier on the spanwise flow.

The compartmentalization mechanism can also be extended to airfoils. Cai et al. (2018) first identified the effect of compartmentalization through experimental investigation of a rectangular wing with a single leading-edge protuberance. The lift force measurements presented a double-step stall process for increasing angles of attack as presented in Figure 2.13. For the first stall step, the lift coefficient dropped to an intermediate value in between the maximum and the post-stall baseline lift coefficients, remaining constant within the range of angles of attack 16°to 20°. Tuft flow visualization revealed that one side of the tubercle, the airfoil was stalled while the flow on other side remained attached. In contrast, the flow on the baseline airfoil at such angles of attack was already fully separated. When the angle of attack further increased, the second step of stall could be identified, with the

lift dropping to baseline post-stall levels, and the flow being fully separated across the span. It was thereby proposed that when one side of the airfoil was stalling, attached flow originating from the peak, confined the local leading-edge separation and prevented it from extending to the other side of the airfoil.

Cai et al. (2017) extended the research to an airfoil with multiple leading-edge tubercles. By means of CFD, it was detected that non-consecutive valleys were stalled while the region in between was still attached and therefore generating lift. In general, the distance between the stalled valleys was found to vary between 2λ and 6λ depending on the geometry of the tubercles. As presented in Figure 2.12, the separated regions emanating from the valleys extend downstream and increase in width, creating a so-called dilatation-type compartmentalization. The non-separated span between the two dilatation regions is contracted in the chordwise direction. Cai et al. (2017) suggested that the near-wall momentums are replenished within the contraction-type compartmentalization avoiding the occurrence of stall in the area. It was also highlighted that once the stall region occurs, the downwash on the adjacent attached region is significantly enhanced due to the vorticity delimiting the separation region. Thus, it could be speculated that the local effective angle of attack within the contraction-type compartmentalization is significantly reduced. This phenomenon is also visible in Figure 2.14, where stall cells can be clearly seen, as indicated by the region with more diffused dye.

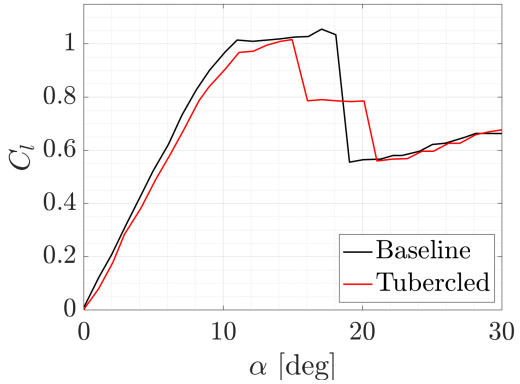

Figure 2.13: Comparison of lift coefficient between the baseline (black) and tubercled (red) airfoils. Data extracted from [Cai et al. 2018].

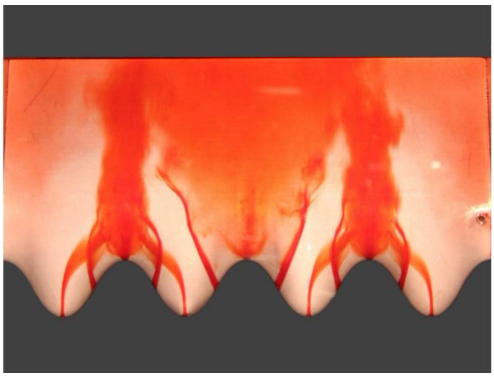

Figure 2.14: Compartmentalization visualization using dye flow technique on a tubercled airfoil at α=18°[Custodio 2007].

Pressure recovery mitigation

As explained in Section 2.2.1, the tubercles can be understood as material added to the leading-edge of an airfoil or in other words, as mere extensions of the airfoil chord. Thus, the tubercles periodically increase and reduce the chord along the spanwise direction. In this context, Van Nierop et al. (2008) proposed a theory alternative to the vortex generator working principle, and argued that the tubercles alter the pressure distribution on the airfoil surface so that separation is delayed behind the peaks. This phenomenon ultimately results in a gradual and smoother onset of stall at large angles of attack. Using an aerodynamic model based on determining the spanwise distribution of circulation, it was asserted that peaks and troughs have to withstand similar adverse pressure gradients. Since neighboring peaks and troughs have similar thicknesses but different chords, the same pressure difference must be recovered with a shorter distance at the span positions aligned with the troughs. Therefore, the separation occurs first behind the troughs, while it is delayed on the peaks. Hansen (2012), through hydrogen bubble flow visualization, showed again that the flow is separating earlier behind the troughs than the peaks affirming that the larger adverse pressure gradient along the troughs could cause it. Rostamzadeh et al. (2014) provided C_p curves along the peak and trough sections providing more direct evidence supporting this theory.

This flow mechanism was introduced during the initial research conducted on tubercles and stands out as one of the simplest explanations provided in this section. Therefore, although it may partially account for the delay in the onset of stall, it does not address flow features such as the aperiodic separation patterns observed in CFD and the tip separation being confined by the streamwise vorticity.

Coexistence of flow mechanisms

The mechanisms discussed in this section are not mutually exclusive, and it is unlikely that there is only one mechanism occurring. Instead, it is more likely that the flow physics of the tubercles can be explained by a combination of the mechanisms mentioned above [Bolzon et al. 2016].

The explanations often overlap, suggesting that multiple benefits can occur simultaneously. For instance, the compartmentalization mechanism, as explained by Cai et al. (2017), illustrates this point well. Although it is suggested that streamwise vorticity limits the spanwise extension of separation, it is also noted that the flow remains attached between two separated regions. This attachment is due to the streamwise vorticity re-energizing the boundary layer, in a manner similar to the action of vortex generators. Furthermore, it is mentioned that the induced downwash on the attached regions delays separation by reducing the effective angle of attack. This scenario clearly demonstrates how various proposed mechanisms can coexist and function simultaneously.

This being said, it is widely accepted that the streamwise counter-rotating vortices mix the near-wall flow, increasing the momentum transfer within the boundary layer re-energizing it as a result. This mechanism is in line with the working principle of the vortex generators. The compartmentalization mechanism has also been observed in both CFD and wind tunnel experiments which could potentially suggest that it is also present. Other mechanisms, like vortex lift and reduced adverse pressure gradient on the peaks are less accepted. Nevertheless, as mentioned previously, it is most likely that the working principle of the tubercles is a combination of mechanisms, and therefore none of them can be discarded.

2.2.3. Effect of tubercles on airfoils in static conditions

Miklosovic et al. (2004) studied the lift and drag of a humpback whale pectoral flipper using an idealized model in the wind tunnel. Their research concluded that compared to the model with a smooth leading-edge, tubercles lead to a 6% increase in the maximum lift coefficient and 40% increase in the stall angle as shown in Figure 2.15. Hence, the tubercled flipper showed an expanded operating span of angle of attack reaching higher lift values at higher angles of attack. At low angles of attack i.e. $\alpha<12°$, the drag was similar to that of the smooth flipper. However, at higher angles of attack, the smooth flipper suffered from abrupt loss of lift due to stall and a subsequent increase in pressure drag, whereas the lift of the tubercled flipper still increased without abrupt drag increase. In baseline post-stall regime, the drag of the tubercled wing was also consistently lower. These findings were highly intriguing and cast light upon an exciting area of study in aerodynamic flow control.

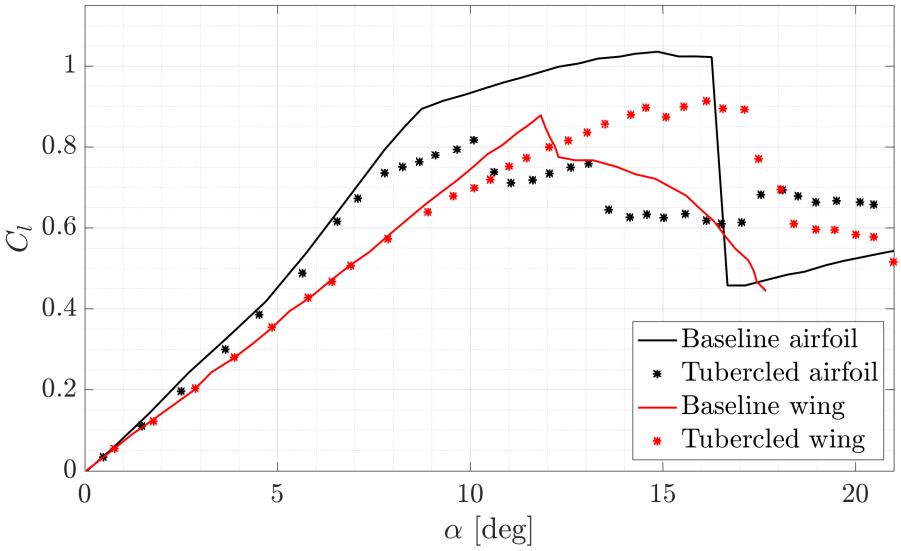

Figure 2.15: Lift slope of airfoils and wings with and without tubercles [Miklosovic et al. 2007].

To delve deeper into the underlying flow mechanisms and working principles of the tubercles that presented such attractive aerodynamic performance enhancements, further research was required. Johari et al. (2007) subsequently evaluated the performance of the tubercles on the rectangular full-span wing. The airfoils with leading-edge protuberances also stalled in a different manner compared to the airfoil with smooth leading-edge. However, the stall process was different to what it was first observed by Miklosovic et al. (2004). The tubercles caused a lift reduction at angles of attack below the baseline stall angle. In post-stall regime, the tubercled airfoil showed higher lift coefficients by almost 50%, leading to a softer and delayed stall. The lift coefficient remained constant for the range of $10°<\alpha<26°$. Although higher aerodynamic efficiency was measured in the post-stall regime, the airfoil with tubercles exhibited a higher drag coefficient overall. This phenomenon was particularly visible for the range of $15°<\alpha<21°$.

At the same time, Miklosovic et al. (2007) extended his initial research and experimentally studied the effects of the tubercles on a rectangular full-span wing. The objective of the research was to determine whether the performance improvements seen with the 3D flipper resulted from enhancements to the sectional characteristics of the airfoil i.e. 2D effects, or if instead the Reynolds number or the 3D effects were the main drivers. Similarly to the findings of Johari et al. (2007), the tubercles provided additional lift beyond the static stall angle of attack of the smooth leading-edge airfoil (see Figure 2.15). However, it was found out that the drag was reduced in the post-stall region. Despite the minor difference in the drag response after stall, both studies lead to similar results for a airfoil with tubercles, namely, softer stall with increased lift in post-stall conditions, and increased drag in the pre-stall regime. Besides, both wind tunnel experiments agreed on the fact that the $C_{l_{max}}$ is reduced for an airfoil with tubercles.

Further extensive work has been conducted to gain a deeper understanding of the difference in the effect of tubercles on full- and finite-span wings. Through computational fluid dynamics, Carreira Pedro and Kobayashi (2008) first pointed out that the outboard section of the flipper is dominated by leading-edge separation. As the angle of attack increases, this separation propagates inboard. The vorticity shed from the protuberances confines the separation and prevents it from propagating in the spanwise direction. The performance of an idealized humpback flipper was also studied by Van Nierop et al. (2008) by means of a numerical model. A lager maximum lift coefficient was not reproduced by the model. Yet, the progressive onset of stall and the reduced maximum lift coefficient were predicted. Thus, it was suggested that the performance enhancement seen in previous research could be related to tip effects that were not accurately described by the model implementation. Kim et al. (2018) experimentally investigated the effect of the tubercles on the idealized flipper model. Unlike in the previous research, PIV and oil flow visualization were used to cast light on the lift enhancement seen in previous research. Although this experiments were conducted at a Reynolds number considerably lower than Miklosovic et al. (2004) experiments (1.8×10^5 compared to 5.2×10^5), the maximum lift coefficient increase, the onset of stall delay, and the drag reduction in the baseline post-stall regime, were also observed. Through surface oil visualization, it was also possible to observe that indeed the streamwise vorticity confined the tip separation as shown in Figure 2.16. At α=9°the baseline flipper without tubercles was already presenting a noticeable flow reversal region at the tip, while the tubercled flipper outboard-span was considerably attached with minimal tip separation.

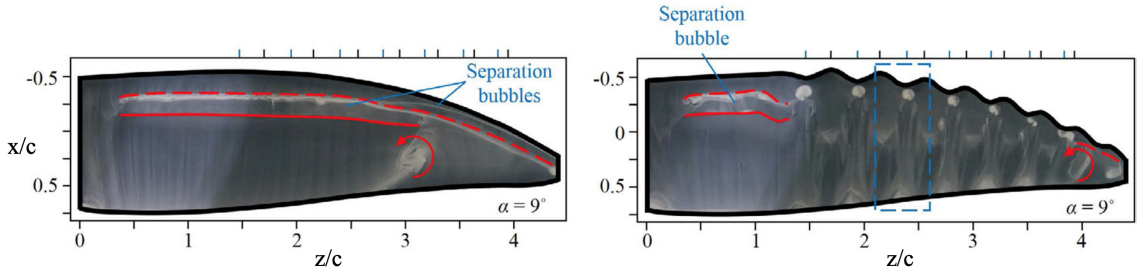

Figure 2.16: Surface-oil-flow visualizations for the baseline (left) and tubercled (right) flipper models at 1.8×10^5 and α=9° [Kim et al. 2018].

As presented in Figure 2.15, the impact of tubercles on the lift curves of airfoils and wings is slightly different. This is because a flipper starts presenting separation at the tip and it propagates inboard as the angle of attack is increased. On the other hand, the separation of a full-span wing typically starts at the trailing-edge and then propagates upstream in the chordwise direction until it reaches the leading-edge at high angles of attack [Rostamzadeh et al. 2014; Cai et al. 2017]. For simplicity, and given that this research focuses on the effect of tubercles on full-span airfoils, the impact of the tubercles on the flowfield during pre-stall and post-stall phases will be described only in the context of the airfoil scenario.

Pre-stall

The majority of research on tubercles has been conducted in laminar or transitional flows with Reynolds numbers ranging from 1.2×10^5 to 5×10^5. In this conditions the boundary layer is typically laminar and it becomes turbulent as it evolves downstream in the chordwise direction, usually after a laminar separation bubble (LSB). This flow phenomenon can be described as follows: due to its inherently reduced kinetic energy, a laminar boundary layer might separate from the airfoil surface as a shear layer if the adverse pressure gradient is too strong. This detachment creates a bubble with reverse flow inside it. The disturbances enhance the momentum transfer, eventually reducing the reverse flow region and allowing the reattachment of the turbulent boundary layer. If the Reynolds decreases, the viscous effects dominate over the inertial effects, and consequently the momentum transfer that allows reattachment decays. As a result, the reattachment is delayed and appears later, increasing the size of the laminar separation bubble [Dellacasagrande et al. 2020]. At low angles of attack, laminar separation bubbles have been commonly detected for 2D airfoils and finite wings without tubercles. It has been identified that this bubble moves towards the leading-edge with the increase in the attack angle [Cai et al. 2017; Rostamzadeh et al. 2014; Kim et al. 2018].

Even at zero angle of attack, the leading-edge tubercles shed two counter-rotating vortices that are convected downstream and separation occurs right after the troughs regardless of the amplitude or wavelength of the tubercles. However, the turbulence intensity increases rapidly past the leading-edge of the troughs sections, enhancing the flow reattachment further downstream and therefore forming a LSB. This flow pattern has been observed with airfoils and finite wings [Rostamzadeh et al. 2014; Kim et al. 2018]. Low negative pressure regions are formed on the troughs whereas the suction peaks over the peaks are mitigated. According to experimental surface pressure measurements along the chord, the chordwise pressure distribution at the trough span positions is more similar to the baseline distribution while the peaks show a reduced suction peak with an adverse pressure gradient smoother than that of the unmodified airfoil [Rostamzadeh et al. 2014; Cai et al. 2017; Kim et al. 2018]. For higher angles of attack in pre-stall region, the periodic peak-trough flow pattern becomes more visible. The lateral velocity towards the peaks is enhanced and the suction peaks at the troughs are sharper. For angles of attack greater than α=4°, the suction peak in the troughs has been found to be already higher than that of the baseline [Kim et al. 2018; Rostamzadeh et al. 2014].

In the case of the full-span wing it is widely accepted in the literature that the lift coefficient is reduced in the pre-stall regime. This reduction becomes more apparent as the angle of attack increases (see black line in Figure 2.15). This response can be interpreted in two ways. First, by looking at the results from Cai et al. (2017) which present the separation region and surface pressure coefficient on the suction side of a smooth and tubercled airfoil for α=8°, 12° and 20° as shown in Figures 2.17, 2.18, and 2.19 in this order. From the near-wall flow pattern at α=8°, it can be stated that for the smooth leading-edge airfoil, the flow is unquestionably two dimensional and fully attached. The authors claim that a minor separation is visible with CFD at the trailing-edge, but it may not be enough to actuate the motion of the tufts. On the other hand, the airfoil with tubercles is already separating. Note from the streamlines that the separation bubble on the troughs is visible. As suggested by Sudhakar et al. (2019), the separation line displays undulating characteristics, showcasing a sinusoidal pattern along the span. This pattern could be attributed to the boundary layer mixing enhancement, or the downwash-upwash effect as explained in Section 2.2.2. The increased separation observed for the airfoil with tubercles could explain the reduced lift coefficient in pre-stall conditions. Secondly, surface pressure measurements can be also used to determine the sectional lift along the span in order to explain the reduced lift for the tubercled airfoil case. Rostamzadeh et al. (2014) followed this approach with experimental data and it was proved that neither the troughs nor the peaks achieved

more lift than the baseline airfoil at α=8°. This can be counterintuitive because as mentioned earlier, for this angle of of attack the suction peak at the troughs is already higher than that of the baseline. However, the C_p curve shows that after the suction peak the curve rapidly falls under the baseline pressure curve, i.e., the adverse pressure gradient is considerably stronger along the troughs compared to baseline.

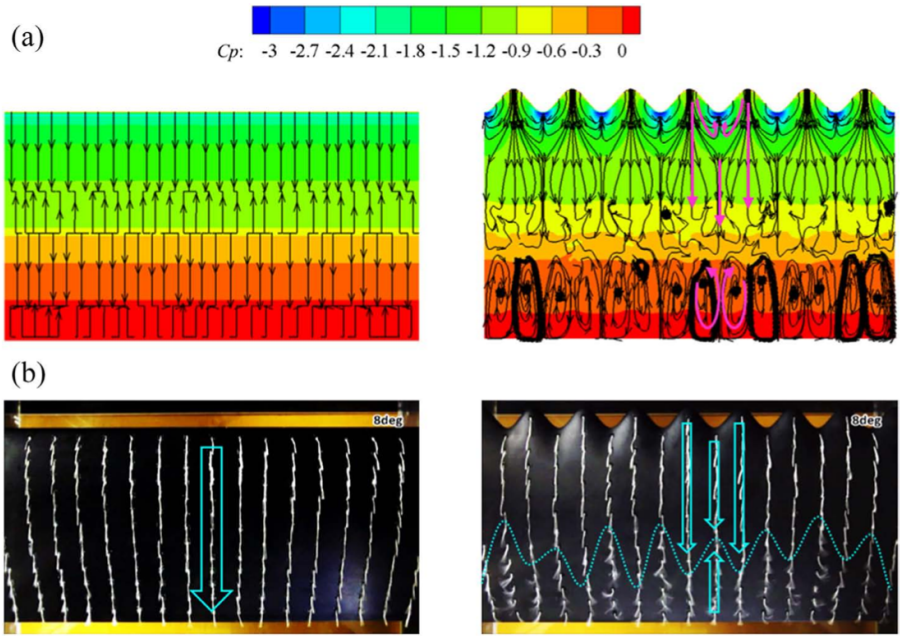

Figure 2.17: Near-wall flow condition over the suction side of the smooth (left) and tubercled (right) airfoils at α=8°and Re=1.8×10^5. (a) Pressure coefficient and streamlines obtained from CFD and (b) tuft visualization from experiments. Extracted from [Cai et al. 2017].

Post-stall

At first glance, when comparing Figure 2.17 to Figure 2.18, the flow patterns over the suction side of the airfoil with tubercles appear very similar. However, it can be observed that the suction peaks in the troughs are stronger at α=12°. The size of the trailing-edge separation has also increased due to the higher angle of attack. On the other hand, the changes experienced by the baseline airfoil are significantly more pronounced, with the separated region extending from the trailing-edge to almost 40% of the chord length. Despite this, the baseline airfoil still achieves higher lift levels than the tubercled airfoil under these conditions.

Figure 2.19 illustrates the suction side of the airfoils at α=20°. At this angle of attack, the baseline airfoil has stalled and the flow over the suction-side is completely separated. Contrarily, the tubercled airfoil displays two stall cells with an attached flow region between them explaining higher levels of lift presented by this airfoil in post-stall regime. Although the figures are not included in this work, Cai et al. (2017) also noted that the flow patterns and pressure distribution on the tubercled airfoil from 16° to 24° were relatively consistent, justifying the approximately constant lift observed in post-stall regime for angle of attack larger than α>16°.

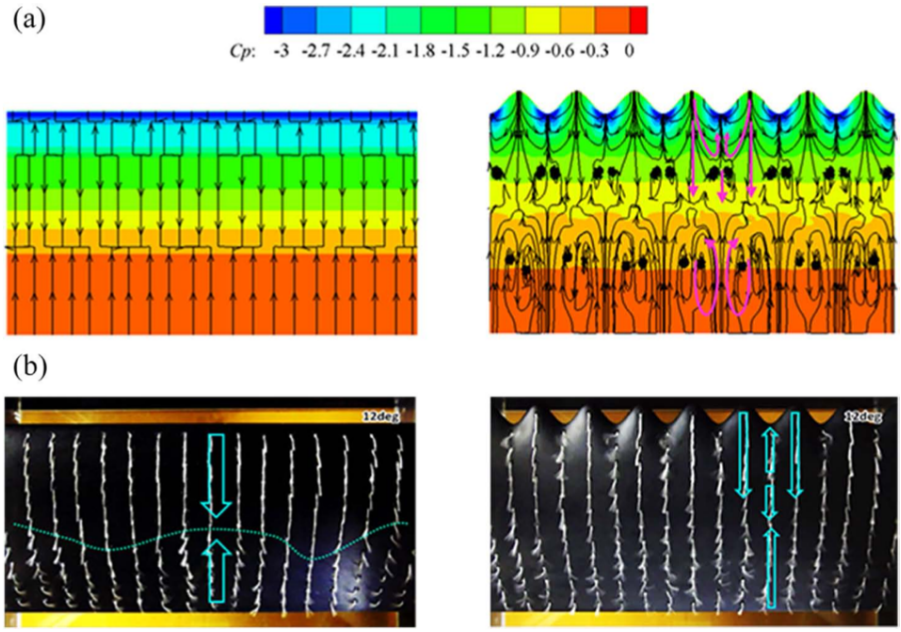

Figure 2.18: Near-wall flow condition over the suction side of the smooth (left) and tubercled (right) airfoils at α=12°and Re=1.8×10^5. (a) Pressure coefficient and streamlines obtained from CFD and (b) tuft visualization from experiments. Extracted from [Cai et al. 2017].

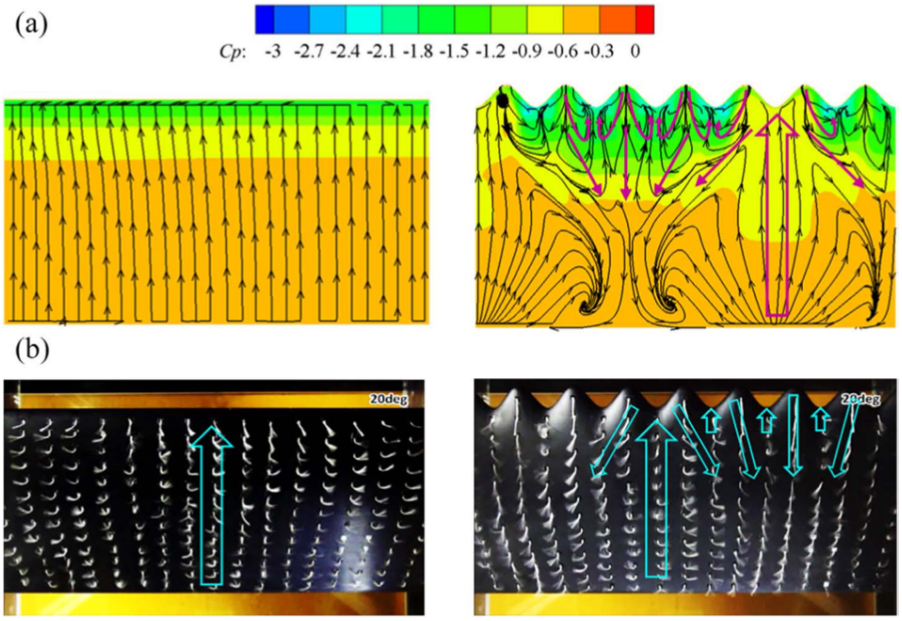

Figure 2.19: Near-wall flow condition over the suction side of the smooth (left) and tubercled (right) airfoils at α=20°and Re=1.8×10^5. (a) Pressure coefficient and streamlines obtained from CFD and (b) tuft visualization from experiments.Extracted from [Cai et al. 2017].

2.2.4. Effect of amplitude and wavelength

The geometry of the tubercles is mainly defined by the amplitude and wavelength of the oscillations, as thoroughly explained in Section 2.2.1. By changing these two parameters, the impact of the tubercles on an airfoil can be noticeably altered. Thus, many researchers have directed their efforts toward investigating the optimum amplitude and wavelength for the tubercles.

Johari et al. (2007) conducted an experimental study of the impact of tubercle amplitude and wavelength on the performance of a full-span wing using a NACA 63_4-021 airfoil at a Reynolds number of Re=1.83×10^5. It was identified that the larger tubercles (A/c=0.12) led to softer stall characteristics but also showed the highest drag levels for the range of angles of attack studied. On the other hand, the smaller amplitude tubercles (A/c=0.025) resulted in better performance in terms of stall angle, maximum lift coefficient and drag increase. The results of the wavelength study suggested that airfoils with smaller wavelengths (λ/c=0.25) reach a higher maximum lift coefficient and an increased stall angle for a smaller increase in drag. Similarly, Hansen (2012) also evaluated the effect of the tubercles on a full-span wing at Re=1.2×10^5. It was also found that smaller amplitude tubercles result in higher maximum lift coefficients and stall angles, whereas larger amplitudes lead to softer stalls, which is consistent with the findings of Johari et al. (2007).

The uniformity across the research is clear. For full-span wings with tubercles, smaller amplitudes have consistently been shown to enhance maximum lift coefficients, stall angles, and reduced drag, while softer stalls can be achieved by increasing the amplitude. Regarding wavelength, higher maximum lift coefficients and increased stall angles are observed for tubercles with smaller wavelengths.

2.2.5. Reynolds number effects

As detailed in Section 2.2.2, the multiple working mechanisms of leading-edge tubercles alter the boundary layer where viscosity plays an important role, thus, the performance of tubercles can be expected to be Reynolds number dependent. In an experimental study with hydrofoils, Custodio (2007) found that rectangular finite wings are sensitive to the Reynolds number up to a point. It was observed that as the Reynolds number increases, both maximum lift and stall angle also increase correspondingly for both tubercled and smooth leading-edge wings. However, the differences in performance between both wings remained consistent for the range of Reynolds number tested Re=9×10^4 to 4.5×10^5. Weber et al. (2010) carried out a series of water tunnel tests with tapered finite wings with 3 and 5 tubercles at Reynolds numbers varying from Re= 2×10^5 to 8×10^5. For both tubercle configurations, the slope of the lift coefficient curve increased with the Reynolds number. Again, it was also observed that the maximum lift coefficient was directly proportional to the Reynolds number. Dropkin et al. (2012) evaluated the Reynolds number effect through CFD. The flowfield around a full-span wing with NACA 63_4-021 was solved for Reynolds numbers varying from Re=1.8×10^5 to 3×10^6. It was concluded that the maximum lift coefficient increased for the smooth leading-edge airfoil as well as for the one with tubercles. On the other hand, the tubercled airfoil proved to be significantly less dependent on the Reynolds number, particularly in post-stall conditions. Therefore, over a wide span of Reynolds numbers ranging from Re=9×10^4 to 3×10^6, it has been demonstrated that higher Reynolds numbers lead to increased lift slopes and maximum lift coefficients. Nevertheless, the performance difference between smooth and tubercled leading-edge airfoils remains.

Studies on the effect of Reynolds number for airfoils with tubercles at Reynolds numbers similar to those used in this research are scarce. Consequently, the impact of Reynolds number on the effectiveness of tubercles under very low Reynolds number operating conditions remains poorly understood. Yasuda et al. (2019) is a notable exception, exploring this effect on a tubercled NACA0012 airfoil within the low Reynolds number range of Re=1×10^4 to 6×10^4, using wind tunnel experiments and CFD. Their results indicate that tubercles function similarly at these low Reynolds numbers as observed at higher Reynolds numbers. Interestingly, at Re<1×10^4, the characteristic abrupt stall behavior observed in the baseline airfoil diminishes. Instead, it exhibits a more gradual and progressive stall pattern similar to that of the tubercled airfoil. Therefore, both the tubercled and smooth leading-edge airfoils demonstrate comparable aerodynamic performance despite marked disparities in their flow characteristics.

2.3. Leading-edge tubercles on dynamic stall

Humpback whales stand out because of their remarkably large flippers when compared to other cetaceans, but what makes them truly distinctive is that they are the sole species to display leading-edge tubercles on the flippers [Fish and Battle 1995]. These unique feature come into play when humpbacks engage in acrobatic hunting strategies to target dense groups of krill and small fish. It is believed that their oversized flippers, in conjunction with the distinctive tubercles, enhance their hydrodynamic performance, ultimately boosting their ability to capture prey.

The humpback whale employs a distinctive technique known as "bubbling" to capture its prey. During this behavior, the whale creates ascending columns of bubbles in a circular pattern, forming a bubble net that corrals the prey into a tight cluster. The process involves the whale releasing bubbles as it swims circularly from the depths toward the surface. Once the bubble net is complete, the whale uses its flippers to pivot and make a sharp turn inside the net before opening its mouth to swallow the prey. Jurasz and Jurasz (1979) observations of humpback whale feeding in the Alaskan coast revealed that the bubble nets range from a minimum diameter of 1.5 meters to a maximum of 50 meters. However, when considering the use of flippers alone and 90° bank angle, a minimum turning diameter of 14.8 meters can be achieved, according to the calculations done by Fish and Rohr (1999). This disparity suggests that humpback whales might employ dynamic stall effects to execute tighter maneuvers, possibly by enhancing lift from their flippers and thereby improving their minimum turning radius.

Segre et al. (2017) conducted observations of humpback whales in their natural habitat, unveiling intriguing insights into their feeding behavior. Their research revealed that just before opening their mouths, humpback whales execute rapid movements with their flippers. This swift motion was postulated to enhance flipper thrust, thereby increasing the velocity of their lunging maneuvers. In an effort to gain a more profound understanding of flipper dynamics, Segre et al. (2017) recorded several humpback whales and captured an interesting instance showcasing that flippers function as dynamic lift generators, rather than static ones. The recorded images shown in Figure 2.20 illustrate a humpback whale engaged in a feeding lunge, with both the upstroke and downstroke lasting 0.8 seconds and having a stroke amplitude of approximately 90°. Taking into account a mean chord length of 0.82 meters for humpback whales, as described in Fish and Battle (1995), and assuming a forward velocity of 3 meters per second, Hrynuk and Bohl (2020) proposes that the motion observed by Segre et al. (2017) can be described by a non-dimensional pitch rate of k=0.2 which clearly falls withing the unsteady aerodynamics regime.

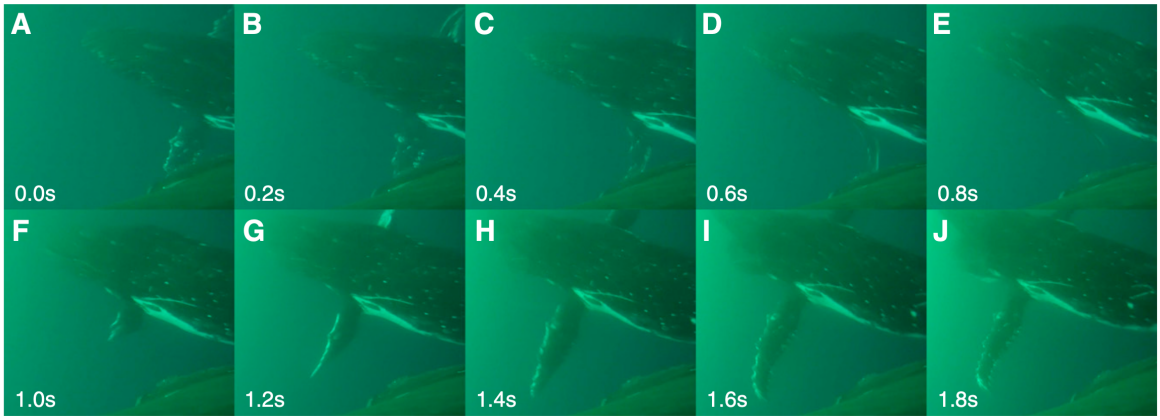

Figure 2.20: A humpback whale performs a flipper-stroke during a feeding lunge. Image extracted from [Segre et al. 2017].

Experimental data reported by Gendrich (1999) suggests that the unsteady force acting on an infinite span airfoil is approximately three times the maximum static lift. When taking this into consideration and, instead of relying on the $C_{l,max}$ of the static case, one takes into account a more realistic $2C_{l,max}$ for the dynamic scenario, the minimum turning diameter initially estimated as 14.8 meters by Fish and Rohr (1999) is halved. This adjustment would bring the estimate more in line with the 1.5

m diameter observed by Jurasz and Jurasz (1979). While research on the effects of tubercles on stationary wings has been extensive, this analysis suggests that a static examination of tubercles alone might not provide a comprehensive understanding of their benefits.

The majority of the research on tubercled airfoils has concentrated on steady flow conditions at fixed angles of attack, with limited exploration of dynamic motions. The existing literature on dynamic stall with tubercled airfoils is summarized in Table 2.1. Drawing definitive conclusions proves challenging due to discrepancies in reported results among various authors. Nevertheless, discernible trends emerge for airfoils oscillating with mean angles below the static stall angle of attack. In this operational regime, tubercles appear to mitigate hysteresis, as initially proposed by Borg (2012) based on wind tunnel experiments with a sinusoidally pitching airfoil. Subsequent studies by Cai et al. (2013) and Nayman and Perez (2022) using CFD simulations supported these findings. Specifically, Nayman and Perez (2022) predicted reductions in lift, drag, and moment hysteresis by 8.9%, 29.4%, and 34.5%, respectively, across all tested conditions compared to the baseline model. Consistent with these results, Wu and Liu (2021) conducted a CFD study evaluating the aerodynamic performance of a sinusoidally pitching wing in dynamic stall. The mean angle of oscillation was consistently below the static stall angle. Introducing the "waviness ratio" parameter (R_w) to quantify the portion of the leading-edge span covered by tubercles as a percentage of the total span, Wu and Liu (2021) observed a 17.1% reduction in peak drag coefficient when tubercles were employed. However, there was also a 9.2% reduction in the maximum lift coefficient. Consequently, the dynamic hysteresis effect demonstrated gradual improvement as the waviness ratio increased. Notably, for the airfoil with R_w=1.0, the hysteresis loop area was the smallest. Despite the consensus on hysteresis reduction, the mechanism driving this phenomenon varies among studies. In general, it is suggested that tubercles enhance flow reattachment as the wing pitches from its peak angle back to its lowest angle as presented in [Borg 2012; Cai et al. 2013; Rohmawati et al. 2020; Nayman and Perez 2022]. However, the results presented by Wu and Liu (2021), which can be seen in Figure 2.21, indicate that the reduction in hysteresis is associated with a decrease in the lift peak, contradicting the findings of other researchers. The observed reduction in lift peak by Wu and Liu (2021) implies an alternative mechanism for hysteresis reduction, emphasizing the complexity of this unsteady aerodynamics phenomenon.

The scarcity of literature on airfoils oscillating at mean angles beyond the static stall angle of attack imposes limitations on the conclusions that can be drawn from existing research. Rohmawati et al. (2020) present force measurements for oscillations with mean angles of α_0=30° which is well above the static stall angle of attack corresponding to a fully separated baseline airfoil in a deep stall condition. Their findings shown in Figure 2.21 indicate that for amplitudes of α_1=5°, the presence of tubercles led to an increase in both lift overshoot and hysteresis. It should be noted that in this flow regime, drag also increased, though to a lesser extent compared to the lift coefficient. For instance, at k=0.125, the lift exhibited a 33% increase compared to the baseline during the upstroke phase, while the drag increased by only 8%. In contrast, Borg (2012) contends that for oscillations around an angle of attack approximately 5° higher than the static stall angle, tubercles offered no advantage in aerodynamic performance compared to the baseline case in terms of lift overshoot and hysteresis. However, it is crucial to acknowledge that Borg (2012) determined the mean angle of oscillation based on the static stall angle of each wing. For tubercled airfoils, this angle was approximately α_0=12°, significantly lower than the α_0=30° used by Rohmawati et al. (2020). Thus, it is evident that research is still insufficient to characterize the effect of tubercles in this operating envelope.

All of the studies mentioned earlier focus on assessing dynamic stall primarily by analyzing aerodynamic forces. However, a critical gap exists when it comes to understanding the flowfield characteristics associated with airfoils featuring tubercles during dynamic stall conditions. The most comprehensive investigation to date has been conducted by Hrynuk and Bohl (2020). This experimental study delved into the impact of leading-edge tubercles on the flow patterns surrounding an airfoil undergoing dynamic stall. The airfoils were pitched from an initial angle of attack of 0° to 50° at constant pitching rates of k=0.1, 0.2, and 0.4, while maintaining a chord Reynolds number of 1.2×10^4. Using molecular tagging velocimetry (MTV), the velocity and vorticity fields around a standard NACA 0012 airfoil with and without leading-edge tubercles were evaluated. Four measurement planes were employed, consisting of two aligned with the peak and trough and two equally spaced in between (referred to as 'near peak' and 'near trough'). These measurement planes allowed for a comprehensive examination of dynamic stall vortex dynamics by tracking parameters such as location, core radius, and circulation.

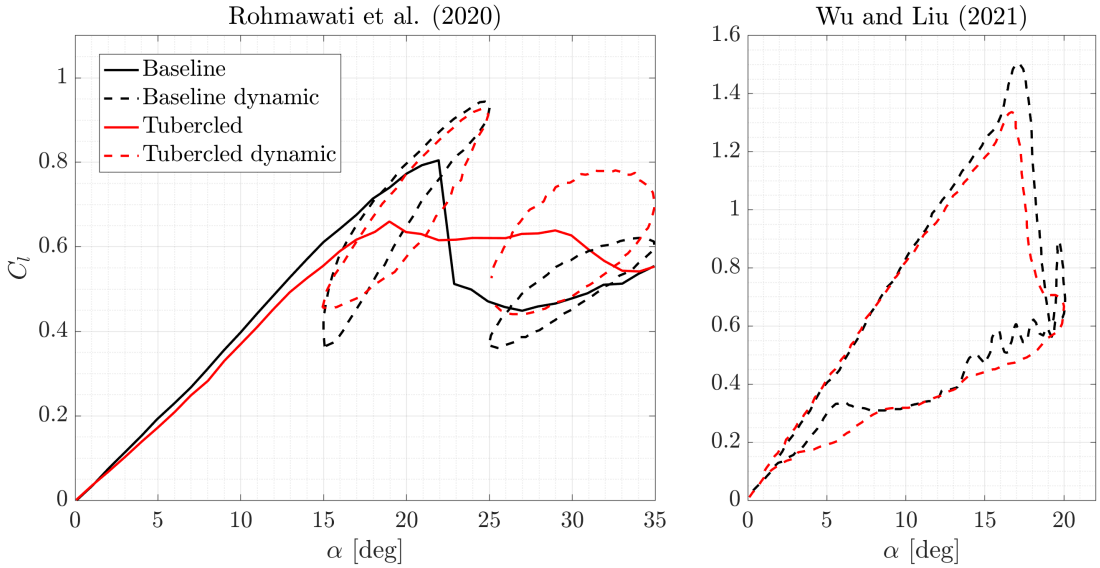

Figure 2.21: Effect of the tubercles on the lift curve of airfoils undergoing pitching oscillations. Data extracted from [Rohmawati et al. 2020] (left) and [Wu and Liu 2021] (right).

Although aerodynamic forces were not directly measured, the authors asserted a strong correlation between dynamic lift and the circulation of the DSV. Therefore, DSV circulation and location were used as indicators to estimate the lift of both the airfoils. Hrynuk and Bohl (2020) noted that over the peak of a tubercle, the DSV formed further back along the chord and at a steeper angle compared to the baseline airfoil. This essentially delayed the initiation of dynamic stall in that region. On the other hand, in the trough span position of the tubercled airfoil, the DSV appeared earlier than on the baseline airfoil but still farther back from the leading-edge. The center of rotation of the DSV on the tubercled airfoil was typically closer to the suction surface, even during the late stages of the pitching motion when flow separation had begun. In particular, it was observed that the DSV in the tubercled airfoil dissipated more slowly, especially at the same pitch rate as the baseline. The authors argue that the combination of these factors enables a tubercled airfoil to generate increased dynamic lift over an extended period compared to a smooth leading-edge airfoil. It was also suggested that if these features are integrated into the design of systems where enhanced dynamic lift is desirable, such as wind turbines and micro air vehicles, tubercles could potentially lead to improved performance. For example, in the case of wind turbines, this could result in greater power generation during unsteady wind conditions.

It is important to note that while this study provides detailed insights into DSV formation and convection, it does not assess the reattachment phase, and therefore does not allow for hysteresis evaluation. Additionally, the visualization of the flowfield is limited to just four planes. The authors speculate that the findings from the peak and trough planes are representative of all peak and trough planes along the span of the wing, except for those closest to the walls where wall effects may be dominant. To prove this hypothesis and gain a comprehensive understanding of the flow around the entire wing, a three-dimensional flowfield visualization is necessary. Such an analysis would clarify the dynamics of the DSV across the entire airfoil span. Furthermore, it would help determine whether the compartmentalization flow mechanism observed in the static case with tubercles is also present in dynamic scenarios.

Reference	Motion	Methodology	Airfoil NACA	k	$Re \times 10^{-5}$	c[mm]	AR	A/c	λ/c	Forces	Hysteresis
Borg (2012)	Sinusoidal oscillation around $c/4$ • α_0=α_{ss}-3°and α_{ss}+5° • α_1=5°and 7°	Wind tunnel. Only forces are measured.	0021	0.08	1.3	100	2.5	0 – 0.12	0 – 0.5	• For α_0=α_{ss}-3°tubercles reduce lift overshoot • For α_0=α_{ss}+5°tubercles offered no advantage in performance	• Reduced hysteresis for α_0=α_{ss}-3°
Cai et al. (2013)	Sinusoidal oscillations around $0.4x/c$. • α_0=10°, 15°and 20° • α_1=5° • α_{ss}=20°	• CFD • Only one wavelength is simulated. • Spalart-Allmaras model	63_4-021	0.1	2	100	-	0.12	0.25	• For $\alpha_0 \approx \alpha_{ss}$ aerodynamic forces are more stable. • Increased consistency with tubercles.	• Tubercles enhance the reattachment and reduce hysteresis at high angles of attack $\alpha \approx \alpha_{ss}$.
Wang et al. (2014)	Sinusoidal oscillations. • α_0=0° • α_1=10°and α_1=20°	• CFD • Only one wavelength is simulated. • URANS $k-\omega$ SST	0010	3	10	N/A	-	0.05	0.25	• Leading-edge protuberances have little effect on the forces. • The pressure distribution of the baseline wing is between those of the modified wing in the peak plane and the trough plane.	n/a
Rohmawati et al. (2020)	Sinusoidal oscillations around $c/4$. • α_0=20°and 30° • α_1=5° • α_{ss}=23°	• CFD • URANS $k-\omega$ SST • Water tunnel experiments.	0018	0.045, 0.06, 0.125	1.4	250	1.6	0.05	0.08	• In post-stall region tubercles improve lift force (more in the upstroke motion than in the downstroke). • The increase in drag is less than the increase in lift.	• Reduced hysteresis in pre-stall regime. • Increased hysteresis in post-stall regime.
Hrynuk and Bohl (2020)	Constant pitch rate from 0 to 50 deg around $c/4$	• Wind tunnel • Molecular Tagging Velocimetry (MTV) • Forces were not measured	0012	0.1, 0.2, 0.4	0.12	120	3.1	0.04	0.24	• DSV for the tubercled airfoil was typically closer to the suction surface. • DSV for the tubercled airfoil convected away slower than for the baseline • Tubercled airfoil to generate more dynamic lift for a longer periods of time	n/a
Wu and Liu (2021)	Sinusoidal oscillation around $c/4$ • α_0=10° • α_1=10°	• CFD • URANS $k-\omega$ SST	0015	0.05	3	200	1.5	0.025	0.2	• Reduced drag peak. • Lift overshoot is also mitigated but to a lesser extend.	• Reduced hysteresis the higher the waviness ratio.
Nayman and Perez (2022)	Sinusoidal oscillations. • α_0=10°and 15° • α_1=10°and 14°	• CFD • URANS and DDES	0012	0.1, 0.15, 0.25	1.2 - 6	152.4	1	0.02 – 0.04	0.07 – 0.14	• Minimal change in maximum lift. • Reduction in maximum drag and moment.	• Tubercles reduce lift and drag hysteresis by 8.9% and 29.4% respectively. • Tubercles reduce moment hysteresis by 34.5%. • Airfoils with the larger tubercle amplitude and wavelength achieved the highest hysteresis reduction.

Table 2.1: Summary of variations in aerodynamic performance in the previous leading-edge tubercles study cases under dynamic stall conditions.

3

Methodology

This chapter is organized into three main parts. Section 3.1 offers a comprehensive explanation of the experimental framework. Section 3.2 provides an overview of the computational fluid dynamics (CFD) methodology specifically developed for this research. Concluding the chapter, Section 3.3 examines the data post-processing techniques utilized in this study during the analysis of the results.

3.1. Experimental methodolody

This section delineates the experimental methodology utilized in this research. It begins with Section 3.1.1, which offers a detailed overview of the experiment's design, including the test section characteristics, the airfoil model, the dynamics-controlling actuator, and the seeding system. Following this, Section 3.1.2 explores the fundamentals of particle tracking velocimetry (PTV) which is the flow measurement technique employed during the experiments. The PTV setup is described in Section 3.1.3. This is followed by a discussion on the image post-processing methods in Section 3.1.4. Finally, the technique utilized for accurately positioning the airfoil within the PTV velocity flowfield at the correct angle of attack is described in Section 3.1.5.

3.1.1. Experiment design

Test section

Experiments were conducted in the W-Tunnel at the Aerodynamics Laboratory of TU Delft, designed for low-speed aerodynamic testing (see Figure 3.1.a). Characterized by its open circuit and powered by a centrifugal fan, the W-Tunnel can be equipped with three different contractions and test sections, depending on the requirements of the experimental tests. For the current experiments, the test section with a cross-sectional area of 0.6×0.6 m^2 and a length of 1.2 m presented in Figure 3.1.b was utilized.

Control over the free-stream velocity was achieved through adjustments to the fan's rotational speed. Within the chosen test section, a maximum free-stream velocity of approximately 16 m/s could be achieved. However, measurements were conducted at a controlled free-stream velocity of U_∞=5 m/s. This setting, provided an environment for precise aerodynamic observations using particle tracking velocimetry. The selected velocity corresponds to a Reynolds number Re=3.3×10^4, calculated based on the chord length of the airfoils c=0.1 m. This setup successfully maintained consistent and reliable free-stream conditions, facilitating a focused investigation into the dynamic stall phenomenon of airfoils with and without tubercles.

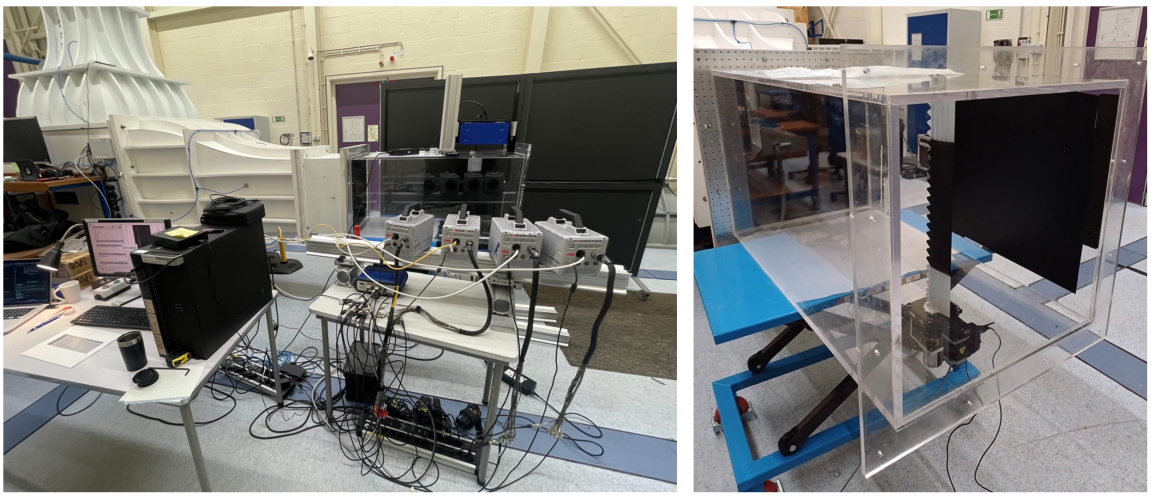

(a) (b)

Figure 3.1: Photos of (a) the W-tunnel and (b) the 0.6×0.6 m^2 test section with the A10L25 airfoil installed.

Airfoil models

The symmetric NACA 0021 airfoil, chosen as the baseline geometry for this study, closely resembles the cross-section of the humpback whale flipper [Fish and Battle 1995]. Beyond its biological mimicry, this airfoil has been commonly used as a generic model for turbine blade cross-sections, bridging the gap between natural inspiration and practical engineering applications. Its selection is further justified by its close similarity to the symmetric NACA0020 and NACA0015 airfoils, which have been extensively used in prior studies to explore the influence of leading-edge tubercles under both static and dynamic conditions [Miklosovic et al. 2007; Borg 2012].

The leading-edge of the tubercled airfoil models is described by a sinusoidal curve as,

$$x_{LE} = Asin(2\pi z/\lambda) \tag{3.1}$$

where the amplitude A is defined as half the chordwise distance between the leading-edge of the peak and the trough, and the wavelength λ is the span between two successive peaks, as shown in Figure 3.2. Following the methodology used by Borg (2012) and Johari et al. (2007), the baseline airfoil is stretched between the leading-edge and 30% of the chord length, which corresponds to the chordwise position where the maximum thickness is reached. In this way, the thickness-to-chord ratio is not maintained across the span, but the airfoil shape for x/c>0.3 is preserved and therefore identical to that of the baseline airfoil.

To isolate the effect of the tubercles, two tubercled airfoils as well as an airfoil with an smooth leading-edge were tested. The three full-span airfoil models with tubercle amplitudes A/c=[0, 0.05, 0.1] are denoted as the baseline, A05L25, and A10L25, respectively. Throughout this work, the baseline airfoil is also referred to as a smooth leading-edge airfoil to emphasize the fact that this airfoil has no tubercles along the leading-edge. Each of the three airfoils maintains a mean aerodynamic chord of c=0.1 m, spans b=0.6 m, and features a tubercle wavelength λ=0.25c. Illustrations of both the baseline and tubercled airfoils can be found in Figure 3.2.

Designed in SolidWorks, the trio of airfoils was 3D printed using stereolithography. To prepare the models for the PTV analysis, each airfoil underwent a finishing process: sanding to eliminate surface inconsistencies followed by an application of matte black paint, enhancing their suitability for the PTV flow measurement technique.

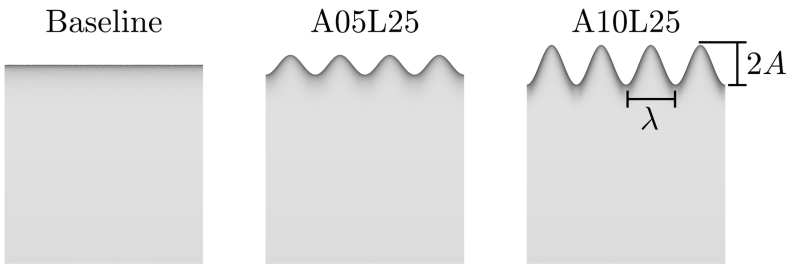

Figure 3.2: Geometry of the baseline and tubercled airfoils used in the present research.

Actuator

The experiments conducted in this study utilized a constant pitch-up and hold motion, a methodology previously adopted in related research on smooth and tubercled airfoils [Jumper et al. 1987; Gendrich 1999; Hrynuk and Bohl 2020]. This approach offers a simpler alternative to the sinusoidal pitching motion, which is another method commonly used in the exploration of the dynamic stall phenomenon. The airfoils underwent a pitch-up from α=0° to a final angle of attack α_1 of 30° and and 55° remaining there for approximately 6 convective times ($t_{upstroke} = 6c/U_\infty$) to allow for the downstream convection of the DSV.

To achieve the desired motion, the airfoil was dynamically controlled using a rotary stage manufactured by Zaber Technologies Inc. Specifically, the model utilized was an X-RSB120AB-E08, which incorporates a high-torque motor and a 120 mm circular base, ideal for securely mounting the airfoil onto the stage.

The actuator was attached to the lower wall of the wind tunnel and connected to the airfoil via an aluminum support designed and manufactured in-house as shown in Figure 3.3. To ensure the airfoil underwent pure rotation during the pitch-up motion, a smooth bolt was fastened to the opposite end of the airfoil, rotating within a bearing attached to the wind tunnel's top wall. The final disposition of the airfoil inside the test section can be seen in Figure 3.1.b.

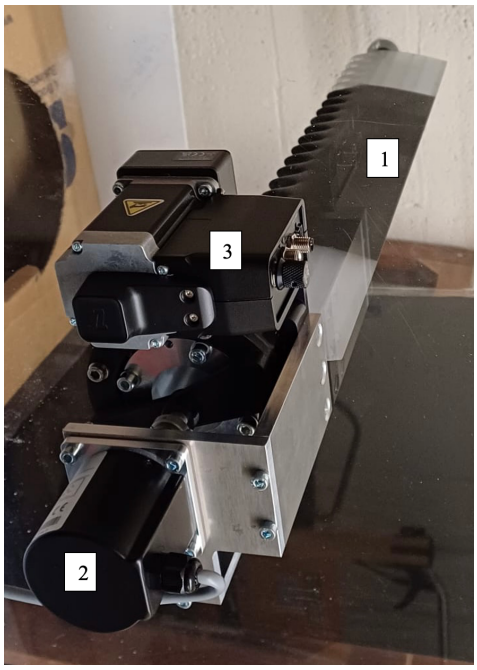

Figure 3.3: Actuator + encoder arrangement. Marked are the A10L25 airfoil (1), encoder (2), and actuator (3).

The actuator is integrated with a controller that interfaces with computers using Zaber Launcher software, enabling motion control via a Python script. However, it lacks a built-in position reader. Therefore, for precise tracking of the airfoil angle during the pitching motion, an Elap srl REV620 encoder was utilized. This encoder was connected to the rotary stage through a KUP-1010-B shaft coupling, allowing for ±0.25mm of shaft misalignment, thereby ensuring accurate measurement of the incidence angle during movements.

A LabView program was employed to synchronize the cameras with the motion of the airfoil, utilizing the encoder to record the angle of incidence at a sampling rate of 2000 Hz. Camera triggering was managed by a signal sent to the programmable timing unit (PTU) by the software, initiated when the airfoil reached α=0.5° during the pitch-up phase. This real-time triggering was enabled by the NI Compact RIO hardware, ensuring that all measurements commenced at the same phase of the pitch-up movement over all the cycles.

As aforementioned, the airfoils underwent a pitch-up and hold motion with two maximum angles of attack α_1=30° and 55°, and two different pitching rates of $k = \dot{\alpha}c/2U_\infty = 0.05$ and 0.1. This experimental choices resulted in a total of 4 different motions as presented in Table 3.1. Each motion type was repeated for the three available airfoils resulting in a total of 12 tests.

	Pitching rate k	**Maximum angle of attack α_1**
Motion 1	0.05	30
Motion 2	0.05	55
Motion 3	0.1	30
Motion 4	0.1	55

Table 3.1: Summary of the motions tested on the three airfoils during the experiments.

The stage motion data obtained from encoder readings for a scenario with a maximum angle of attack of α_1=30° is presented in Figure 3.4 for both k=0.05 and 0.1. The timing utilized in this study is normalized time ($t^* = tU_\infty c$), where t^*=0 is defined as the moment the airfoil reaches α=0.5°. The ideal motion, denoted as the controller input, is also depicted for comparison purposes.

For the scenario with k=0.05, the stage motion closely follows the controller input, with both the stage motion and the controlled input overlapping during the linear pitch-up phase. Conversely, when k=0.1, the maximum acceleration of the stage is insufficient to accurately replicate the controller input, resulting in significantly prolonged acceleration and deceleration phases. Despite the observed limitations of the stage for the $k = 0.1$ motion, which restrict its capacity to faithfully replicate the controller input, this motion profile was also used for the experiments.

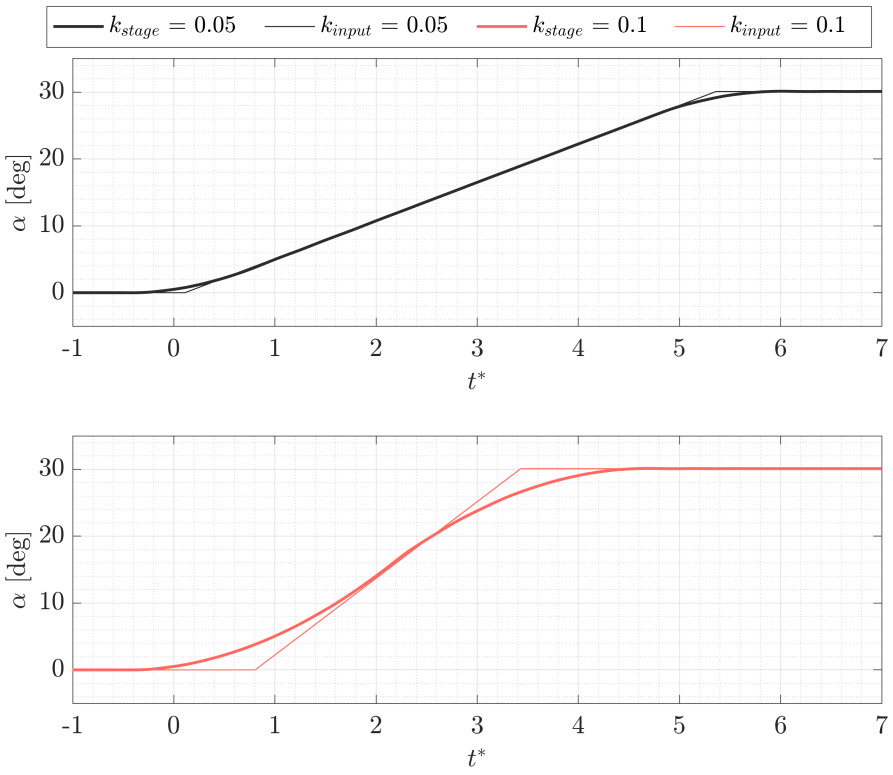

Figure 3.4: Stage motion and the control input for $k = 0.05$ and 0.1.

3.1.2. Fundamentals of Particle Tracking Velocimetry

In this research, particle tracking velocimetry (PTV) was employed to capture the velocity field within the measurement volume. This technique offers substantial benefits as a non-intrusive flow measurement method, typically causing minimal disruption to the flowfield by using tracer particles [Melling 1997]. Unlike methods such as pitot tubes or hot-wire anemometry, PTV can precisely characterize the flowfield within a three-dimensional domain, providing intricate insights into flow dynamics.

This section aims to introduce the basics of the PTV flow measurement technique. However, to fully comprehend how PTV functions, it is crucial to first understand Particle Image Velocimetry (PIV), the foundational technique from which it evolved. Consequently, a concise overview of the PIV working principles, which are also pertinent to PTV, is presented first. Following this, the discussion will progress to 3D PIV with Tomographic PIV, eventually leading to a focus on particle tracking and the Shake-the-Box algorithm, which was utilized for image post-processing in the current experiments.

Working Principles of PIV

Particle Image Velocimetry is a flow measurement technique widely used in educational and research experiments. It is employed to capture the instantaneous velocity field and other fluid-related properties. During a PIV measurement, tracer particles are introduced into the fluid. These particles, capable of light scattering, are uniformly illuminated by a laser light sheet. Using a camera, the position of these tracer particles is recorded at two sequential instances denoted as t and Δt. By analyzing the particle displacements between these images over the known time interval, their velocities can be determined. Consequently, the speed and direction of the flowfield are known as well, as the motion of the particles is considered a reliable representation of the dynamics of the fluid. The typical setup used for planar PIV is presented in Figure 3.5.

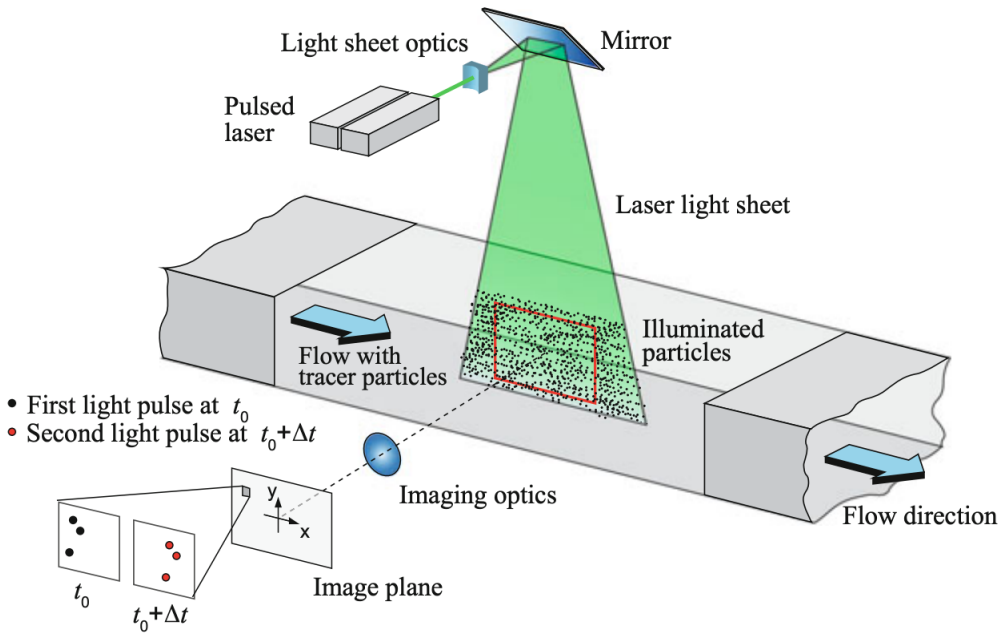

Figure 3.5: Typical planar PIV setup. Image extracted from [Raffel et al. 2018].

After acquiring a pair of images, a complex image-processing approach is employed, incorporating signal-processing and correlation techniques. The initial step involves dividing the entire image into multiple interrogation windows which are treated as individual measurement spaces and are processed independently. The size of these windows typically ranges from 16x16 pixels to 128x128 pixels, depending on the desired resolution. It is important to note that using more interrogation windows improves the resolution of the velocity field but also increases the processing time.

For each interrogation window, the two exposures undergo cross-correlation. This process assesses the similarity between the two time periods based on the displacement of one relative to the other. It results in a discrete cross-correlation map, where the peak position relative to the origin indicates the average particle image displacement within that specific interrogation window. However, the position of the peak aligns with the nearest pixel and may not precisely represent the actual displacement of the particle. To achieve subpixel precision, Gaussian interpolation is often applied to determine the particle image displacement with increased precision.

Once the particle motion is determined in terms of pixel shift between exposures, the velocity can be calculated by considering the magnification factor, denoted as M, and defined in Equation 3.2. This conversion allows pixel-based displacement to be expressed in actual physical terms.

$$M = \frac{sensor\ size}{image\ object\ size} = \frac{pixel\ size \times number\ of\ pixels\ in\ the\ sensor}{FOV} \tag{3.2}$$

To obtain high-quality PIV results, one has to make sure that different requirements are fulfilled during the data collection process. First, the diameter of the particles in the images should be $d_\tau \approx$2-3 pixels to ensure that the movement of the particles can be traced accurately and that peak-locking does not occur [Raffel et al. 2018]. This phenomenon happens if the particle diameter is smaller than the size of a pixel. As a result, the position of the particle cannot be detected with subpixel accuracy, leading to positional errors up to 0.5 pixels. The effective particle image diameter can be determined as,

$$d_\tau = \sqrt{\left(M\, d_p\right)^2 + \left(2.44\lambda(1+M)f\#\right)^2} \tag{3.3}$$

where d_p is the physical diameter of the particles and the second term is the diffraction diameter d_{diff}. For typical PIV configurations, the diffraction limit generally dominates the particle image formation $d_{diff} >> Md_p$. The f-number (or f-stop) $f_\# = f/D$ refers to the ratio of a lens's focal length to its aperture diameter. In PIV measurements the cameras are typically equipped with fixed focal length lenses, and therefore a larger value of $f\#$ can be used to increase the particle image diameter at the expense of less bright particles given the reduced aperture diameter. Furthermore, in 3D PIV, the f-stop number also determines the depth of field: the smaller the aperture (that is, the bigger the f-number), the greater the depth of field but the darker the images. On the contrary, a small value of $f\#$ corresponds to bright images with a much smaller depth of field. Therefore, in 3D PIV, $f\#$ is also used to adjust the depth of field to at least match or be bigger than the illuminated measurement volume.

The time separation between exposures should be carefully chosen to ensure that the majority of particles are imaged within the same interrogation window during both exposures. This condition is crucial for the cross-correlation process within each window and is often referred to as the "maximum displacement criteria" [Raffel et al. 2018]. To determine the appropriate time separation between laser pulses, one considers the maximum expected freestream velocity of the flow and the magnification factor. This information is used to calculate the displacement of the particles between the two laser pulses. The light pulse separation is then defined to ensure that the particle displacement remains less than a quarter of the size of the interrogation window, thereby preventing the particles from moving outside of the interrogation window between the two light pulses.

3D PIV and particle tracking

By using two cameras that capture the illuminated flow particles from different directions, the "classical" planar PIV method can be extended to allow for the measurement of all three velocity components within the light sheet. However, due to its inherent reliance on a light sheet to illuminate particles, it can only determine particle velocities within the illuminated plane. This limitation can result in missing data for the direction perpendicular to the laser plane and potential interference with in-plane velocities. To address this constraint and broaden the applicability of PIV to diverse aerodynamic challenges, the introduction of Tomographic PIV, often referred to as "TomoPIV", has proven valuable. This more advanced method for measuring velocity flowfields builds upon the principles of PIV but extends its capabilities to three dimensions [Elsinga et al. 2006].

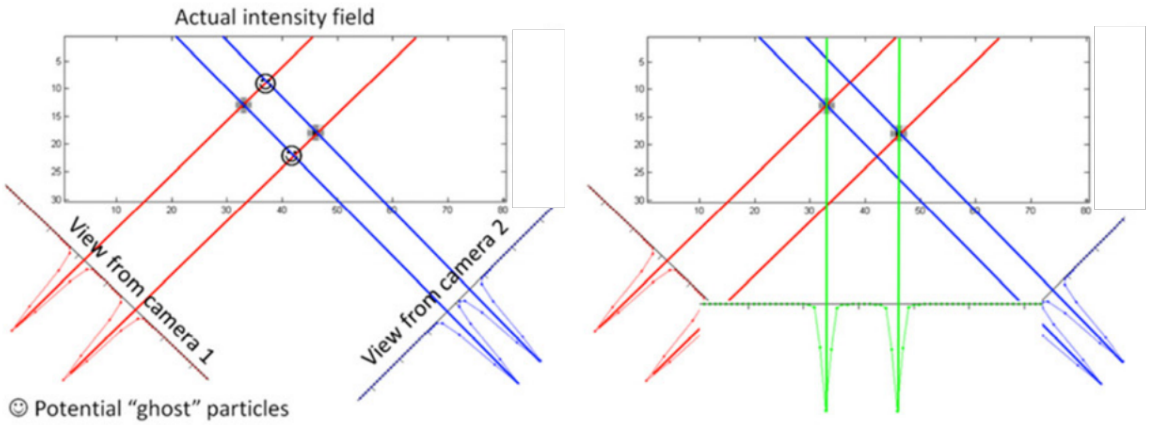

Figure 3.6: Visualizing a 3D particle field: On the left, two views of two particles result in four possible reconstructions. On the right, introducing a third view resolves any concurrent misleading intersections (ghost particles). Image extracted from [Raffel et al. 2018].

The region of interest where the velocity flowfield is to be determined is no longer a simple light sheet but rather an illuminated volume. This volume is created by expanding the thickness of the laser sheet to match the required depth of the field of view while reducing its extension in the other direction obtaining an illuminated volume. Multiple cameras, usually numbering between 3 and 6, are strategically positioned, allowing for observation of the illuminated region from various viewing angles. Similar to the 'classical' PIV methodology, these cameras capture the scattered light from the tracer particles. To achieve this, the depth of focus of the imaging system must match or exceed the thickness of the illuminated volume.

The analysis of particle motion is conducted through three-dimensional cross-correlation, as is done in planar PIV. However, the challenge in extending PIV into three-dimensional space lies in the reconstruction of 3D volumes from the set of pairs of images obtained with each camera. This requires the use of a tomographic reconstruction algorithm to address this complex inverse problem, often characterized by ill-posedness and the presence of multiple potential solutions. As noted by Raffel et al. (2018) in their book, "A single set of projections can result in many different 3D objects". A comprehensive discussion and examination of tomographic reconstruction algorithms, such as the Multiplicative Algebraic Reconstruction Technique (MART), are available in Elsinga et al. (2006) and Raffel et al. (2018).

Although delving into a detailed description of these 3D reconstruction algorithms falls beyond the scope of this methodology chapter, a simple example aiming to shed light on the working principle of the reconstruction algorithms is presented in Figure 3.6. On the left, the intensity fields captured by two cameras are visible in red and blue. Note that the combination of the two measured intensity fields leads to four possible particle locations but only two are genuine. The two particles that are not actually in the domain but could potentially be detected are known as "ghost particles". On the right, a third camera is introduced enabling the detection of the so-called ghost particles, and therefore facilitating the accurate identification of the actual positions of the two particles. In simpler terms, this process exemplifies the logic behind the 3D reconstruction approach, which transforms the images acquired from multiple cameras into a discrete 3D representation where particles are represented as intensity peaks in a voxel space.

According to Schanz et al. (2016), TomoPIV comes with specific limitations. Notably, the presence of ghost particles can substantially impact the accuracy of the velocity vector field, particularly when dealing with high particle image densities. Moreover, the cross-correlation approach employed in TomoPIV involves spatial averaging across interrogation volumes, which can result in the smoothing of velocity gradients and small flow structures. Furthermore, this method is known to consume significant amounts of computational resources during image processing.

In response to these limitations, Schanz et al. (2016) introduced the 'Shake-The-Box' PTV or 4D-PIV technique. This flow measurement approach builds upon the foundational principles of Tomographic PIV while addressing some of its drawbacks. By employing a lagrangian particle tracking (LPT) scheme, the Shake-the-box (STB) algorithm introduces a novel approach and reverses the typical sequence of evaluation used in previous PIV methods. In traditional methods, particle distributions are initially determined, followed by the deduction of velocity through cross-correlation. However, STB utilizes existing velocity information to estimate the particle distribution for the next time step. This approach allows the flow itself to actively contribute to the reconstruction process, resulting in a substantial reduction in the number of iterations required and, consequently, a decrease in processing time.

3.1.3. PTV setup

The velocity field was measured on the suction side of the airfoil with 3D time-resolved PTV using the setup and the wind tunnel arrangement illustrated in Figure 3.7. Four Photron Fastcam SA1.1 high-speed cameras were employed. These cameras feature a 1024×1024 pixel^2 sensor with a pixel pitch of 20 µm and a maximum image acquisition rate of 5400 Hz. To optimize memory usage, the camera sensors were cropped to 768×1024 pixel^2, allowing for storage of up to 7276 images. The airfoil motion was captured at a frequency of 2000 Hz, resulting in a total sampling duration of 3.6 seconds. Considering that the cameras were triggered after the airfoil crossing α=0.5° and that the airfoil remained for 6 convective times at a maximum angle of attack position, the total sampling time allowed for the measurement of more that 10 complete cycles for all the motions tested.

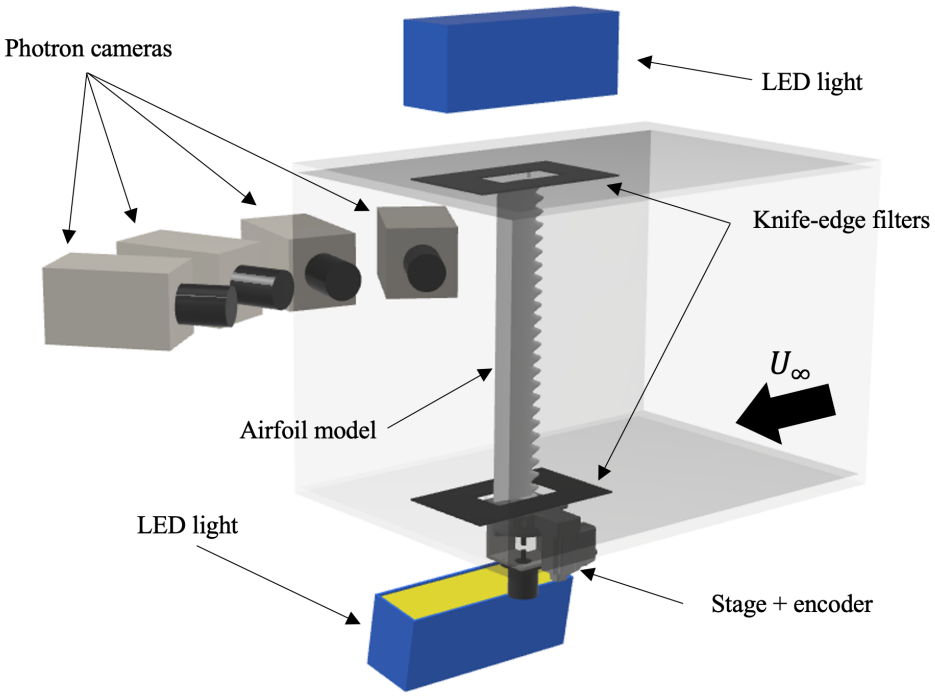

Figure 3.7: Experimental arrangement in the W-Tunnel and PTV system layout.

The cameras were arranged horizontally in a linear configuration approximately 1 m from the model, with an angle between them of 40°, as shown in Figure 3.8. Equipped with Nikon 60 mm lenses ($f_\#$=16), this setup resulted in a measurement volume of 180×120×300 mm^3.

The suction side of the airfoil was illuminated using two LaVision LED light sources positioned above and below the wind tunnel section. Furthermore, to prevent illuminating particles that were too close or too far from the cameras, which may lie outside the depth of field, two knife-edge filters were used to match the illuminated region to the measurement volume.

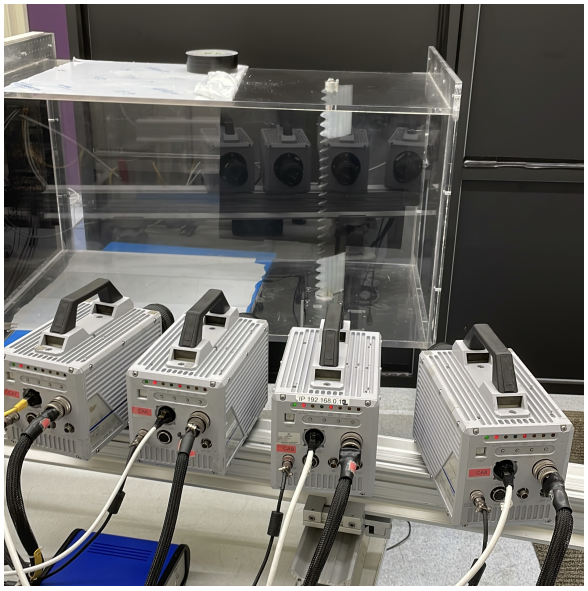

Figure 3.8: High-speed cameras arranged horizontally in a linear configuration.

Particle seeding system

To successfully measure the flowfield using PTV, it is necessary to introduce particles into the flowfield. Hence, the free-stream flow was seeded with neutrally buoyant helium-filled soap bubbles (HFSB) with a nominal diameter of approximately 300 µm [Faleiros et al. 2019]. These were introduced into the settling chamber by a 10-wing, 200-nozzle rake. The pressure values for air, soap, and helium were controlled by a Fluid Supply Unit (FSU), which allowed the pressure for the soap and helium to be set independently.

3.1.4. Image processing

The image sets captured with high-speed Photron cameras were processed using DaVis10 software. A representative image of the particles, as obtained during these research experiments, is displayed in Figure 3.9.a. Although tubercle reflections were initially visible, they were effectively removed by employing the time filter subtraction feature in DaVis10.

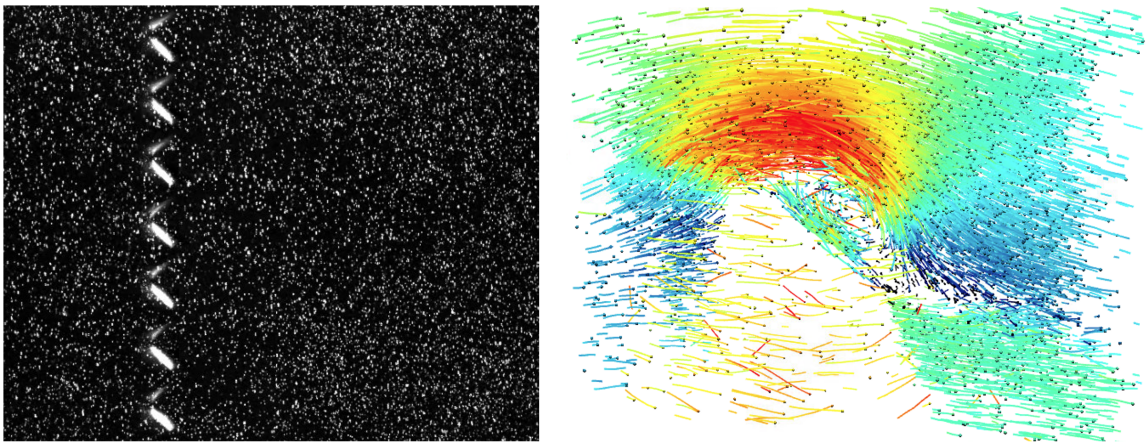

(a) (b)

Figure 3.9: (a) PTV image before processing and (b) particle tracks colored by velocity magnitude, obtained after STB-PTV post-processing.

After applying the Shake-the-Box algorithm, tracks within the measurement volume were identified (see Figure 3.9.b). However, since tracks only provide detailed information about local flow characteristics at specific points in time, velocities and accelerations are only known at the track locations. Therefore, interpolating the track data onto a Cartesian grid is necessary to determine the velocity field across the entire measurement volume.

The binning process requires adjusting two key parameters: the spatial bin size and the temporal bin size. These parameters impact the resolution of the resulting velocity field, the post-processing time and the amount of disk space used for data storage. Thus, this section presents a sensitivity analysis of these parameters for the baseline airfoil undergoing a pitch-up motion up to a maximum amplitude of α_1=30° at k=0.05.

Spatial binning

During DaVis spatial binning, the domain is divided into cubic cells, with their dimensions determined by the user in terms of voxels. In the current experiments, the size of a pixel in the physical domain was 0.3 mm. Consequently, a bin size of 36 voxels was chosen, corresponding to a physical dimension of 10.8 mm equivalent to 0.11c. To complement this setup, a spatial polynomial function of the first order was employed.

The velocity associated with each bin is calculated as the average velocity of the tracks within that bin. However, if the bin size is too small, there may not be enough tracks within it to accurately represent the dynamics of the flowfield. To address this, the software allows the user to specify a minimum number of tracks within a bin required to proceed with the averaging. In cases where no tracks are found within a bin, or the number of available tracks falls below the specified threshold, the velocity field within the bin remains undefined, resulting in velocity gaps in the measurement volume.

Moreover, in DaVis10 the user has the option to define an overlap between bins. This feature helps enhance mesh resolution without requiring a reduction in bin size, thereby reducing the probability of encountering empty bins within the region of interest. In the current research, an overlap of 75% was utilized, resulting in a mesh resolution of 9 voxels or 2.7 mm.

Figure 3.10 illustrates the vorticity field at z/c=0 obtained using different bin sizes for the baseline airfoil pitching up to α_1=30° at k=0.05. As anticipated, finer bin sizes yield higher resolution, as evidenced by the clearer definition of the DSV core. In this specific motion case, no undefined bins were detected, even with the smallest bin size. However, it was noted that for cases with $k = 0.1$, the particle density within the DSV was notably low. Consequently, defining excessively small bin sizes, i.e., smaller than 10.8 mm, led to the emergence of undefined regions within the DSV core.

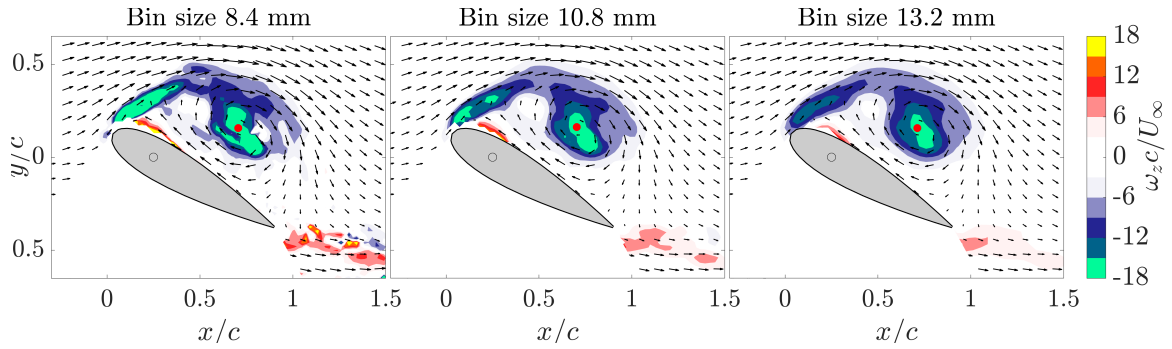

Figure 3.10: Spatial bin size effect on 2D vorticity flowfield obtained with STB-PTV at t^*=6.

While one might assume that a finer binning mesh would require more time for data processing, this is not necessarily true. The primary factor influencing computational time is the overlap between windows. When the overlap increases, the same track may be included in multiple bins therefore increasing the total number of tracks evaluated. Conversely, if no overlap is used and the mesh is finer, each particle is only considered once regardless of the bin size. That being said, for the presented bin spatial size sensitivity study, the overlap was fixed at 75%. However, it was found that finer bin sizes

necessitate more processing time. For instance, post-processing a complete cycle with a bin size of 8.4 mm required approximately 50 minutes, whereas with a bin size of 10.8 mm, the total computation time was reduced to roughly 20 minutes. It should be noted that this is likely due to limitations of the hardware used rather than smaller bin sizes requiring more computational power. With respect the disk memory usage, achieving the finest resolution necessitated 48 gigabytes of disk memory for a full cycle, whereas the medium bin size only required 23 gigabytes. A summary of these statistics is presented in Table 3.2.

Figure 3.11 displays a vorticity iso-surface at $\omega_z c/U_\infty$=-9, indicating the position and shape of the DSV. The finest bin size notably enhanced resolution but also introduced additional noise into the final velocity field. Conversely, increasing the bin size substantially reduced noise while yielding a smoother DSV iso-surface, thereby facilitating subsequent analysis.

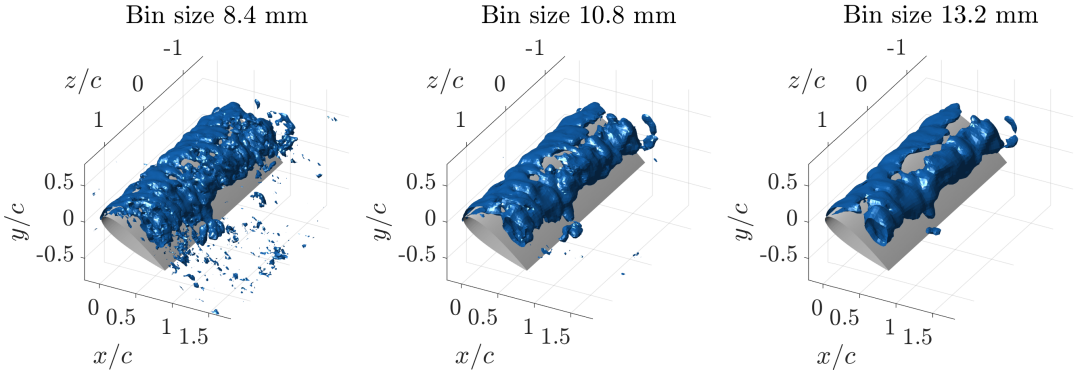

Figure 3.11: Spatial bin size effect on 3D vorticity flowfield obtained with STB-PTV at t^*=6. Iso-surfaces at $\omega_z c/U_\infty$=-9.

Due to limitations in memory and computational time, the finer mesh with a bin size of 8.4 mm was discarded. Consequently, the medium bin size of 10.8 mm was adopted for the remainder of the study. This decision was based on the fact that this bin size did not significantly increase disk usage or computational resources while offering enhanced resolution and comparable noise levels compared to the coarser bin size. Additionally, the coarse mesh failed to capture the vorticity near the airfoil leading-edge due to its limited resolution, which prevents it from accurately representing the velocity gradients.

Bin size	**8.4 mm**	**10.8 mm**	**13.2 mm**
Mesh resolution [mm]	2.1	2.7	3.3
Disk memory (1 cycle) [gb]	23	48	132
Processing time [%]	80	100	200

Table 3.2: Bin spatial size sensitivity analysis.

Temporal binning

During post-processing of a bin, all tracks within the bin for the specific time-step being analyzed are considered. Moreover, to increase the particle count, those particles present within the bin in preceding time-steps, as well as those expected to enter the bin, can also be taken into account. The number of time-steps considered is set adjusting the temporal bin size which defines the time-steps examined prior to and following the time-step undergoing binning. Weighting is applied to the particles, assigning greater influence on the average to particles present within the bin during the time-step undergoing binning, compared to those from previous time-steps that are still under consideration.

Figures 3.12 and 3.13 illustrate the influence of the temporal bin size on both the 2D and 3D vorticity fields. The effect of this parameter was notably less pronounced compared to the spatial bin size. The

DSV core, marked by the red point in the 2D slices, maintained its position consistently irrespective of the temporal bin size. However, the vorticity source at the leading-edge weakened with an increase in the number of considered time-steps. The shape of the DSV appeared to be relatively unaffected by changes in the temporal bin size. Nevertheless, larger temporal bin sizes resulted in a more cohesive and rounded appearance of the DSV.

Determining the optimal setup was challenging given the limited impact of this factor. Considering too many time-steps could potentially mask small flow features in the flowfield. Conversely, considering too few time-steps might increase the risk of having insufficient particles within the bins, resulting in unresolved bins within the volume of interest. Hence, throughout this research, 21 time-steps were included during the binning post-processing corresponding to Δt^*=0.52.

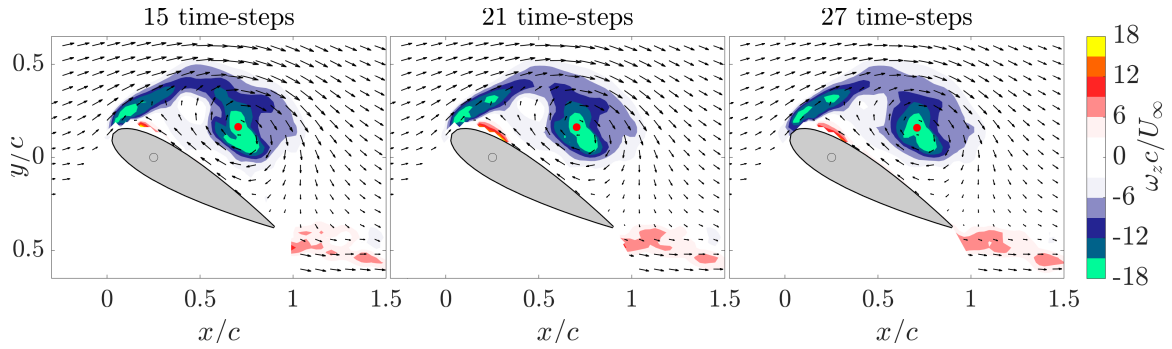

Figure 3.12: Temporal bin size effect on 2D vorticity flowfield obtained with STB-PTV.

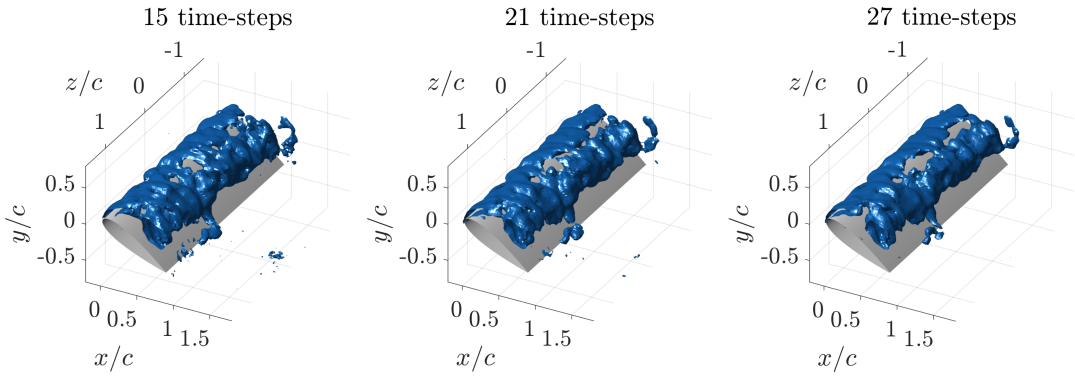

Figure 3.13: Temporal bin size effect on 3D vorticity flowfield obtained with STB-PTV. Iso-surfaces at $\omega_z c/U_\infty$=-9.

3.1.5. Airfoil positioning

After the sets of PTV images are post-processed with the STB-PTV algorithm and subsequently binned, the time-resolved velocity field is obtained. However, for a comprehensive understanding of the flowfield and its interaction with the airfoil, precise positioning of the airfoil within the measurement volume is essential. This ensures that any flow feature identified within the region of interest can be clearly visualized and located in space with respect the airfoil.

The approach employed to locate the airfoil in the PTV domain consisted of three steps: firstly, five markers were painted on the suction side of the airfoil, as depicted in Figure 3.14. Subsequently, these markers were identified in the images captured by the high-speed cameras using a Matlab script partially developed for this study. The implemented image recognition approach benefited from the markers' known shape and color - they were white, whereas the airfoil and the wind tunnel wall opposite the cameras were painted black. As shown in Figure 3.15, although the particles are also white in the images, the markers remained easily discernible even with the particle seeder operating, as their size was significantly larger than that of the particles.

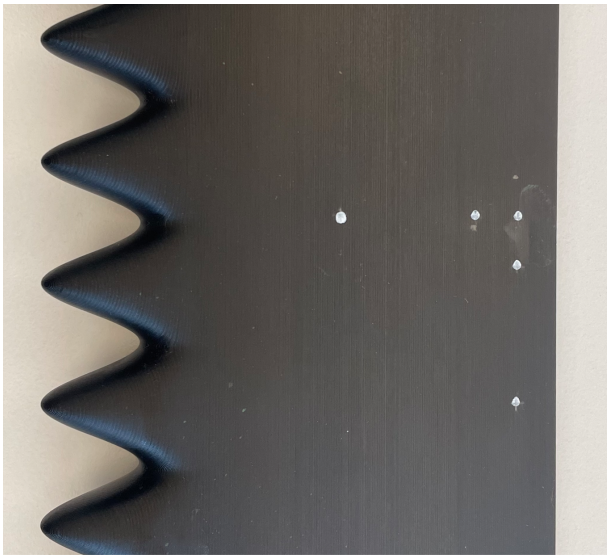

Figure 3.14: White markers painted on the suction side of the A10L25 airfoil.

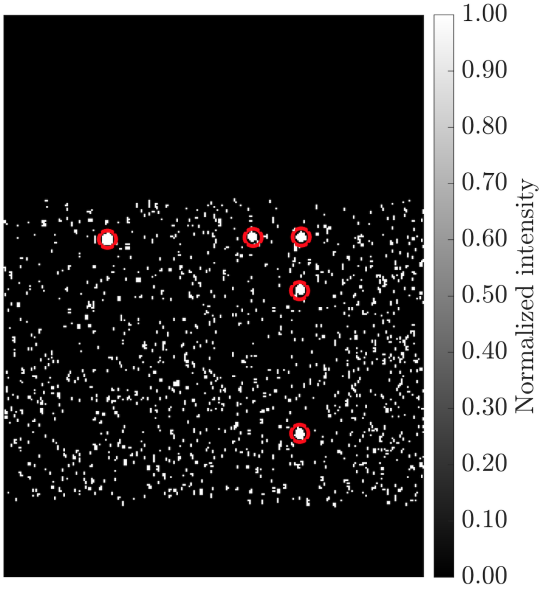

Figure 3.15: Markers identified on an image taken with the high-speed camera.

Upon identifying the markers in the images from all cameras, their spatial coordinates were determined using triangulation, as illustrated in Figure 3.16. Furthermore, by fitting an arc to the path of each of the five markers, the center of rotation for each marker was determined. Following this, a three-dimensional linear regression was applied to fit a line through the set of points, thereby establishing the axis of rotation of the airfoil.

Once the location and incidence of the airfoil were determined for each set of images, a common system of reference for both CFD simulations and experiments was necessary. This step was crucial for two main reasons: firstly, during the wind tunnel experiments, a new calibration was conducted for each airfoil to ensure successful detection and tracking of the particles during post-processing. Thus, the reconstructed velocity fields had a slightly different frame of reference for each airfoil. Secondly, the CFD results used a different frame of reference compared to the experimental data.

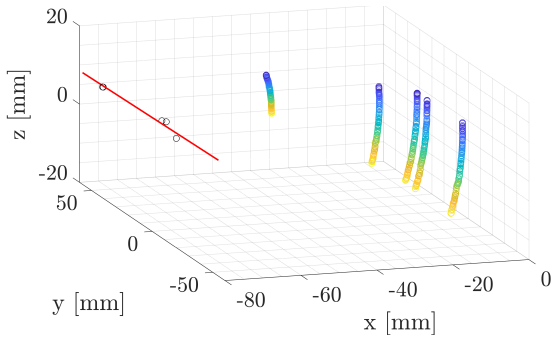

Figure 3.16: Markers' position during the pitching up. Axis of rotation indicated with the red line.

To facilitate flowfield comparison across CFD and experimental data, as well as between different airfoils, all STB-PTV tracks were transformed to the CAD frame of reference, which was already employed in the CFD computations. This transformation was accomplished by computing a rotation matrix and a translation vector for each case using a least squares approach proposed by Wahba (1965). The MATLAB scripts to track markers from multiple cameras, triangulate to 3D world coordinates using camera calibration files, and determine object orientation by matching them to the known marker locations on a CAD model are available on GitHub[1].

[1]MATLAB scripts at https://github.com/MorganL1984/3D-marker-tracking, last accessed January 20, 2024.

Figure 3.17 illustrates the angle of attack of the airfoil during a pitch-up and hold motion with k=0.05 and α_1=30°. The incidence of the airfoil has been determined using both encoder readings and marker tracking, as detailed in the methodology section. While the tracking method exhibits slightly lower accuracy compared to the encoder readings, the results demonstrate strong concordance between the two approaches. Consequently, it is inferred that the airfoil motion can be effectively tracked and spatially located over time.

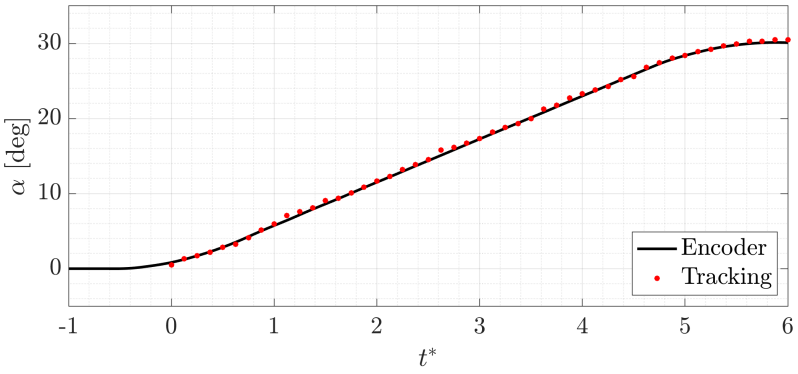

Figure 3.17: Airfoil motion obtained from encoder readings and marker tracking.

3.2. Numerical methodolody

Numerical simulations were conducted using the DelftBlue supercomputer and the OpenFOAM open-source computational fluid dynamics toolbox. For both steady-state and dynamic simulations, the pimpleFoam solver was utilized. This solver, specifically designed for addressing unsteady turbulent flow phenomena, solves the Unsteady Reynolds-averaged Navier–Stokes (URANS) equations on a finite volume mesh. The initial conditions for the transient solver were obtained from the simpleFoam steady-state solver, which was iterated until the residuals of the velocity, pressure, and turbulence fields converged below 10^{-5}.

Regarding the pimpleFoam setup, the nOuterCorrectors was set to 150 iterations. Consequently, the pressure-momentum coupling was recalculated within each time iteration until the pressure and velocity residuals reached values below 1×10^{-4} and 5×10^{-5} respectively. The limit of 150 iterations was never reached and each time step usually converged after approximately 25 iterations. This approach facilitated quicker simulations by allowing larger time steps, while ensuring good convergence levels and a stable simulation [Holzmann 2016].

The turbulence modeling utilized the two-equation model $k-\omega$ SST due to its proven ability to accurately capturing flow separation phenomena [Rohmawati et al. 2020]. Furthermore, this turbulence modeling technique has already been used to simulate both static and pitching airfoils across a broad spectrum of Reynolds numbers [Cai et al. 2017; Wu and Liu 2021].

The OpenFOAM mesh generation tool, SnappyHexMesh, was employed to construct a high-quality hexahedral mesh around the airfoil. Starting from a coarse mesh around the imported airfoil geometry in STL format, SnappyHexMesh then refines it to produce a final smooth mesh which proved to be able to accurately capture the tubercles shape. In the simulations conducted for this research, four layers were employed to ensure that the value of y^+ remained below 0.5 for most of the airfoil, in accordance with the requirements of the chosen turbulence model.

To make the airfoil rotate as intended, a sliding mesh approach was utilized. To do so, a cylinder surrounding the airfoil along the span direction was created as presented in Figure 3.18 effectively dividing the domain in a rotating and a fixed mesh. The diameter of the cylinder was four times that of the airfoil chord, and it was centered at x/c=0.25. Although it has not been presented in this work, a diameter sensitivity study was conducted in the early stages of CFD workflow development, and it was found that further increasing the cylinder diameter had no effect on the final solution. The rotating and fixed meshes were coupled using the CyclicAMI boundary condition, which interpolates

the field between the two meshes and is particularly suitable for patches that share the same outer bounds but have dissimilar inner constructions. The resulting mesh was applicable for both static and dynamic simulations, as the cylinder could be rotated to match the desired angle of attack of the airfoil.

This CFD methodology aimed to mimic conditions found in a wind tunnel. Consequently, the four walls of the wind tunnel test section were represented as solid walls. However, to optimize the simulation and reduce the computational resources needed to run it, the top and bottom wind tunnel walls were modeled as slip walls. This means that while the free-stream cannot penetrate the walls, the influence of the boundary layer is not taken into account. Symmetric boundary conditions were set for the spanwise side boundaries as done in previous research [Visbal and Garmann 2018]. Despite these simplifications, the approach proved to have a minimal impact on the final results and was therefore considered valid.

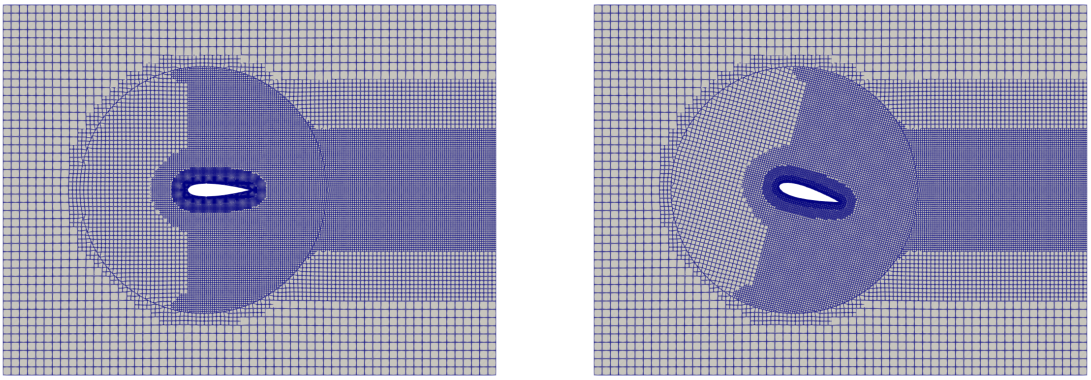

(a) α=0° **(b)** α=15°

Figure 3.18: Sliding mesh at different angles of attack.

3.2.1. Static case

The primary aim of the CFD work in this research was to model the dynamic stall phenomenon of smooth and tubercled airfoils. However, it was deemed necessary to first establish a robust methodology for simulating static conditions. This decision was based on the inherent simplicity of the static case, making it more straightforward to implement. Moreover, the static case required less computation time, which proved to be very useful when adjusting the turbulence parameters, as this process necessitated conducting several tests.

The previously mentioned sliding mesh technique was employed to compute the flowfield around airfoils, both with and without tubercles, at a fixed angle of attack. It is important to note that the static simulation is essentially identical to the dynamic simulation, except for the absence of the mesh motion tool. Thus, consistent mesh configurations, turbulence modeling, and boundary conditions could be applied to both static and dynamic simulations.

Mesh sensitivity study

To obtain a mesh-independent solution, three progressively refined grids were examined, each with a refinement ratio of 2 relative to the previous mesh, representing three distinct grid resolutions: a relatively coarse grid (Mesh 1), a finer grid (Mesh 2), and a further refined grid (Mesh 3). For this mesh sensitivity study, the A10L25 airfoil was utilized, as it was considered that its flowfield was inherently more complex than that of the baseline airfoil, thereby requiring a finer mesh to capture the flow features. Furthermore, the angle of attack was fixed α=15° because at this particular condition, flow separation was expected to occur for the smooth airfoil, while steady stall cells were anticipated for the tubercled wings.

	Mesh 1	**Mesh 2**	**Mesh 3**
# of cells	4,056,117	15,874,062	48,503,650
CPUh	70.46	360.25	1524.66
C_l	0.4953	0.590	0.582
C_d	0.191	0.196	0.196

Table 3.3: Grid sensitivity analysis parameters.

Table 3.3 displays the CPU time needed for the simulation, in addition to the total cell count for each mesh. It also showcases the lift and drag coefficients averaged over the last 0.3 seconds of simulation. A comparison of the aerodynamic force coefficients achieved with the two most refined meshes reveals that Mesh 3 did not produce different results, despite significantly increasing the computational time required for the simulation. Mesh 1 proved to be not fine enough and therefore, Mesh 2 was adopted for the rest of the study.

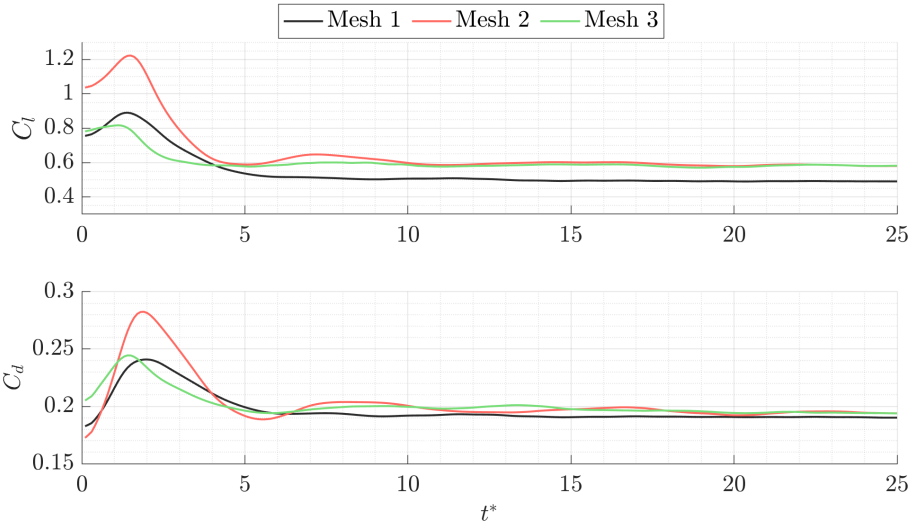

Figure 3.19: Lift and drag coefficient for the three meshes used in the grid sensitivity analysis.

Validation case: baseline airfoil

The validation of the CFD workflow was conducted using the baseline airfoil at an angle of attack $\alpha = 15°$. Experimental findings revealed that the airfoil experienced stall conditions at this angle of attack. Consequently, adjustments were made to the turbulence parameters, including turbulence kinetic energy k and turbulence specific dissipation rate ω, to achieve satisfactory correlation with experimental data. Although, the turbulence parameters could be successfully adjusted to recreate the experimental case at α=15°, the correlation between experimental and CFD results was slightly weaker for angles of attack below α<15°. This is attributed to the difficulty in finding an optimal set of turbulence parameters that could apply to all angles of attack within the pre-stall regime. Consequently, the focus shifted towards accurately predicting the flowfield state at the stall angle of attack, as this is known to be the operational condition where tubercles have the most pronounced influence on the aerodynamics of the airfoil.

The primary difference between experimental and CFD results lies in the fact that the latter predicts a steady flow separation region, whereas observations from experiments reveal that the stall exhibits temporal variability. Consequently, in order to facilitate a comparison between the two cases, the experimental data was averaged in both time and space in the span direction. The resulting averaged experimental velocity field, along with the velocity field acquired through CFD, is illustrated in Figure 3.20, with the area of flow separation delineated by an iso-line at U_x=0 m/s. Analysis of this figure leads to the conclusion that CFD effectively predicts the separation point as well as the extent of the flow separation region in a time-averaged sense.

The boundary layer velocity profiles are plotted in Figure 3.21. Overall, the CFD data demonstrates good agreement with the experimental flowfield. Although there is an initial tendency for the CFD predictions to slightly overestimate flow reversal upstream of x/c=0.3, the stall phenomenon closely mirrors the experimental observations beyond x/c=0.5.

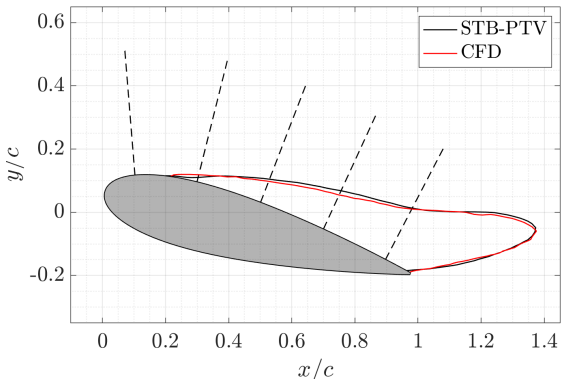

Figure 3.20: Comparison of the separated region obtained from experimental and CFD data. The black dashed lines are used to plot the boundary layer velocity profiles in Figure 3.21.

The comparison of wake momentum loss is depicted in Figure 3.22. In the vicinity of the flow reversal region, both methods present similar wake sizes. However, further downstream, CFD predicts a larger momentum deficit. This can be partially attributed to the influence of the boundary layer on the wind tunnel walls. As explained in Section 3.2, while the CFD simulations account for the presence of walls, they do not explicitly model the boundary layer. Therefore, the blockage effect resulting from boundary layer growth and the subsequent increase in freestream velocity are not taken into account.

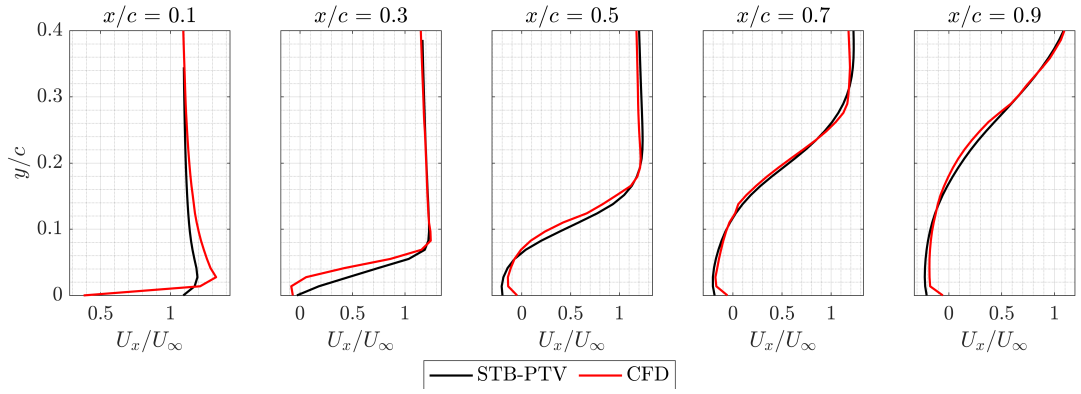

Figure 3.21: Comparison of the boundary layer velocity profiles for the baseline airfoil at α=15°.

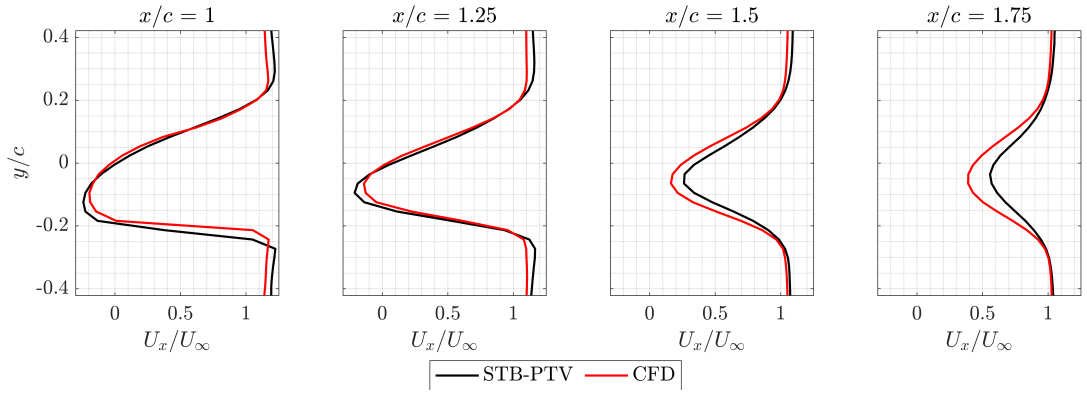

Figure 3.22: Wake evolution comparison downstream of the baseline airfoil at $\alpha = 15°$.

Validation case: A10L25 airfoil

The same CFD workflow employed with the baseline airfoil detailed above, was also used for the A10L25 airfoil at α=15° to evaluate its capability in predicting stall cells and its accuracy regarding stall cell size and streamwise vorticity.

The experimental data presented in this section comprises a temporal average of approximately 3.6 seconds of sampling time. This averaging approach was adequate because the position of the stall cells remained stationary throughout the entire data acquisition period. Thus, temporal averaging augmented the number of tracks available as well as the spatial resolution of the resultant flowfield.

Figure 3.23 illustrates the stall cells represented with an iso-surface at U_x=0 m/s for both experimental and CFD data. Additionally, the counter-rotating pairs of vortices are depicted via contour plots of the streamwise vorticity ω_x at chordwise locations of $x/c = 0.025$, 0.065, 0.105, and 0.145. The comparison between methods reveals noticeable disparities in stall cell positions. This variance could be caused imperfections in the wind tunnel model, predisposing stall cells to align with specific troughs. Furthermore, the fact that CFD is not modeling the boundary layer over the wind tunnel wall boundary layer modeling in CFD may also have an effect.

Despite positional differences, the shape of stall cells and their impact on the flowfield were accurately represented. The streamwise vorticity strength along stall cells intensifies as it convects downstream, resulting in increased downwash over the attached region between consecutive stall cells. Similar to observations in the baseline airfoil, the CFD-predicted flowfield exhibits smoother characteristics, with vortices showcasing greater coherence. This phenomenon is particularly evident in the vorticity contour plots at x/c=0.145.

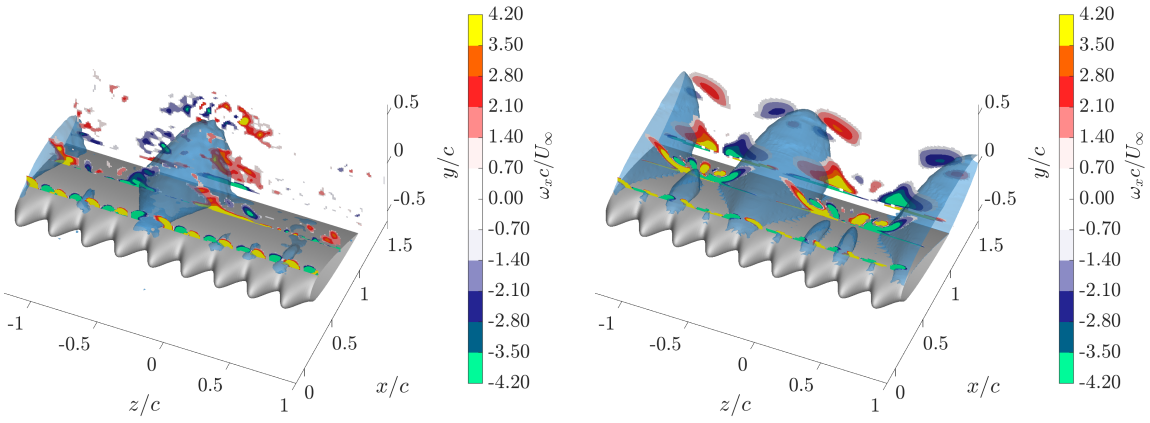

(a) STB-PTV **(b)** CFD

Figure 3.23: Evolution of the streamwise vorticity ω_x over the A10L25 airfoil at an angle of attack of α=15° obtained from experimental and CFD results. The stall cells are indicated with the semi-transparent iso-surface at U_x=0 m/s.

Figure 3.24 depicts a slice normal to the span direction of the stall cell illustrated in Figure 3.23. The iso-line at U_x=0 m/s delineates the flow reversal region. It can be seen that the stall cell obtained from experimental data is higher but extends shorter in the free-stream direction. Nonetheless, the separation point remains consistent in both cases.

Overall, despite variations in stall cell positions, and considering the similarity in primary flow features between CFD and experimental data, the presented CFD methodology was considered sufficiently accurate. Consequently, the workflow employed for both baseline and A10L25 simulations served as the foundation for the dynamic case discussed in Section 3.2.2.

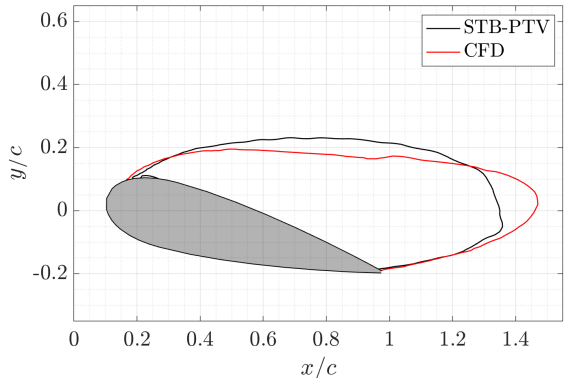

Figure 3.24: Stall cell indicated with iso-line at U_x=0 m/s obtained from experimental measurements and CFD simulations for the A10L25 airfoil at an angle of attack of α=15°.

3.2.2. Dynamic case

The methodology employed for static cases presented in Section 3.2.1 was extended to conduct dynamic simulations maintaining the sliding mesh technique, and therefore requiring minor modifications to the workflow. The dynamic mesh capability available in OpenFOAM was utilized to rotate the airfoil mesh in accordance with the motion specifications defined in the dynamicMeshDict file located within the constant directory. To ensure fidelity in replicating the experimental scenario, the motion data from the encoder readings depicted in Figure 3.4 was fed into the CFD simulations.

Time-step sensitivity study

A time-step sensitivity analysis was conducted to ensure the validity of the numerical calculations. The lift and drag coefficients of the airfoil obtained with time-steps of Δt=2.5×10^{-4} s, 5×10^{-4} s, and 10×10^{-4} s are plotted in Figure 3.25. To aid comprehension, only these time-steps are presented; however, time-steps of Δt=1.25×10^{-4} s and 20×10^{-4} s were also evaluated.

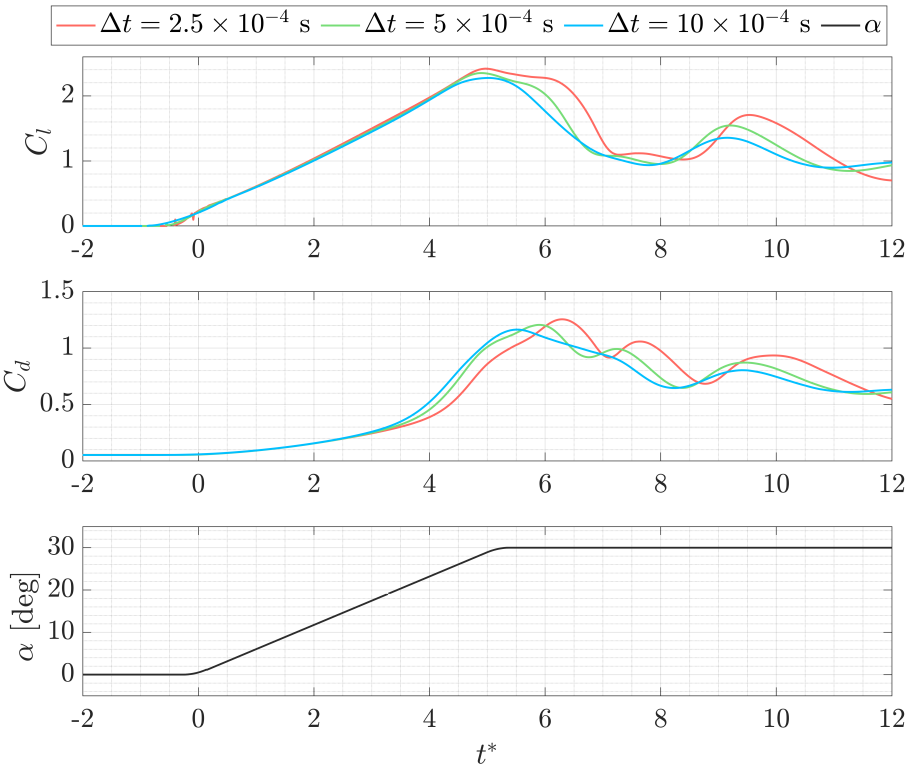

Figure 3.25: Time-step independence verification for baseline airfoil with maximum amplitude of α_1=30° and k=0.05.

As depicted in Figure 3.25, the response and evolution of the aerodynamic forces over time exhibited a consistent pattern regardless of the chosen time-step. However, it was observed that the solution was dependent on the time-step employed. Decreasing the time-step resulted in a time delay and an amplification in the magnitude of the lift overshoot. To further elucidate this phenomenon, Figure 3.26 illustrates the impact of the time-step on the strength, morphology, and convective behavior of the DSV at $t^* = 6.5$. Analysis of these frames reveals that the DSV becomes stronger and more cohesive as the time-step size decreases. Furthermore, larger time-steps lead to earlier detachment of the DSV from the leading-edge vorticity source as well as enhanced downstream convection, shedding light on the rationale behind the delayed and intensified lift overshoot observed with the smaller the time-step.

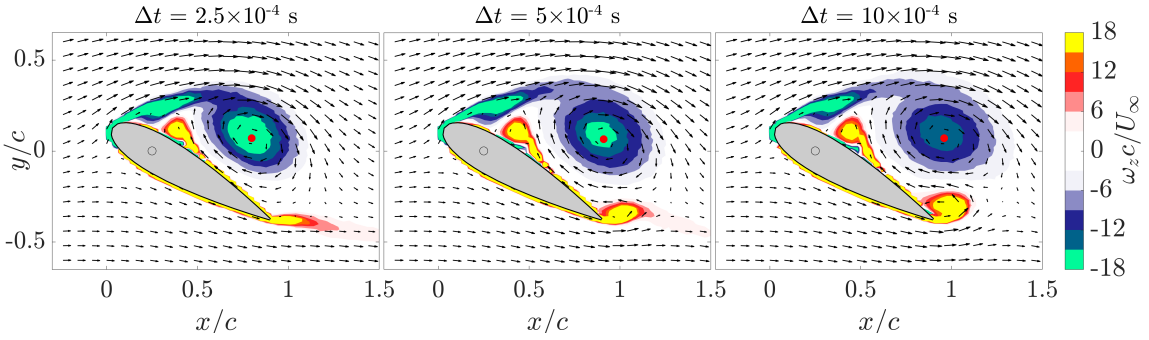

Figure 3.26: Vorticity field ω_z at t^*=6.5 illustrating the dependence of DSV strength, shape and convective path on time-step. The red dots indicate the DSV position determined with Γ_1 method.

Validation case: baseline airfoil

Ideally, the dynamic solution should be independent of the time-step selection. However, this was not achieved in this study as shown in Figure 3.25. When comparing the CFD results to the experimental data, it was observed that there was an optimal time-step for which the predicted solution successfully matched the DSV convection path obtained from experimental data. In line with these findings, an alternative approach was followed. Using the Γ_1 method that will be presented in Section 3.3.1, the DSV strength and convective path were monitored in time and space from the CFD data computed with three different time-steps Δt=2.5×10^{-4} s, 5×10^{-4} s, and 10×10^{-4} s. The experimental data was averaged in the span direction to obtain the average DSV representation across the airfoil span.

Figure 3.27 illustrates the convective path in airfoil coordinates and circulation of the DSV obtained using the experimental data from $t^* = 5.5$, corresponding to the time when the airfoil had just reached its maximum angle of attack of $\alpha = 30°$, until $t^* = 7.3$, after which the DSV convected downstream and had almost dissipated. Ideally, tracking the formation and growth of the DSV as the airfoil pitches up would be desirable. However, the resolution of the binned PTV data was insufficient to allow for this. Therefore, only the time span during which the DSV could be accurately tracked is presented. Figure 3.27 also includes the DSV core position and circulation at discrete time instants, obtained from the CFD flowfield calculated with varying time-steps. It is important to highlight that the temporal resolution of the CFD data was lower because, for these simulations performed for validation purposes, the flowfield was saved every Δt^*=0.5 equivalent to Δt=0.01 seconds.

In terms of convective path, Δt=5×10^{-4} s yields the optimal agreement between CFD simulations and experimental data. However, it is observed that the circulation appears notably lower in the experimental results. This discrepancy arises from the spanwise averaging of STB-PTV data. Due to the varying positions of the DSV along the span, the core vorticity experiences a slight attenuation post-averaging. This phenomenon is clarified in Figure 3.28, where the instantaneous vorticity field from experimental data (Figure 3.28a), CFD predictions (Figure 3.28b), and the spanwise-averaged experimental vorticity field (Figure 3.28c) are depicted. A comparison of the instantaneous flowfield slices indicates that the DSV predicted by the CFD exhibits comparable strength to that observed in the experimental scenario, whereas the averaged vorticity field shows a notably weaker core. Consequently, a time step of Δt=5×10^{-4} s was utilized during the dynamic simulations presented in this work, as it has been found to produce the most favorable agreement between CFD simulations and experimental data.

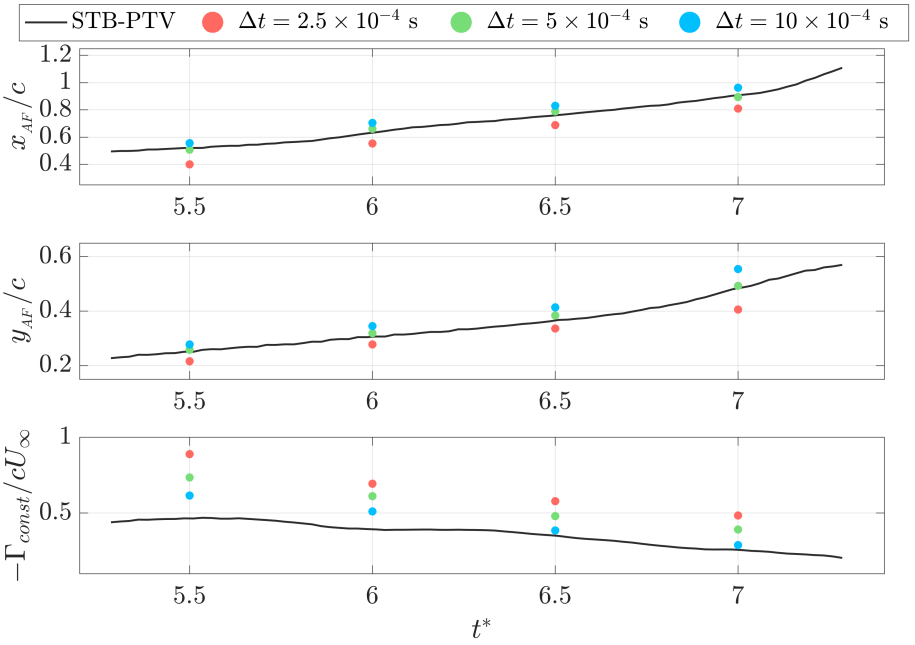

Figure 3.27: DSV convection and circulation validation for baseline airfoil with k=0.05 and α_1=30°.

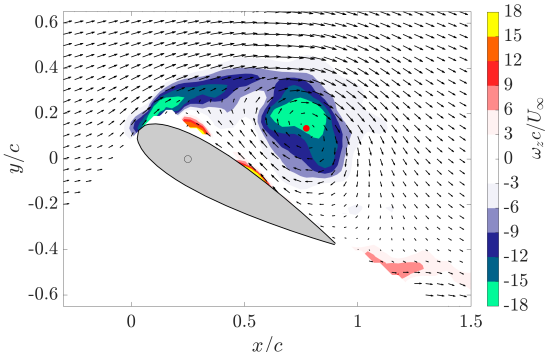

(a) Instantaneous vorticity field for the baseline airfoil at z/c=0 obtained from experimental data.

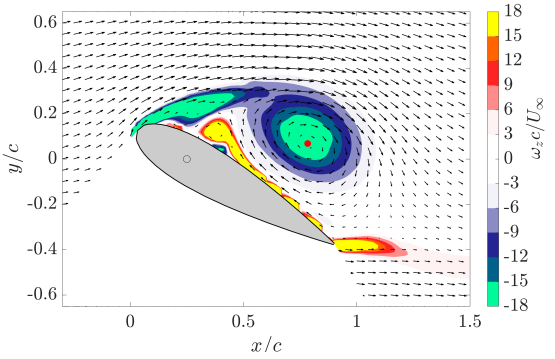

(b) CFD instantaneous vorticity field for the baseline airfoil at z/c=0 calculated with Δt=5×10^{-4} s.

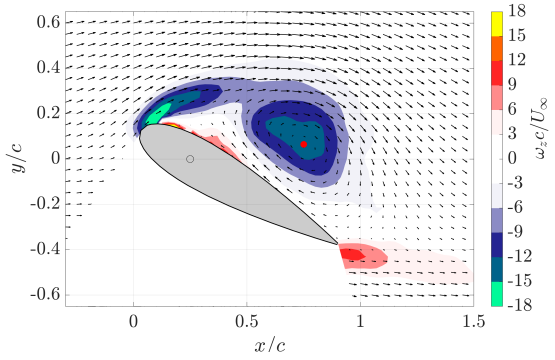

(c) Spanwise average of the vorticity field for the baseline airfoil obtained from experimental data.

Figure 3.28: Comparison of the experimental and CFD vorticity fields at $t^* = 6$. The red dots indicate the DSV core position determined with Γ_1 method.

3.3. Post-processing tools

This section introduces the two main post-processing tools used in the analysis of CFD and experimental data. First, an efficient approach for tracking the DSV in both CFD and experimental flowfields, which has been extensively used throughout this work, is detailed in Section 3.3.1. Secondly, the phase-averaging approach and a discussion on its suitability for application in the current experiments are presented in Section 3.3.2.

3.3.1. Dynamic stall vortex tracking

Understanding the shedding and convection of the DSV is paramount for effectively managing the fluctuating aerodynamic loads experienced by airfoils operating under dynamic conditions. To capture these vortical structure, particle tracking velocimetry serves as a valuable tool, offering insight into the temporal evolution of the flowfield. However, for a comprehensive comparison between smooth leading-edge and tubercled airfoils, solely relying on PTV may not suffice to draw accurate conclusions regarding the impact of tubercles on the DSV. This limitation arises due to the difficulty in identifying the impact of tubercles on the position or strength of the DSV, which may not be immediately apparent to the naked eye. Even when differences are significant, comprehending the temporal evolution of the DSV and comparing it across different airfoils requires more than flowfield snapshots. Given that PTV provides a time-resolved perspective of the DSV evolution, automated routines are essential for characterizing the DSV accurately; otherwise, data analysis becomes cumbersome and excessively time-consuming.

To address this issue and efficiently quantify the impact of tubercles on the DSV and dynamic stall phenomenon, a robust method for identifying and tracking the DSV vortical structure was necessary. Traditional vortex identification methods such as the Q-criterion struggle to characterize vortical structures due to the intense shear between the free stream and the recirculation region, as highlighted by Taylor and Amitay (2016). Instead, they suggested the Normalized Angular Momentum (NAM) criterion, denoted as Γ_1, first introduced by Michard et al. (1997). In this research this approach was adopted since this vortex identification method has previously been successfully applied to track the DSV captured with Particle Image Velocimetry (PIV) [Taylor and Amitay 2016] and Molecular Tagging Velocimetry (MTV) [Hrynuk and Bohl 2020].

The center of the DSV was identified using the Γ_1 method, as described in Equation 3.4. Here, N denotes the size of the interrogation window, r represents the distance to the location being evaluated for this element of the summation, and $u(M_i)$ represents the velocity vector.

$$\Gamma_1 = \frac{1}{(2N+1)^3} \sum_i \frac{r_i \times u(M_i)}{|r_i|\,|u(M_i)|} \tag{3.4}$$

Equation 3.4 was implemented on a discrete grid perpendicular to the span direction, isolating an N by N planar region within the domain, as illustrated in Figure 3.29a. Emphasize that grid points located within the airfoil section or outside the PTV domain were excluded from the summation.

During the implementation phase, it was observed that the Γ_1 method exhibited slight bias when the vortex was not precisely centered within the grid. To address this issue, an iterative approach was adopted: initially, Equation 3.4 is solved using the initial grid depicted in Figure 3.29a which has a grid spacing of 3 mm. Subsequently, the DSV core position is estimated to be at the grid point with the highest Γ_1 value, although this positioning may not be entirely accurate as the actual core could lie between two adjacent grid points. A new mesh is then defined, with a grid spacing of 1mm, centered at the updated vortex core position. Moreover, the grid width and height are reduced to 20 mm to exclude points near the airfoil where data might not be available. The process of solving Equation 3.4 with this refined mesh identifies a new vortex core. This iterative procedure continues until the new core position deviates by no more than 0.5 mm betweem two consecutive iteration.

In Figure 3.29b, it can be seen that thanks to this iterative approach, the core position is adjusted by approximately 10 mm. Furthermore, it is evident that at the final iteration, the core is accurately positioned at the center of rotation of the DSV, as illustrated by the velocity vectors.

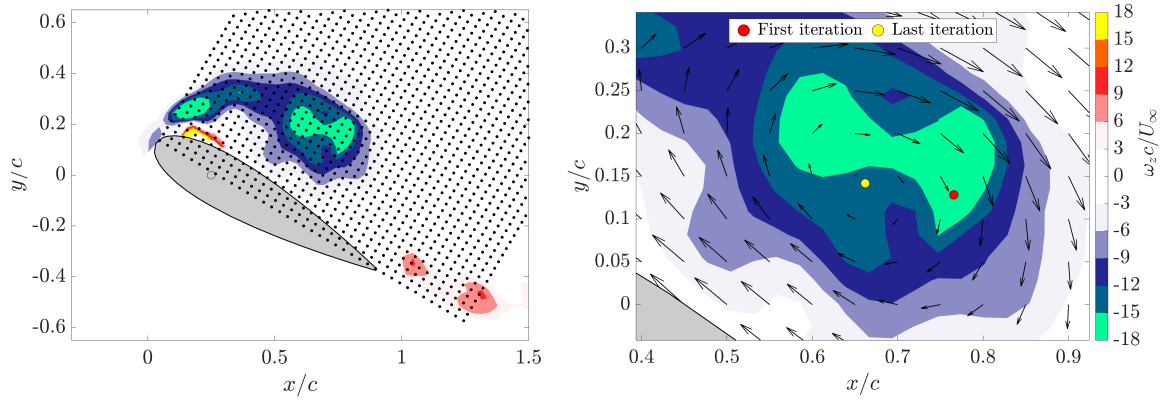

(a) Mesh used for the first iteration with 3 mm resolution.

(b) Evolution of the vortex core position calculated with Γ_1.

Figure 3.29: Grid and identified vortex core position using Γ_1 method with iterative approach.

This methodology was extended to a three-dimensional context. Although determining the vortex core position relied solely on 2D slices perpendicular to the airfoil's span direction, the three-dimensional evolution of the DSV over the airfoil at a given time instant was determined by locating several planes along the span of the airfoil.

Once the core of the DSV was located in space, determining its circulation became feasible. To ensure comparability with the findings of Hrynuk and Bohl (2020), the circulation was estimated using the same methodology. Consequently, the circulation results presented in this study solely reflect the circulation of the DSV, computed as the summation of the DSV vorticity within its core radius. Establishing the core radius poses challenges as it requires to first identify the outer edge of the vortex. To accomplish this, the radius of the DSV was determined using the radius of gyration defined by Equation 3.5 [Bohl and Koochesfahani 2009], where ω_z represents the vorticity field aligned with the span direction, and r denotes the distance from the DSV core to the point being evaluated. Subsequently, the circulation was calculated by integrating the vorticity over an area equivalent to $1.75r_{core}$.

$$r_{core} = \sqrt{\frac{\iint r^2 \langle \omega_z \rangle \, \mathrm{d}A}{\iint \langle \omega_z \rangle \, \mathrm{d}A}}. \tag{3.5}$$

The computation of circulation during the DSV analysis is influenced by the core radius which changes over time, therefore introducing uncertainty into the estimations. While this is manageable for single-frame cases given that the estimated radius can be visually verified, analyzing multiple frames across various span positions and cycles makes individual radius verification impractical. Consequently, a constant radius r_{const}=10 mm was also utilized to calculate the DSV circulation, ensuring consistency across analyses. This approach yielded to a second circulation value calculated with an area of integration which was independent of the DSV core radius estimate. Furthermore, this constant radius was significantly smaller than the actual DSV radius providing reliable insights into DSV core inner vorticity and DSV diffusivity.

3.3.2. Phase-averaging

Phase averaging is a fundamental technique in experimental aerodynamics that serves to simplify complex flowfield data by focusing solely on repetitive patterns. This technique involves averaging data over multiple flow cycles, thereby providing a clearer understanding of the underlying flow behavior while filtering out transient fluctuations. By emphasizing coherent flow features and attenuating random noise, phase averaging facilitates the identification and analysis of relevant flow structures. On the other hand, it has to be acknowledged that flow structures lacking repetition across cycles are

inherently reduced or may even disappear from the averaged flowfield. Hence, one should be careful when employing phase averaging on experimental data, especially if specific flow characteristics are not repeatable between phases.

During the experiments conducted in the present work, the actuator was connected to an encoder as described in Section 3.1.1. The encoder readings were sent to a LabView program which triggered the measurement once the airfoil crossed an angle of attack of α=0.5°. Ensuring that the cameras were triggered at the same phase of motion for every cycle led to phase-locked measurements. Thus, the way the experiments were conducted resulted in data that could be easily phase-averaged without prior data treatment.

Hrynuk and Bohl (2020) utilized phase-averaging to enhance the temporal resolution of their measurements, acquired from experiments involving smooth leading-edge and tubercled airfoils undergoing a similar pitch-up and hold motion to that employed in this study. They noted the repeatability of the flowfield across runs was sufficient to average each phase without compromising any relevant flow feature. Consequently, this methodology was also applied to the experimental data gathered in this research.

To demonstrate the repeatability of the DSV, Figures 3.30 and 3.31 present three instantaneous and the corresponding phase-averaged vorticity iso-surfaces at $\omega_z c/U_\infty$=-9 for t^*=6 and t^*=7 respectively. The black lines denote the DSV core position determined using the Γ_1 method, as described in Section 3.3.1. At t^*=6, the three cycles present a similar DSV in terms of position and strength. Although, the DSV core position slightly differs from cycle to cycle, it is save to assume that no information is lost during the phase-averaging process. The DSV phase-averaged over 10 cycles is just a smoother representation of the three cases and its core position is also more uniform across the span. Highlight the fact that because the position of DSV slightly differs between cycles, the application of phase-averaging leads to a subtle reduction in the strength of the DSV. This occurs as small flow structures characterized by high vorticity are attenuated during the averaging process.

Conversely, at t^*=7, when the DSV has been convected downstream past the trailing-edge and it is already starting to dissipate, the variation between cycles is significantly higher. The previously organized vortex structure breaks down, leading to a transition to a more turbulent flow regime. It is worth noting that the dissipation pattern of the vortex differs across cycles. For instance, the initial cycle exhibits a DSV discontinuity at $z/c > 0$, a feature not observed in subsequent cycles. Consequently, this discontinuity is reflected in the phase-averaged flowfield. The discrepancy is a result of the limited number of cycles available for phase averaging, allowing outlier flow features which are potentially unrepresentative of the mean flow, to influence the phase-averaged flowfield. Employing a greater number of cycles during the averaging process would likely mitigate the DSV discontinuity. This case underscores the importance of meticulously evaluating and comparing instantaneous with phase-averaged results before drawing any conclusions.

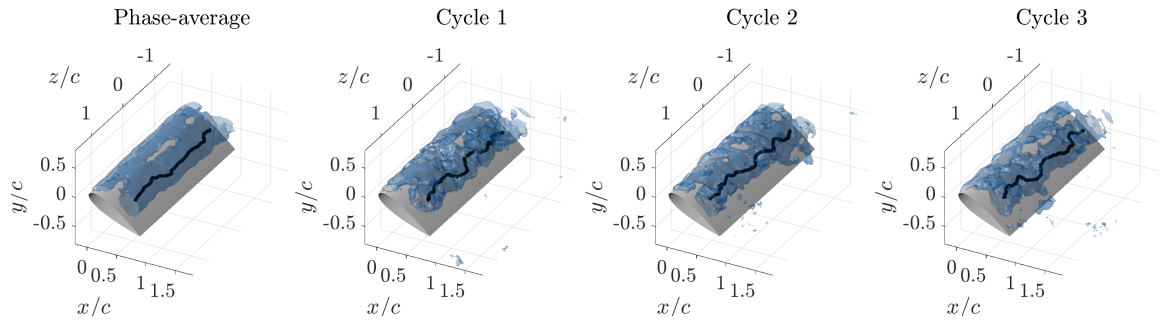

Figure 3.30: Vorticity iso-surface at $\omega_z c/U_\infty$=-9 showcasing the DSV at t^*=6 for the phase-averaged case and 3 consecutive cycles.

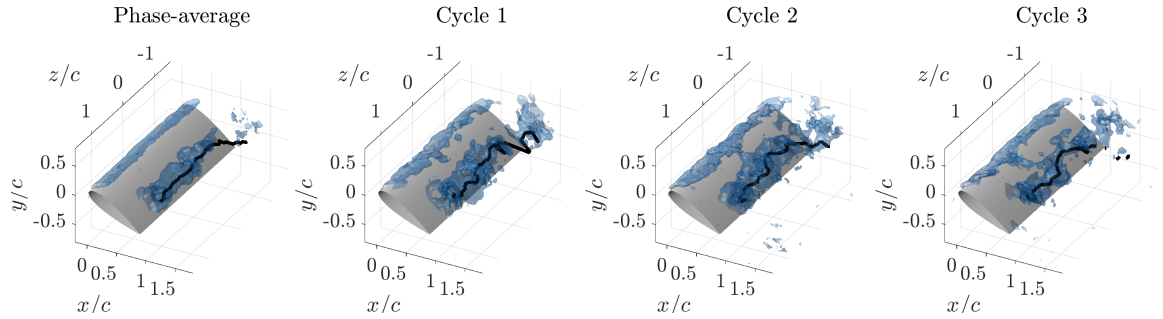

Figure 3.31: Vorticity iso-surface at $\omega_z c/U_\infty$=-9 showcasing the DSV at t^*=7 for the phase-averaged case and 3 consecutive cycles.

In the case of tubercled airfoils, relying solely on phase-averaged flowfield analysis may lead to erroneous interpretations. As will be detailed in Section 4.4.1, stall cells form at varying trough positions in each cycle. Consequently, phase-averaging the flowfield results in the stall cells disappearing from the domain, presenting the airfoil with uniform separation across the span, as depicted in Figure 3.32. This scenario illustrates a clear example of when the phase-averaging method is unsuitable for analysis.

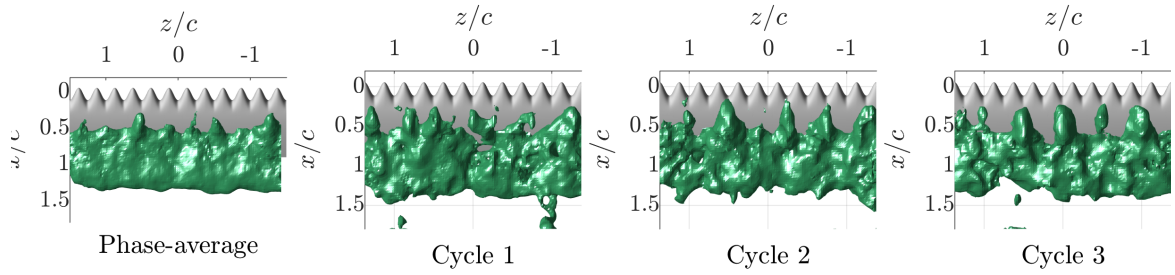

Figure 3.32: A10L25 airfoil separated region indicated with iso-surface at U_x=0 m/s for the phase-averaged case and 3 consecutive cycles at $t^* = 9$.

In the results discussion provided in Chapter 4, the instantaneous flowfield is initially employed to obtain a precise understanding of the flowfield and its evolution during the pitch-up and hold motion. Subsequently, phase-averaged data is utilized when a comprehensive and neater understanding of the DSV position and strength is required. Moreover, it is applied exclusively to phases preceding DSV break down and dissipation, where the repeatability between cycles has proved to be high enough.

4

Results

This chapter presents the results from both experimental and computational studies conducted in this thesis to assess how tubercles affect the formation and convection of the dynamic stall vortex (DSV), as well as the separation development in deep stall conditions, which are crucial aspects of the dynamic stall process. The experimental investigations detailed in Section 4.1 provide insights into the flow dynamics around baseline and tubercled airfoils, including phase-averaged and amplitude effect studies. A complementary analysis of the computational fluid dynamics (CFD) results in Section 4.2 expands on these findings, enhancing the understanding of this unsteady aerodynamics phenomenon and highlighting the similarity in results obtained with both methodologies. Section 4.3 delves into the dynamics of the DSV, quantitatively examining the impact of the tubercles on its convection and circulation. Section 4.4 explores the complex flow behaviors in the deep stall regime after the DSV has been convected past the trailing edge, including stall compartmentalization and wake instabilities. The evaluation of aerodynamic forces, presented in Section 4.5, concludes with insights drawn from the flowfield analysis and DSV tracking, summarizing their effect on the unsteady aerodynamic forces obtained from CFD. Finally, Section 4.6 assesses tubercle performance across different pitching-up conditions, verifying whether the conclusions from the previous sections hold true under a wider range of operational conditions.

4.1. Experimental flowfield characterization

This section details the experimental results obtained using particle tracking velocimetry. All the data shown pertains to the motion with k=0.05 and a maximum angle of attack of α_1=30°, unless otherwise specified. The temporal evolution of the angle of attack for this specific motion is depicted in Figure 3.4. This particular motion was selected as it represents the lowest reduced frequency tested during the experimental campaign, making it the best in terms of temporal resolution, which is crucial for analyzing the dynamic stall phenomenon. Additionally, the slower motion of the airfoil allowed more time for the particles to be fed into the DSV, facilitating a more detailed flowfield reconstruction within its core. Choosing the smallest amplitude angle α_1 also helped in this regard.

Regarding the data visualization, for all the plots the data origin is configured such that the pitching axis is located at x/c=0.25. The x axis is aligned with the free-stream direction while the z axis is aligned with the span direction. The experimental data presented in this section has been selectively masked to exclude particles located behind the wing where camera visibility was obstructed. Although these particles were detected by the STB-PTV algorithm, they are considered ghost particles that do not accurately represent the actual flowfield. Consequently, rather than removing the ghost particle tracks from the flowfield, a simpler approach is used and data from the bins behind the airfoil are omitted, simplifying the flowfield analysis and enhancing the clarity of visualizations.

Throughout this study, iso-surfaces have been extensively utilized to represent various variables within three-dimensional space. For clarity and ease of understanding, consistent colors have been applied: red and blue denote positive and negative spanwise vorticity ω_z, respectively, while green highlights the U_x=0 m/s velocity iso-surfaces, marking regions of flow separation. Additionally, when presenting results from DSV tracking or when an analysis necessitates identifying a specific flow feature relative to the airfoil, the airfoil frame of reference is employed, and the coordinates are specifically denoted as x_{AF} and y_{AF}. Recall that the origin is positioned at the leading-edge of the baseline airfoil.

4.1.1. Baseline airfoil

Results for the smooth leading-edge airfoil are illustrated in Figure 4.1, where the vorticity iso-surfaces at $\omega_z c/U_\infty$=-9 display the position and shape of the DSV. The three-dimensional vorticity visualization successfully captures the temporal evolution of the DSV. Noticeably uniform along the entire airfoil span during almost the entire motion, the DSV shows spanwise variability in its initial formation stages around t^*=4, when the boundary layer begins to roll up. This variability is likely due to the limited reconstruction quality of the PTV method in the near-wall region, which reduces its ability to accurately capture the initial stages of DSV formation. Moreover, at the end of the convection phase approximately at t^*=6.5, the DSV begins to dissipate, a process that is noticeably non-uniform along the span direction. This non-uniformity is likely due to the inherent randomness associated with turbulence dissipation, which can cause variations in how the vortex breaks down across the airfoil.

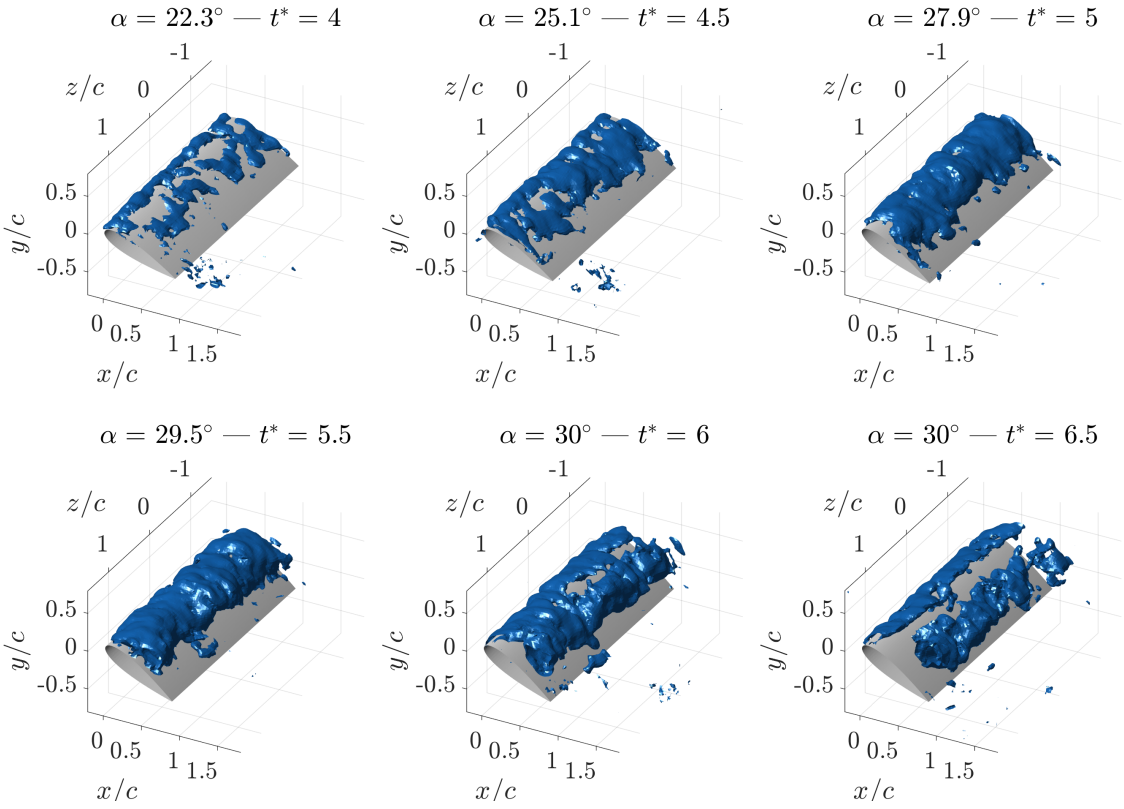

Figure 4.1: Vorticity iso-surface at $\omega_z c/U_\infty$=-9 for baseline airfoil.

Given the spanwise uniformity of the DSV during its growth and convection phases, the flowfield can be effectively analyzed using 2D slices to enhance understanding of the DSV evolution, as demonstrated by Hrynuk and Bohl (2020). Accordingly, Figure 4.2 depicts the time evolution of the spanwise vorticity field ω_z at the span location of z/c=0. The flowfield observations align with findings from previous studies, including those by Gendrich (1999), Choudhry et al. (2014a), and Hrynuk and Bohl (2020), among others.

The vector map displaying the velocity field indicates that the flow remains attached past the static stall angle of attach, which, as discussed in Section 3.2.1, is approximately α_{ss}=15° for the baseline airfoil. Particularly at t^*=4 and α=22°, it is evident that despite the boundary layer beginning to roll up and concentrate near the leading-edge, the majority of the flow is still attached to the airfoil's surface.

As the airfoil pitches up, the DSV grows in size and strength. Below the DSV, a secondary vortex with opposite vorticity forms due to the proximity of the airfoil's surface. As suggested by Hrynuk and Bohl (2020), this secondary vorticity structure causes the DSV to move upward and pinch off. Due to limited flowfield reconstruction near the airfoil surface, this second vorticity structure is less visible, though it can still be detected. By t^*=5.5, the DSV reaches the mid-chord position and approximately at t^*=6, it detaches from the leading-edge vorticity source marking the beginning of the convection phase. At this stage, the DSV is a distinct vortical structure that is convected over the suction of the airfoil. As it moves downstream and gradually dissipates, it grows in size eventually braking down. This DSV evolution is consistent with previous research in dynamic stall with smooth leading-edge airfoils [Jumper et al. 1987; Gendrich 1999].

During the pitch-up phase, a vortex with positive circulation also forms at the trailing-edge due to the flow rolling over from the pressure side. As will be observed with the tubercled airfoil, the intensity of this trailing-edge vortex is closely linked to the strength of the DSV.

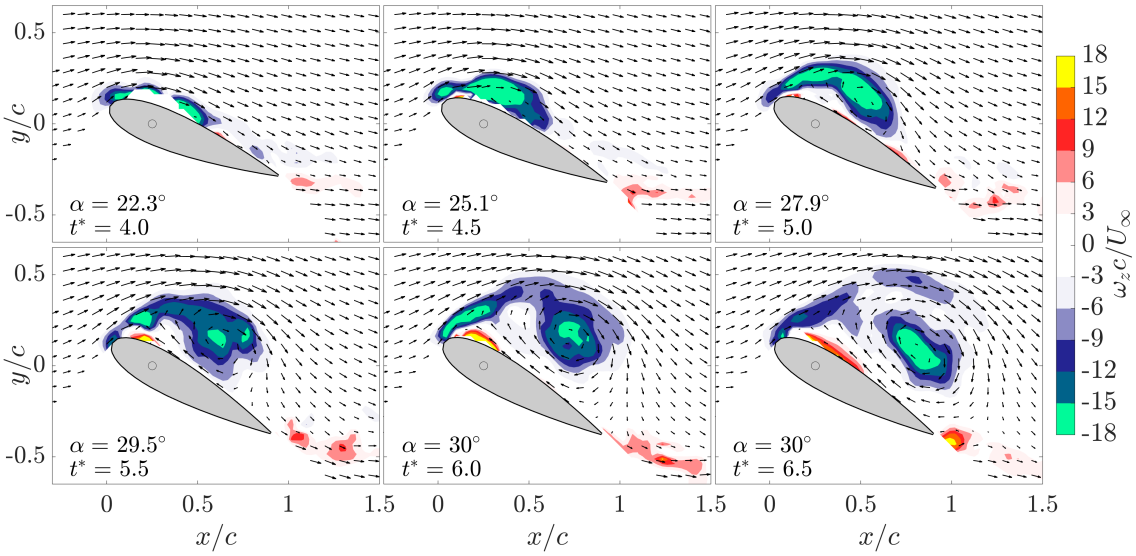

Figure 4.2: 2D vorticity flowfield for baseline airfoil at z/c=0.

4.1.2. Tubercled airfoil

The three-dimensional characteristics of the DSV for the A10L25 airfoil are depicted using vorticity iso-surfaces at $\omega_z c/U_\infty$=-9, as shown in Figure 4.3. Although the A05L25 airfoil was also tested, the largest amplitude was selected to clearly highlight the differences compared to the baseline airfoil. A detailed justification for this choice is provided in Section 4.1.4.

The presence of tubercles significantly alters the formation and convection of the DSV. A key difference is that the leading-edge vorticity is discretized along the span, with vorticity being only shed from the troughs. Even at the early stage of t^*=4.5, the vorticity at the trough locations is already visible. The DSV structure does not become clearly visible until t^*=5.5, and its position is almost at the trailing-edge, significantly further downstream than in the baseline case. From the 3D flowfield visualization, it is evident that the DSV appears less coherent and weaker than that of the smooth leading-edge airfoil.

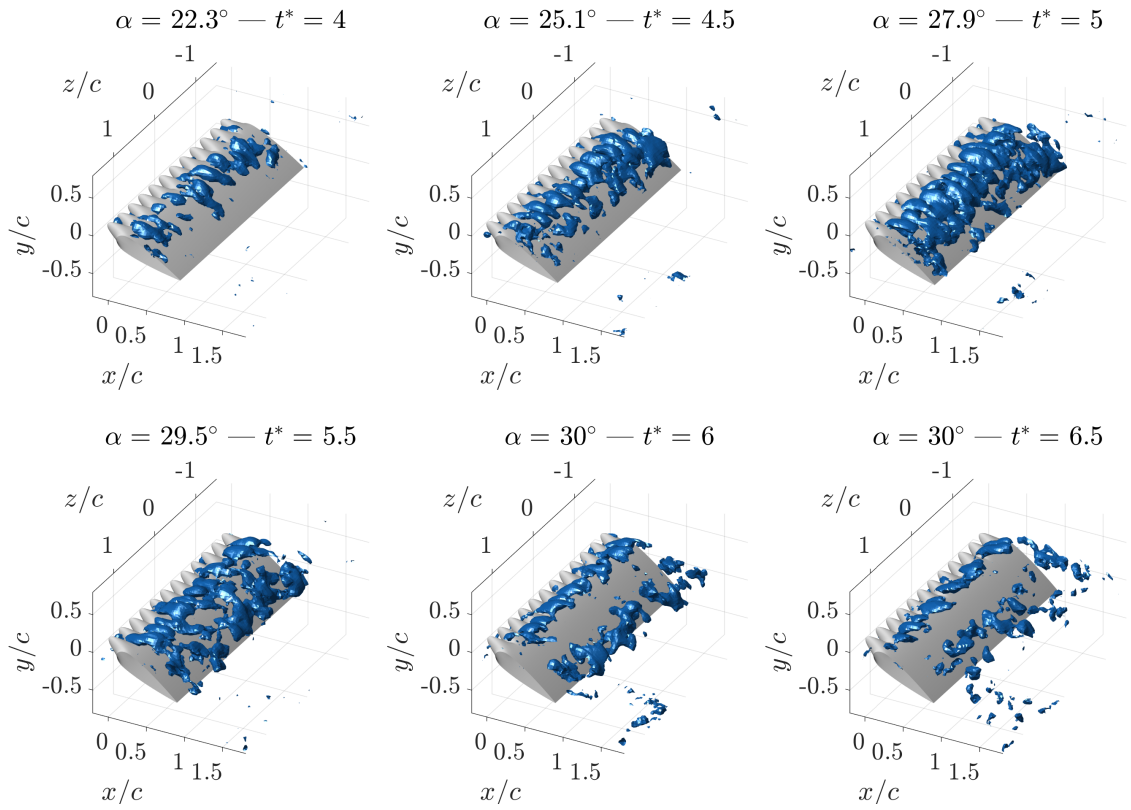

Figure 4.3: Vorticity iso-surface at $\omega_z c/U_\infty$=-9 for A10L25 airfoil.

While the flowfield exhibits less uniformity in the span direction compared to the baseline airfoil, a consistent flowfield evolution is observed at all the peaks, contrasting with the behavior at the troughs. This difference between the peaks and troughs was previously identified by Hrynuk and Bohl (2020). To further elucidate this peak-trough flow pattern, Figure 4.4 displays the vorticity field at a plane aligned with a trough at z/c=0, and Figure 4.5 illustrates the vorticity field at the peak located at the span location of z/c=0.125. It is important to note that although only two planes are shown here, the flow characteristics discussed are representative of all other peaks and troughs of the airfoil.

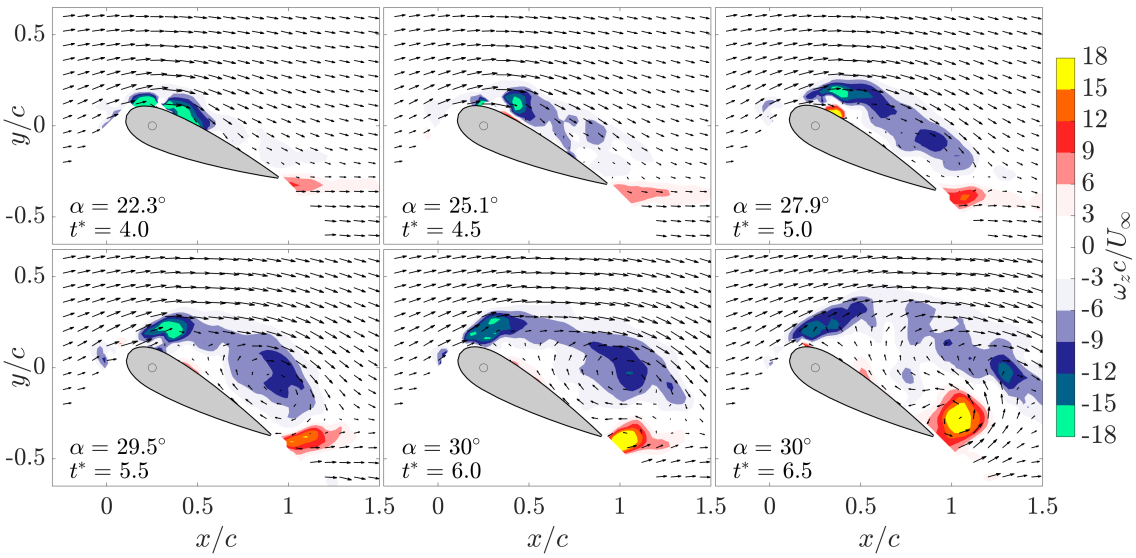

Figure 4.4: 2D vorticity flowfield for A10L25 airfoil at trough location z/c=0.

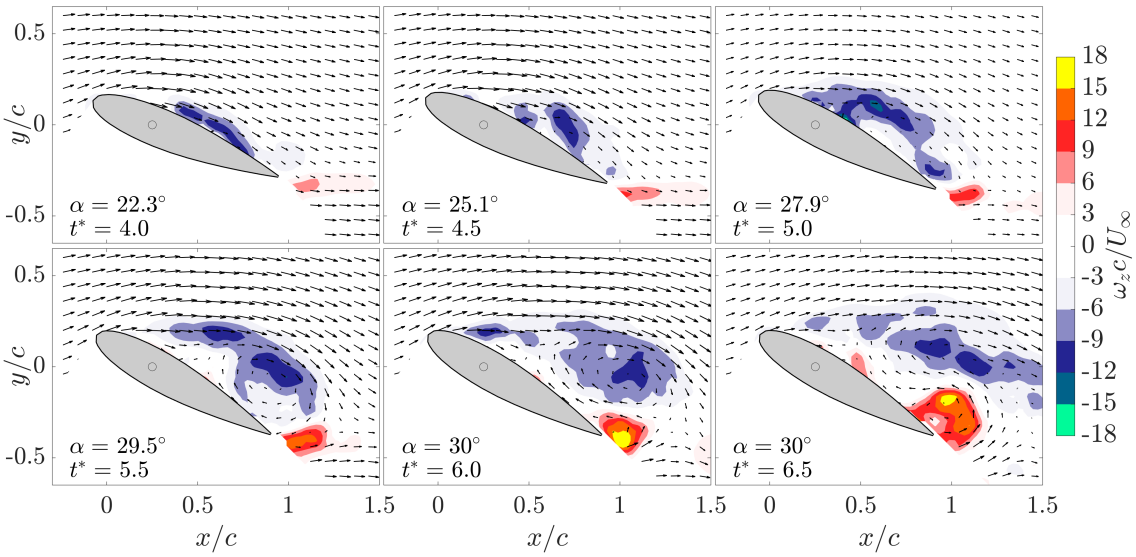

Figure 4.5: 2D vorticity flowfield for A10L25 airfoil at peak location z/c=0.125.

Significant differences are evident in the trough plane when comparing to the baseline. Initially, by t^*=4, the boundary layer vorticity starts to concentrate at the leading-edge similarly to the baseline. However, by t^*=4.5, a reverse flow region appears at the trailing-edge and extends rapidly upstream separating the DSV from the airfoil and therefore impeding its growth. This trailing-edge separation is caused by the upwash effect created by the streamwise counter-rotating vortex pairs along the troughs. The early interruption of the formation phase results in a weaker DSV which does not become visible until t^*=5, significantly later than in the baseline scenario. As already indicated by the 3D iso-surfaces, the position of the DSV is further downstream, and its core exhibits lower vorticity levels than in the baseline case. By t^*=6, after the airfoil has reached its maximum angle of attack, the DSV has nearly convected past the trailing-edge and it is completely dissipated after t^*=6.5. Similar to observations with the smooth leading-edge airfoil, the flow on the pressure side rolls up over the trailing-edge, forming a vortex with a rotation direction opposite to that of the DSV. Due to the weaker DSV, the downwash on the trailing-edge is reduced, thereby facilitating the formation of a stronger trailing-edge vortex. As it will proved with the CFD results in Section 4.5, this trailing-edge vortex has minimal effect on the airfoil total lift.

The peak plane also exhibits notable differences compared to the baseline and the A10L25 trough plane. By t^*=4, while the baseline and trough sections are already displaying signs of boundary layer roll-up at the leading-edge, the peak remains completely attached, with a distinct region of compact vorticity only becoming visible past $x_{AF}/c \approx 0.4$. As the angle of attack increases, reverse flow begins to manifest at the trailing-edge, and by t^*=5.5, the DSV becomes clearly visible. It's position is similar to the trough case.

The downstream shift in DSV formation is directly linked to the counter-rotating streamwise vortices shed by the tubercles. Figure 4.6 displays streamwise vorticity iso-surfaces at $\omega_x c/U_\infty$=-1 and 1, illustrating the counter-rotating vortices at the time instant of t^*=4.5. The velocity flowfield used for calculating the vorticity is phase-averaged, which explains the vorticity discontinuity observed past $x_{AF}/c \approx 0.5$, where reverse flow starts and phase repeatability significantly decreases. From this figure, it is evident that the counter-rotating vortices coexist with the DSV, influencing its formation and dynamics. Similarly to static scenarios, downwash at the peak span locations enhances flow attachment, while upwash is induced along the troughs, yielding the opposite outcome. Consequently, the DSV growth phase is interrupted at the troughs due to the earlier trailing-edge separation caused by the upwash which promptly extends upstream and detaches the DSV from the airfoil's surface, preventing it from growing and increasing its strength. At the peaks, the downwash prevents the boundary-layer roll-up and subsequent concentration of vorticity near the leading-edge. Hence, the DSV formation only begins once separation occurs at the trailing-edge, resulting in a DSV that is weaker and forms further downstream compared to the baseline.

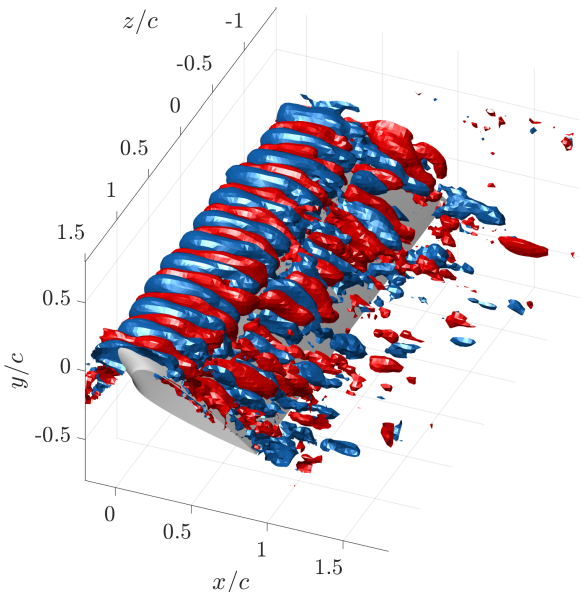

Figure 4.6: Streamwise vorticity iso-surface at $\omega_x c/U_\infty$=-1 (blue) and 1 (red) for A10L25 airfoil at t^*=4.5.

The diminished strength of the DSV in tubercled airfoils can also be attributed to differences in the shedding direction of the leading-edge vorticity. The tubercles shed streamwise vorticity at the expense of reduced spanwise vorticity. Conversely, the straight leading-edge of the baseline airfoil primarily sheds vorticity in the spanwise direction, which aligns with the rotational axis of the DSV. Consequently, a stronger DSV can be expected for the baseline airfoil. Even if the streamwise vortices are eventually tilted and merge into the DSV, this integration process is likely to be less efficient than in scenarios where the leading-edge vorticity is initially aligned with the DSV rotational axis.

4.1.3. Phase-averaged flowfield

To further clarify the three-dimensional formation and convection of the DSV and assess the impact of tubercles, vorticity iso-surfaces at $\omega_z c/U_\infty$=-7 are used. These surfaces are derived from phase-averaging over 10 cycles. They are presented for the smooth leading-edge airfoil in Figure 4.7, and for the tubercled airfoil A10L25 in Figure 4.8. While these figures do not show the actual instantaneous flowfield but rather an average over 10 cycles, they enhance the interpretation and analysis of the DSV. As mentioned in Section 3.3.2, due to variations in the exact position, strength, and shape of the DSV across different phases and cycles, the phase-averaging technique tends to reduce the vortex strength and make it more diffuse. Nonetheless, prior to the breakdown and diffusion of the DSV, the phase-average provides a reliable representation of the DSV dynamics and is therefore valuable for analyzing the flowfield.

For the tubercled airfoil, which exhibits decreased repeatability, both the instantaneous and phase-averaged iso-surfaces, as shown in Figures 4.3 and 4.8 respectively, demonstrate similar DSV dynamics. However, phase-averaging enhances the coherence and spanwise uniformity of the DSV. As a result, the discretization of leading-edge vorticity is better defined throughout the entire pitching-up phase.

Comparing the baseline and the tubercled airfoil also reveals that the DSV is formed further downstream in the case of the tubercled airfoil as already identified with the instantaneous flowfield. Regarding size, the DSV for the tubercled airfoil at both t^*=6 and that of the baseline at t^*=6.5 appear to be of similar size. However, the vorticity levels within the vortex core are higher in the baseline case, as observed in the 2D instantaneous slices and as will be further validated with CFD results in Section 4.2. These conclusions have been already drawn from the instantaneous flowfield, but are further reinforced by the phase-averaged vorticity, which makes the observations even more apparent. Additionally, the consistency between the phase-averaged and instantaneous flowfields suggests that the insights derived from the instantaneous observations reflect flow features that are representative across all the cycles measured during the experiments.

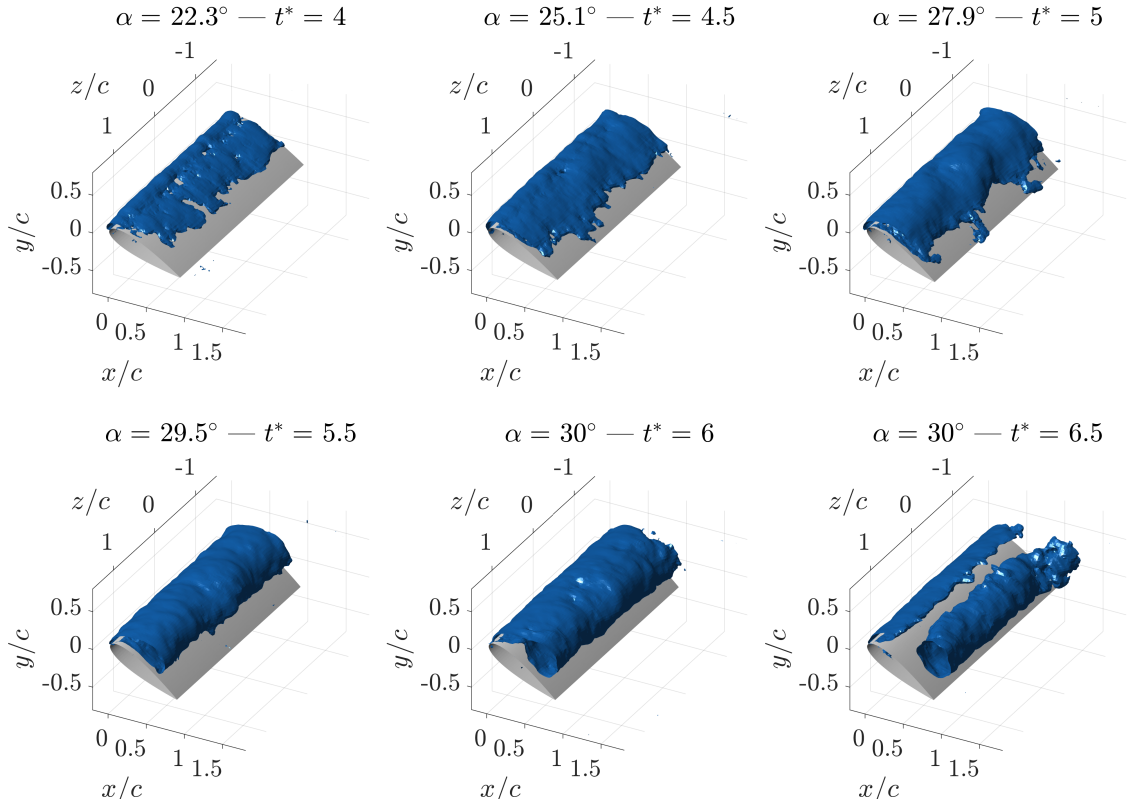

Figure 4.7: Phase-averaged vorticity iso-surfaces at $\omega_z c/U_\infty$=-7 for the baseline airfoil.

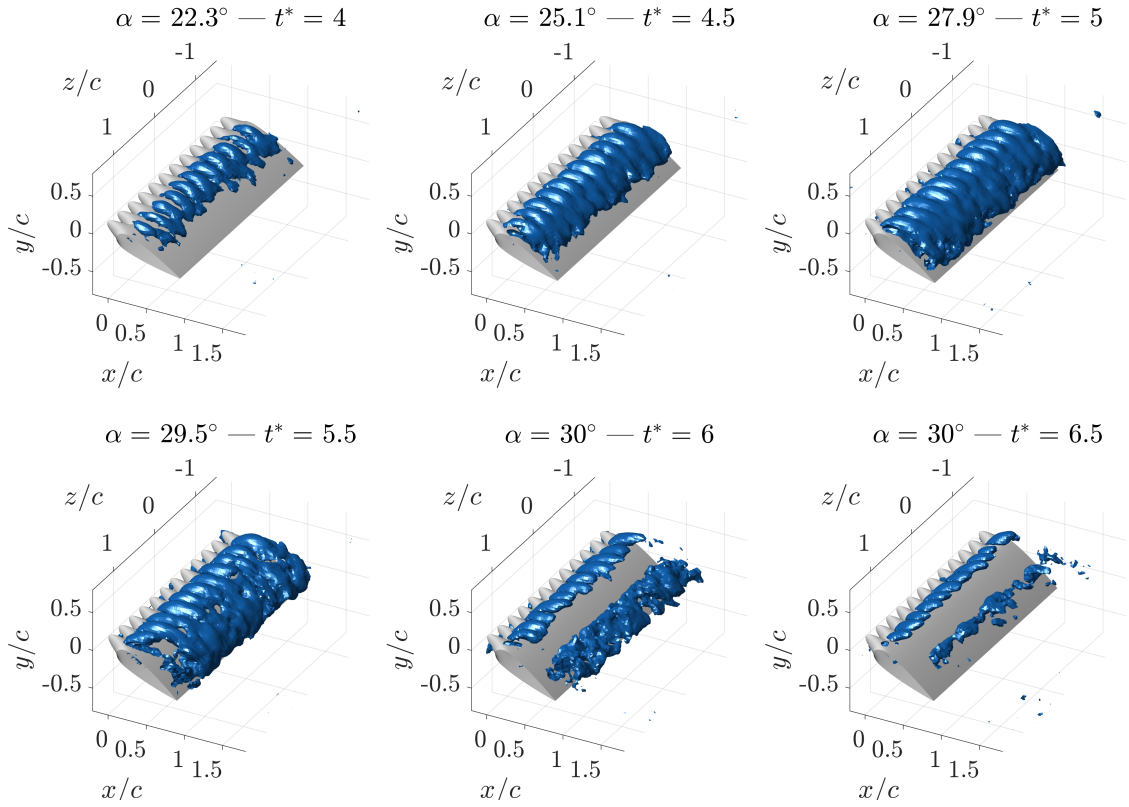

Figure 4.8: Phase-averaged vorticity iso-surfaces at $\omega_z c/U_\infty$=-7 for the A10L25 airfoil.

4.1.4. Tubercle amplitude effect

This section has presented results primarily for the baseline and the A10L25 airfoil, intentionally focusing on the maximum tubercle amplitude to clearly demonstrate their impact on the flowfield. This approach facilitates a detailed analysis of how tubercles influence the dynamic behavior of the airfoil, especially in terms of the development and evolution of the DSV. By emphasizing the effects at a significant tubercle amplitude, the study ensures that the changes induced by the tubercles are both observable and quantifiable. This addresses one of the main limitations of the experiment conducted by Hrynuk and Bohl (2020), where an amplitude of A/c=0.05 was chosen, and the flow field differences between the tubercled and smooth leading-edge airfoils were barely visible.

While there may be concerns that the A10L25 tubercles, due to their extreme size, do not present the true effects of tubercles, the flowfield and the DSV evolution show a linear behavior with increasing tubercle amplitude. Figure 4.9 demonstrates this by displaying the spanwise vorticity at t^*=6 for the three airfoils tested, illustrating how tubercle size affects DSV dynamics. This figure also proves that as tubercle amplitude increases, the DSV position shifts progressively downstream, showing a direct correlation between tubercle magnitude and the downstream displacement of the DSV formation position. Additionally, the A05L25 airfoil, featuring milder tubercles, still exhibits signs of leading-edge vorticity discretization, similar to observations made with the A10L25 airfoil in both the instantaneous and phase-averaged data previously presented in the current section. This suggests that even less pronounced tubercles contribute to segmenting vorticity along the leading-edge. Moreover, the A05L25 configuration also diminishes DSV coherence, though to a lesser extent than the more extreme tubercles.

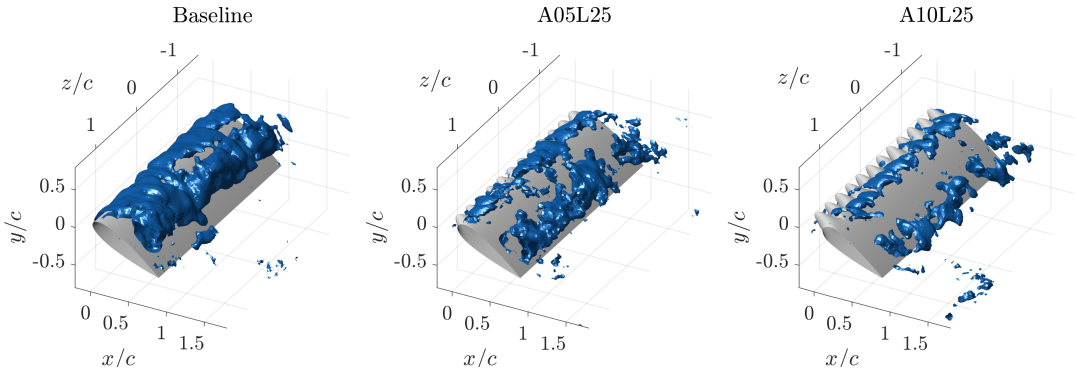

Figure 4.9: Vorticity iso-surface at $\omega_z c/U_\infty$=-9 for the three airfoils tested at t^*=6.

It can therefore be concluded that it is safe to analyze the effect of tubercles using the most extreme tubercle configuration. Furthermore, it is unlikely that an untested tubercle amplitude would demonstrate a different DSV behavior from what has been observed. The trends remain consistent across the tested range of amplitudes, providing a solid framework for understanding the impact of tubercle size. Consequently, the conclusions drawn from the baseline and A10L25 configurations are valid and applicable to smaller amplitudes. This approach will also be applied when presenting the CFD results in Section 4.2, where only the baseline and A10L25 airfoils will be discussed.

4.2. CFD flowfield characterization

The CFD results are in accordance with the experimental flowfield data. However, due to the turbulence modeling technique employed in the CFD computations, specifically the Unsteady Reynolds-Averaged Navier-Stokes (URANS) approach with the $k-\omega$ SST turbulence model, the CFD flowfield aligns better with the phase-averaged experimental data than the actual instantaneous experimental flowfield. This is because URANS inherently averages the Navier-Stokes equations over time, smoothing out transient fluctuations and focusing on the mean flow characteristics. Consequently, while URANS captures the general patterns and main features of the flow, it may not accurately replicate the transient, highly dynamic fluctuations present in instantaneous data. The phase-averaged data naturally reduces transient fluctuations to highlight dominant flow features, similar to the effects of the averaging process in URANS, resulting in a closer alignment with the CFD predictions.

Vorticity iso-surfaces at $\omega_z c/U_\infty$=-7 are displayed in Figure 4.10 for the baseline case. The primary difference from the experimental phase-averaged data is that during the initial phases of the motion, up to t^*=5, the vorticity shear layer extends across the entire airfoil in the chord direction, while the experimental data only show it extending to approximately $x_{AF}/c \approx$0.6. This discrepancy could be due to poor particle reconstruction near the airfoil surface, or because the particle concentration was not sufficient to capture such a thin flow feature.

At α=25.1°, a distinct region of vorticity near the leading-edge indicates the beginning of DSV growth as the boundary-layer vorticity accumulates near the leading-edge. Consistent with the experimental data, the CFD predictions also indicate that the DSV fully forms into a coherent vortex after t^*=5 and continues to strengthen until t^*=6.5, when the DSV detaches from the leading-edge vorticity source.

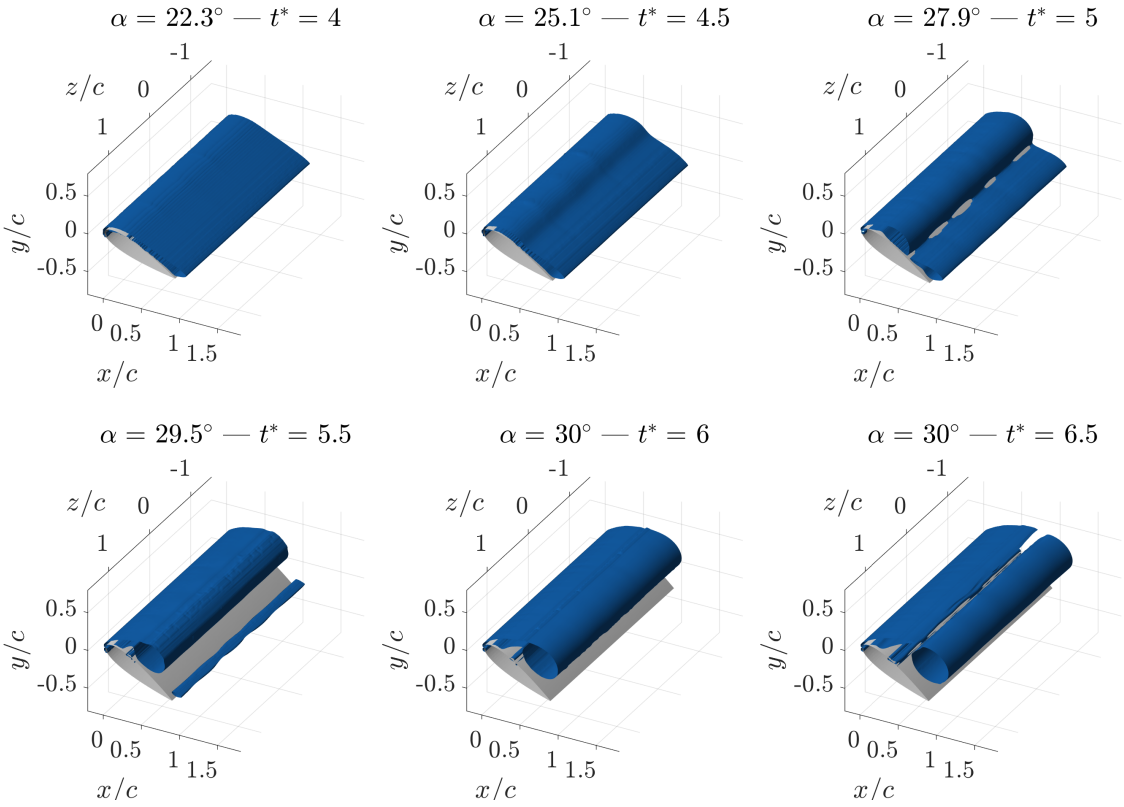

Figure 4.10: Vorticity iso-surface at $\omega_z c/U_\infty$=-7 for baseline airfoil predicted with CFD.

The CFD flowfield is also visualized using planes perpendicular to the span direction in Figure 4.11. When compared with the experimental data from Figure 4.2, it is clear that the DSV predicted by CFD is significantly more cohesive, displaying a well-defined core, which maintains its integrity over time and space, even after t^*=6.5, when it has almost convected a full chord distance.

An interesting flow feature to note is the secondary vortex that forms below the DSV as it moves away from the airfoil surface. This vortical structure, which was barely visible in the experimental data, is clearly discernible in the CFD results due to the enhanced resolution that is achieved with this method. From this series of images, it is easier to see how the DSV pushes the secondary vortex upstream, causing it to grow upward. This secondary vortex likely contributes to the detachment of the DSV from the leading-edge vorticity source, as its circulation pushes the leading-edge vorticity upstream. Hrynuk and Bohl (2020) also observed a tertiary recirculating region below the secondary vortex at α=30°, which is similarly visible in the current simulation. It is important to note that this flow feature is too small to be detected with PTV.

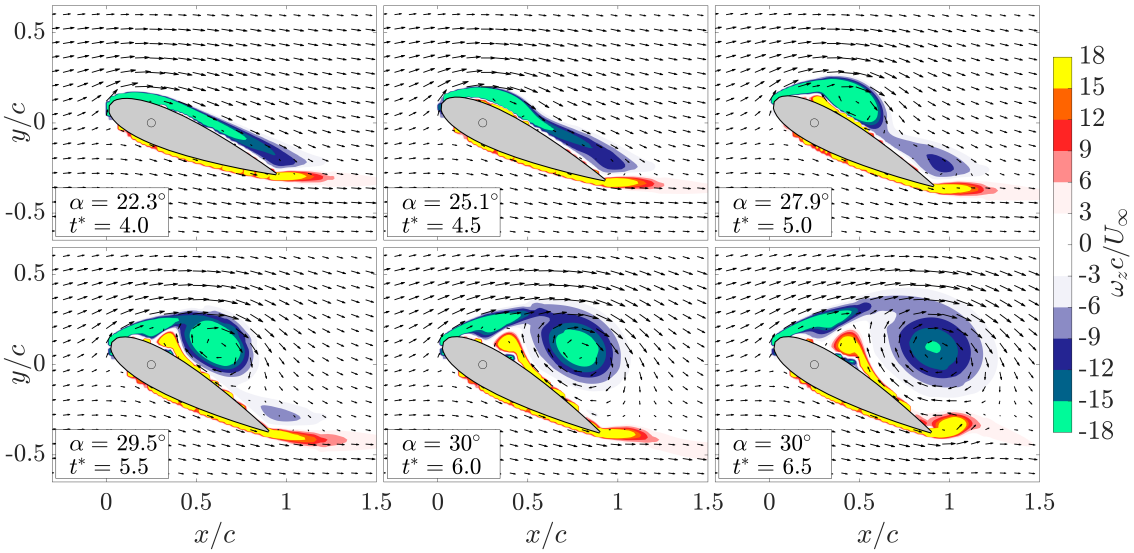

Figure 4.11: 2D vorticity flowfield for baseline airfoil at z/c=0 predicted with CFD.

In line with the baseline airfoil, the CFD results for the A10L25 airfoil also show good agreement with the experimental phase-averaged data. The flowfield in the CFD results is distinctly smoother and contains less noise, making interpretation inherently simpler. As observed in the experimental data, the troughs are the primary source of vorticity feeding into the DSV structure. It is also evident that the DSV forms closer to the trailing-edge. Interestingly, the DSV appears to have a larger diameter at the span positions aligned with the peaks, a phenomenon not observed in the experimental data where the DSV size is uniform across the span.

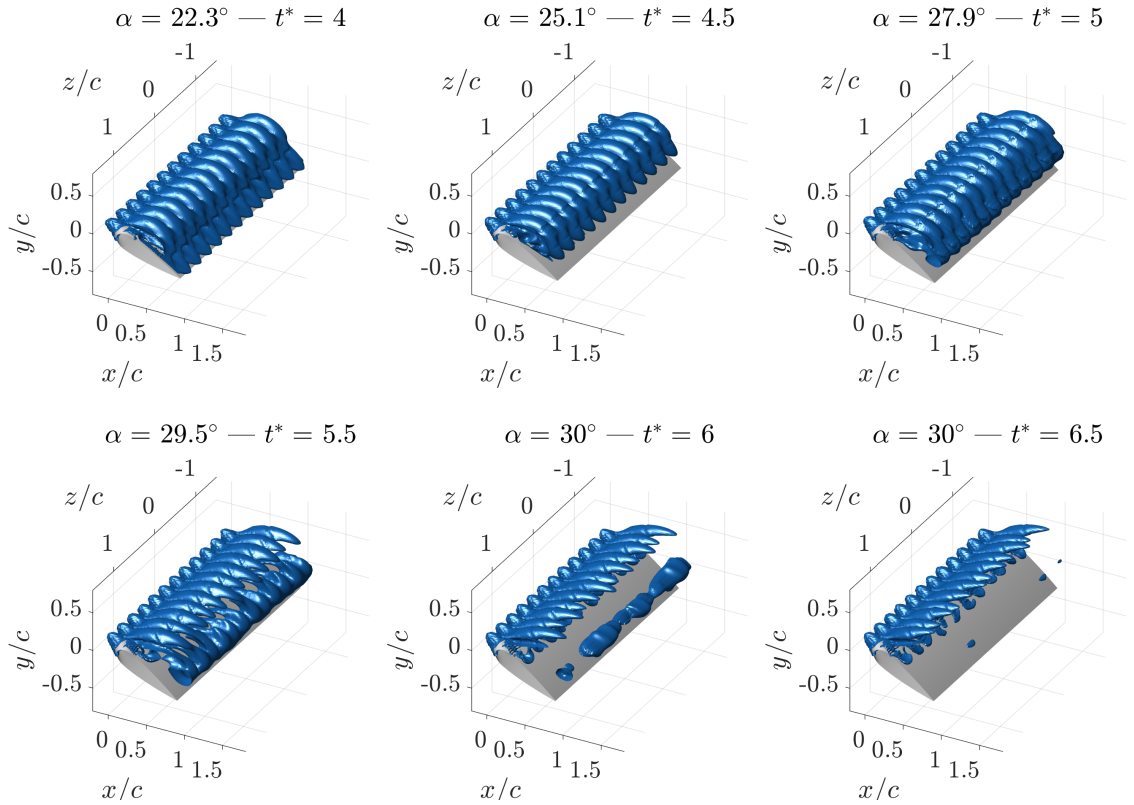

Figure 4.12: Vorticity iso-surface at $\omega_z c/U_\infty$=-7 for A10L25 airfoil predicted with CFD.

The CFD vorticity flowfield for peak plane is displayed in Figure 4.13. Consistent with the experimental findings, the flow remains attached for longer due to the downwash generated by the counter-rotating vortices. The DSV only forms after the trailing-edge shows noticeable signs of separation, which occurs around t^*=5.0.

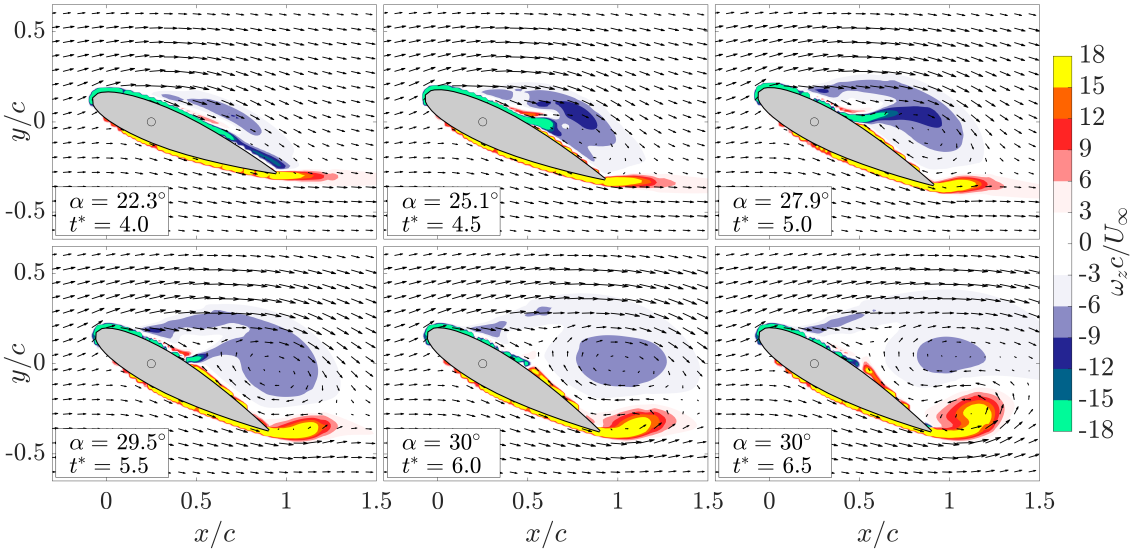

Figure 4.13: 2D vorticity flowfield for A10L25 airfoil at trough location z/c=0.125 predicted with CFD.

Unlike the experimental data, CFD reveals a secondary spanwise vorticity source positioned more upstream than the principal one which is located right before the flow reversal region. To shed some light on this phenomenon, Figure 4.14 displays the vorticity iso-surface at $\omega_z c/U_\infty$=-7 from a top view. From this perspective, it is evident that the secondary vorticity source is actually a segment of the trough vorticity source, clearly indicating that the secondary source does not originate in the peak plane, but instead from the neighboring troughs.

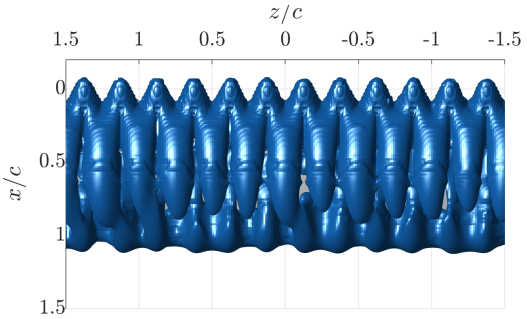

Figure 4.14: A10L25 airfoil vorticity iso-surface at $\omega_z c/U_\infty$=-7 predicted with CFD.

Figure 4.15 shows the CFD flowfield at the trough location located at z/c=0. In line with the experimental findings, the strong leading-edge vorticity source does not materialize into a DSV as coherent as that of the baseline. This is likely to be caused by the delayed separation at the peaks which prevents the roll-up of the boundary layer at the troughs. It is not after approximately α=28° at t^*=5.0 that the peaks start to present trailing-edge separation and the DSV is uniformly formed across the whole airfoil span. Moreover, as it has been already pointed out with the experimental 2D slices, the DSV is separated from the airfoil's surface during its formation phase earlier than in the baseline scenario. This is clearly visible at t^*=4 when the reverse flow has extended upstream below the DSV.

Another difference with respect to the baseline, which was not as discernible in the experimental data, is the direction of the leading-edge vorticity source. In the trough locations, the vorticity source is almost perpendicular to the airfoil chord, whereas in the baseline scenario, the vorticity source is aligned with the free-stream direction and closer to the suction side of the airfoil. This is caused by the upwash at the troughs generated by the streamwise counter-rotating pairs of vortices, which pushes the vorticity upwards right after the troughs. This flow feature is likely to have two consequences: first, it enhances the detachment of the DSV from the airfoil's surface during its growth stage, thereby enhancing its detachment from the leading-edge source and preventing it from increasing its strength. Note that initially, this was believed to be caused only by the trailing-edge separation extending upstream, but it is likely that the vorticity source direction also plays a role in this. Secondly, because of the strong upwash behind the troughs, the DSV formation position is further downstream, as the flow has to rotate for longer to form a vortical structure. This phenomenon could also potentially explain the lower vorticity levels at the trough sections than at the peak section. The troughs concentrate the vorticity but they push the flow upwards far from the airfoil surface preventing this vorticity to be fed into a clean vortex with a well-defined core close to the leading-edge.

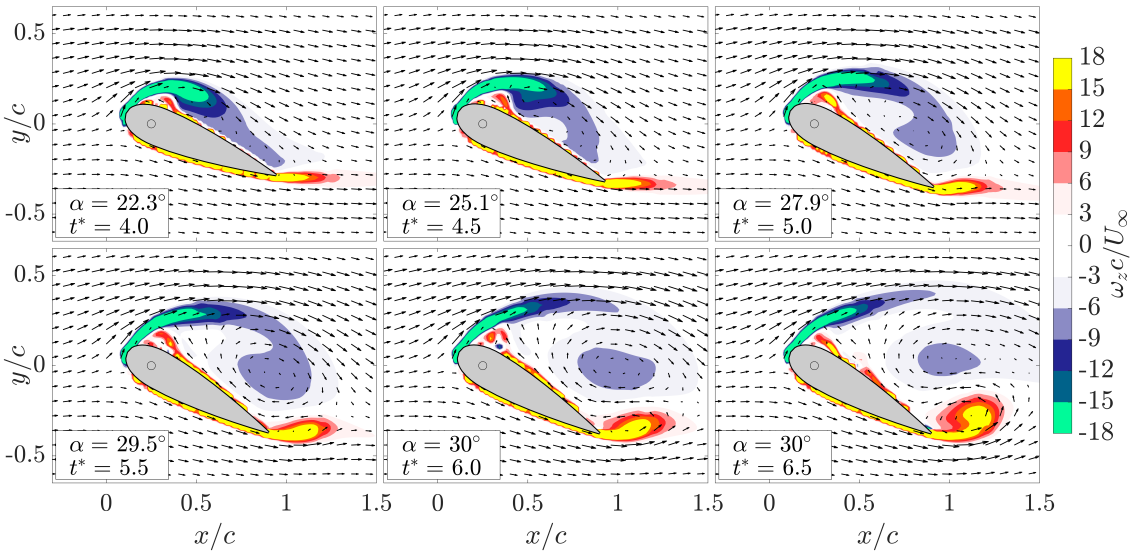

Figure 4.15: 2D vorticity flowfield for A10L25 airfoil at peak location z/c=0 predicted with CFD.

4.3. DSV temporal and spatial tracking

The convective path and strength of the DSV have a significant impact on the lift and drag characteristics of the airfoil [Carr et al. 1977; Jumper et al. 1987; Choudhry et al. 2014b]. Previously, the DSV has been characterized using flowfield analysis, which has been instrumental in depicting the temporal evolution of the DSV and its interaction with tubercles. However, this method primarily offers qualitative insights and falls short when assessing the effect of the tubercles quantitatively.

To address this gap, this section adopts a more analytical approach by employing the Γ_1 method to perform temporal and spatial tracking of the DSV during airfoil pitch-up motions. This technique allows for precise measurements of changes in the DSV formation location, convective path, size, and circulation, which are factors crucial for understanding the impact of the tubercles on aerodynamic performance. By quantitatively analyzing these parameters, it is possible to more accurately understand the tubercle effects on lift overshoot and enhance the clarity of the findings. Therefore, this quantitative assessment complements the flowfield visualizations presented in Sections 4.1 and 4.2.

4.3.1. DSV convective path

Following the methodology employed by Hrynuk and Bohl (2020), the DSV has been tracked in space and time during the pitch-up and hold airfoil motion using the Γ_1 method, as detailed in Section 3.3.1. Figure 4.16 displays the x_{AF}/c and y_{AF}/c for the three airfoils. The airfoil coordinate system is utilized, with the x_{AF} axis aligned with the chord direction and the origin set at the leading-edge of the smooth leading-edge airfoil. This specific frame of reference, also adopted by Hrynuk and Bohl (2020), is particularly suited for pinpointing the position of the DSV in relation to the airfoil, thus allowing for the study of relational effects between the DSV and the airfoil.

Tracking begins at t^*=5, when the airfoil is nearing its maximum angle of attack of α_1=30°. Prior to this time, the Γ_1 method could not effectively determine the position of the DSV core because it had not yet formed into a well-defined vortical structure. It has been detected, that for the tracking to be effective, a clear reversal flow region is necessary; otherwise, the vortex core cannot be successfully identified. It is important to note that since the pitch-up motion of the airfoil concludes by t^*=5, the subsequent movement of the DSV can be solely attributed to its convection rather than to a relative displacement between the DSV and the airfoil caused by the pitching motion.

The solid lines represent the spanwise average of the DSV core position at each measured instant, incorporating data from ten repetitions of each cycle. The shaded area covers the range within one standard deviation from the average. Given the DSV consistency across the span, averaging its position is justified and offers a clear view of its behavior during the convection phase.

From the tracking results, it is evident that the baseline DSV forms at $x_{AF}/c \approx 0.4$, while for the A05L25 and A10L25 airfoils, it forms at $x_{AF}/c \approx 0.6$ and $x_{AF}/c \approx 0.8$, respectively. In all three cases, the DSV forms at the same distance from the airfoil center-line. However, considering the thickness of the airfoil, the baseline DSV is closest to the surface during its formation phase as it forms near the position of maximum airfoil thickness. The velocity at which the DSV is convected is fairly similar across the three cases, although the baseline curve presents a reduced slope up to t^*=5.6.

Analysis of the tracking data indicates that for the baseline airfoil, the DSV remains over the suction side for an extended period. Additionally, the data consistently demonstrate an increase in the chordwise position of DSV formation with increasing tubercle amplitude. This trend suggests that larger tubercle amplitudes cause the DSV to form further downstream, affecting a smaller portion of the airfoil chord. Consequently, tubercles could be effective not only in reducing the intensity of lift overshoot but also in shortening its temporal duration. Although these conclusions could have already been reached from the flowfield analysis, the DSV tracking leads to the same conclusions but in a quantitative manner.

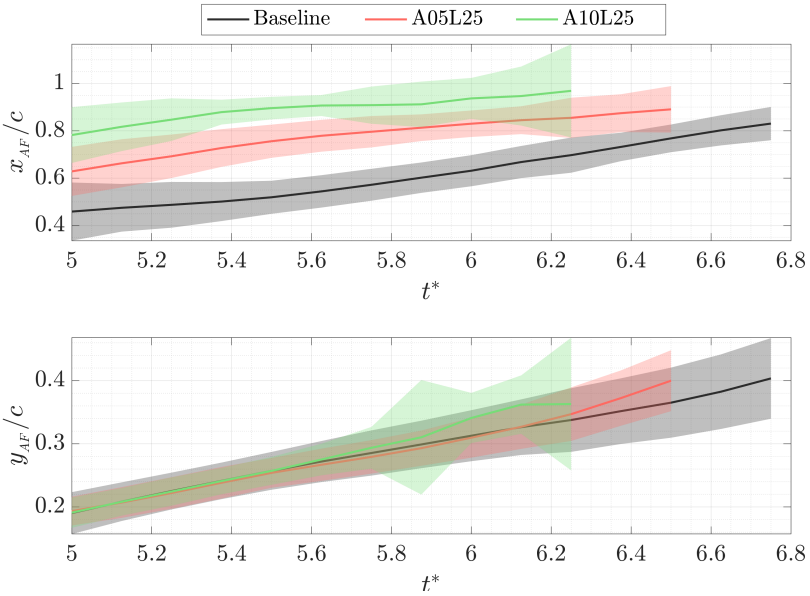

Figure 4.16: DSV convective path for k=0.05 and α_1=30°.

4.3.2. DSV vorticity and circulation

Once the vortex is located in space, its core radius can be determined. By integrating the vorticity within the core, the total circulation of the DSV is estimated. This approach, detailed in Section 3.3.1, has been used to determine the temporal evolution of the DSV core size r_{core} and its circulation Γ_{core}. Additionally, the DSV circulation has been calculated using a constant core size of 1 cm, defined as Γ_{const}. The evolution of the DSV radius and circulation over time is shown in Figure 4.17.

Circulation measurements using both the estimated DSV core and constant core radii confirm that the DSV associated with the smooth leading-edge airfoil remains consistently stronger throughout its life-cycle compared to that of the tubercled airfoils. However, the evolution of the circulation over time differs between the two methods. This divergence arises because the circulation calculated with the estimated core radius aims to capture the total circulation of the DSV, whereas the circulation computed with the constant radius focuses on the inner core, which contains higher levels of vorticity. The subsequent paragraph will justify the differences observed with both methods.

The circulation computed with the constant core radius, Γ_{const}, indicates that the baseline DSV is noticeably strengthened, increasing its core vorticity until t^*=5.4. Beyond this point, its circulation decreases monotonically. This pattern aligns with observations from Figures 4.2 and 4.11, which demonstrate that by $t^* = 5.5$, the DSV begins to separate from the leading-edge vorticity source, concluding its formation stage and entering the phase of convection where core vorticity starts to decay. For tubercled airfoils, the DSV exhibits a gentler trend, with a gradual increase in vorticity until t^*=5.5, followed by a subsequent decline.

Interestingly, the circulation computed with the time-dependent core radius Γ_{core} exhibits a distinct behavior: for all three airfoils, a parabolic evolution is observed, reaching a peak before the DSV circulation diminishes and the vortex breaks down. This increase in circulation is attributed to the DSV radius increase during the entire convection phase and the rotation induced by the undisturbed free-stream outside the disturbed region. The fact that the circulation computed with the constant area, which is significantly smaller than the core radius, decays over time indicates that the DSV becomes more diffuse as it convects downstream, although the DSV continues to increase its circulation.

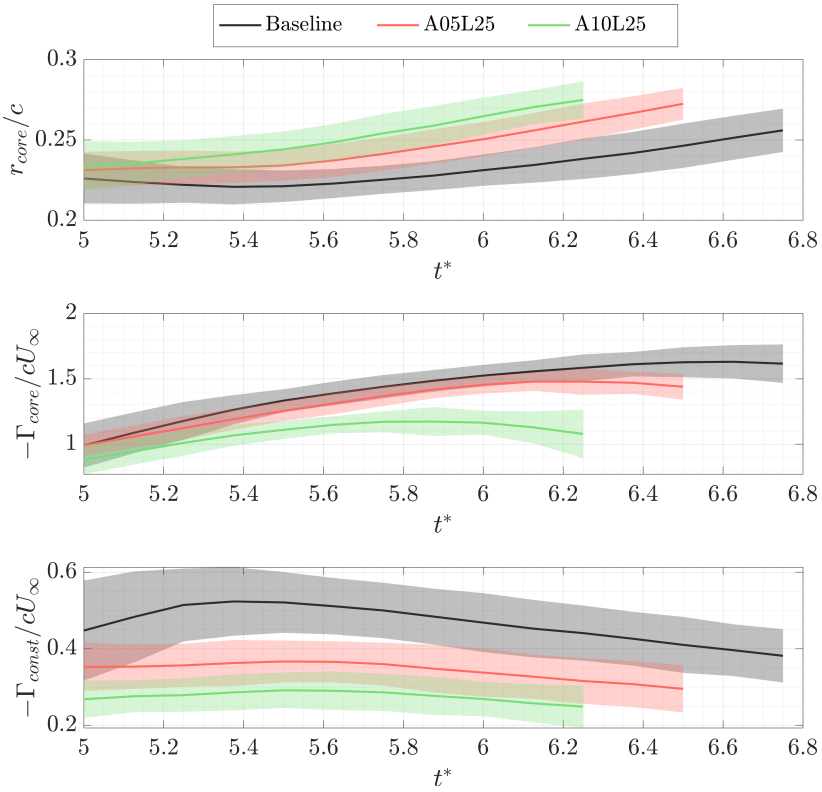

Figure 4.17: DSV circulation for k=0.05 and α_1=30°.

4.3.3. DSV effect on airfoil aerodynamic performance

Figure 4.18 summarizes the time-resolved evolution of the DSV and its circulation for the three airfoils studied in this research for the motion with k=0.05 and α_1=30°. The figure illustrates that the tubercles influence the chordwise location of DSV formation, with larger tubercle amplitudes leading to a more pronounced downstream shift. The baseline DSV forms more upstream and remains above the airfoil for a longer duration compared to the tubercled airfoils. Furthermore, from the previous Figure 4.17 it has been proved that tubercles tend to reduce the strength of the DSV during its convection phase.

These observations regarding the position and strength of the DSV suggest that the lift overshoot caused by the DSV is greater in the airfoil with a smooth leading-edge. Moreover, the baseline DSV forming further upstream implies a prolonged duration of lift overshoot compared to that experienced with the tubercled airfoils. On the other hand, the fact that the DSV position is shifted downstream for the tubercled airfoils suggests that these airfoils may suffer less from dynamic stall unsteadiness and reach a conventional deep stall regime quicker.

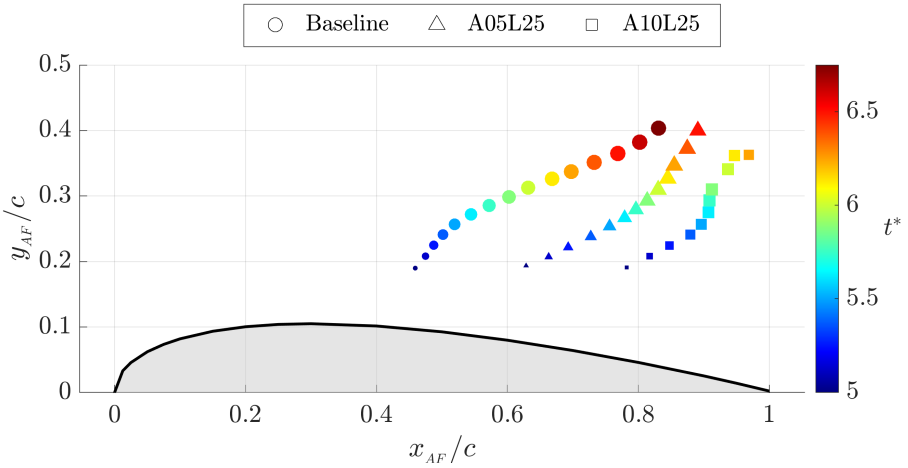

Figure 4.18: DSV tracking for k=0.05 and α_1=30°. The marker size is proportional to Γ_{core}.

4.4. Deep stall regime

The formation and convection phases of the DSV have been thoroughly investigated for airfoils with both smooth and tubercled leading-edge airfoils. These analyses are based on experimental results detailed in Section 4.1 and computational fluid dynamics simulations described in Section 4.2. Section 4.3 provides a quantitative assessment of the DSV circulation and trajectory, offering significant insights into the impact of tubercles on these phenomena. For the motion parameters considered, with a reduced frequency k=0.05 and an initial pitch angle α_1=30°, the lift overshoot concludes approximately at t^*=6.5. This marks the transition to a deep stall condition characterized by a rapid decline in dynamic lift and a subsequent stabilization of the aerodynamic loads after the flowfield has evolved into a steady state. This section aims to elucidate the aerodynamic behaviors observed during the deep stall phase and to outline the fundamental influences of the tubercles on this regime.

4.4.1. Stall compartmentalization

Figures 4.19 and 4.20 illustrate the evolution of the flow separation region after the DSV has been convected beyond the trailing-edge and the airfoil has entered a deep stall regime. These iso-surfaces show that both baseline and A10L25 airfoils present stall cells, with those on the baseline airfoil being significantly larger and exhibiting a more chaotic development. In contrast, in the tubercled airfoil, a clear compartmentalization effect is visible, and the stall cells align with the troughs. From the visualization of the tubercled airfoil stall cells, two main conclusions can be drawn: first, there is a consistent distance of two wavelengths between consecutive stall cells; second, the position of the stall cells remains unchanged throughout the entire motion. The fact that the stall cells are pinned in the tubercled case could potentially result in a more stable lift response during deep stall compared to the baseline airfoil.

In deep stall regime, both airfoils evolve into a state resembling a conventional stall. Here, tubercles function similarly as they do under static conditions, likely resulting in higher lift levels for tubercled airfoils, as already suggested by Johari et al. (2007) and Cai et al. (2017). This is due to the regions presenting attached flow between the stall cells, which benefit from the compartmentalization effect. Consequently, in these regions, the suction peak along the leading-edge is maintained, allowing the tubercled airfoils to produce more lift compared to the baseline airfoil, which experiences more severe flow separation extending over the entire airfoil span.

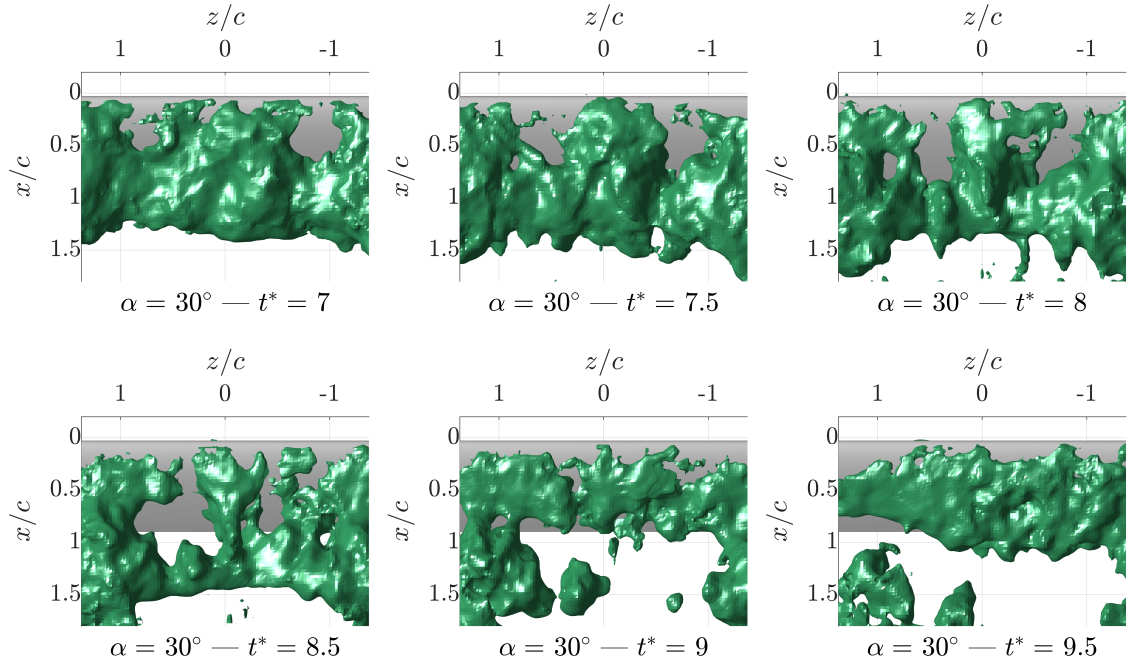

Figure 4.19: Reverse flow iso-surface at U_x=0 m/s for the baseline airfoil.

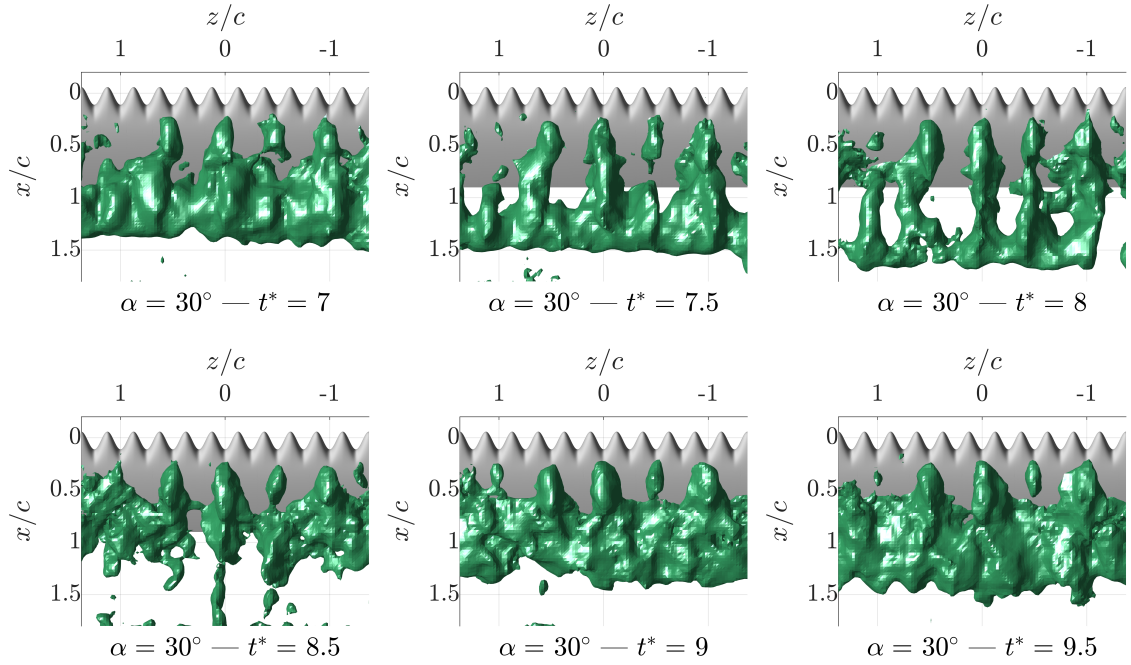

Figure 4.20: Reverse flow iso-surface at U_x=0 m/s for the A10L25 airfoil.

So far, the analysis of stall cells has primarily focused on their temporal evolution within a single pitching-up cycle. To assess whether the observations from one cycle hold true across repeated cycles, Figure 4.21 provides a comparative illustration of the stall cells at $t^* = 9$ for six different motion cycles. Interestingly, while the stall cells maintain consistent trough positions during each cycle, their positioning exhibits random variations across different cycles. It can also be observed that the spacing between consecutive stall cells varies, ranging from one to three wavelengths, with a predominant configuration of λ^*/λ=2.

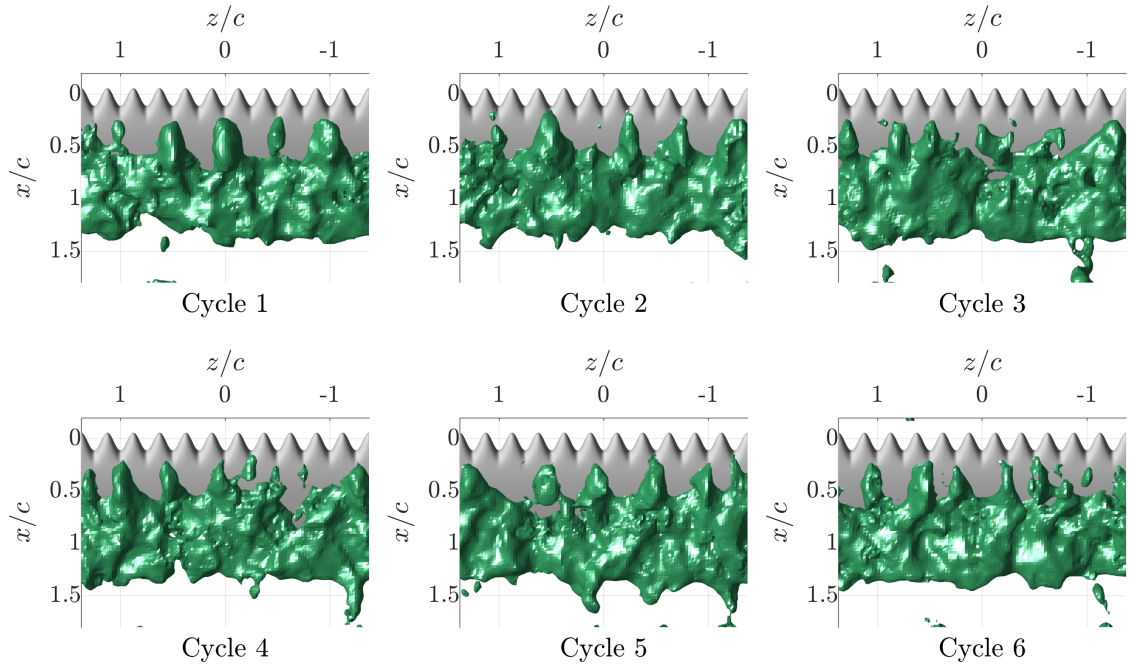

Figure 4.21: U_x=0 m/s iso-surface for the A10L25 airfoil at the six consecutive cycles at $t^* = 9$.

While Figure 4.20 illustrates the evolution of the stall cells for the A10L25 airfoil during the deep stall phase, the formation and interaction of these cells with the DSV has not been fully discussed yet. To address this, Figure 4.22 presents the stall cell evolution during the pitch-up motion, captured through PTV data. From t^*=4.5 to t^*=5.5, flow reversal regions become evident at nearly each trough, a phenomenon driven by the counter-rotating vortices induced by the tubercles. These vortices upwash over the trough span locations, enhancing separation in a manner similar to static conditions.

At t^*=6, coinciding with the maximum angle of attack α_1=30°, the DSV is distinctly observable as a cohesive vortex. It is during this moment that the stall starts reorganizing into fewer but larger stall cells. As the DSV moves away from the airfoil, these stall cells become higher and better defined while the attached regions between them extend downstream. The current study does not identify a clear interaction between the stall cells and the DSV; however, throughout the entire pitch-up phase, the stall cells remain positioned between the DSV and the airfoil surface, growing upward only after the DSV is convected downstream beyond the trailing-edge.

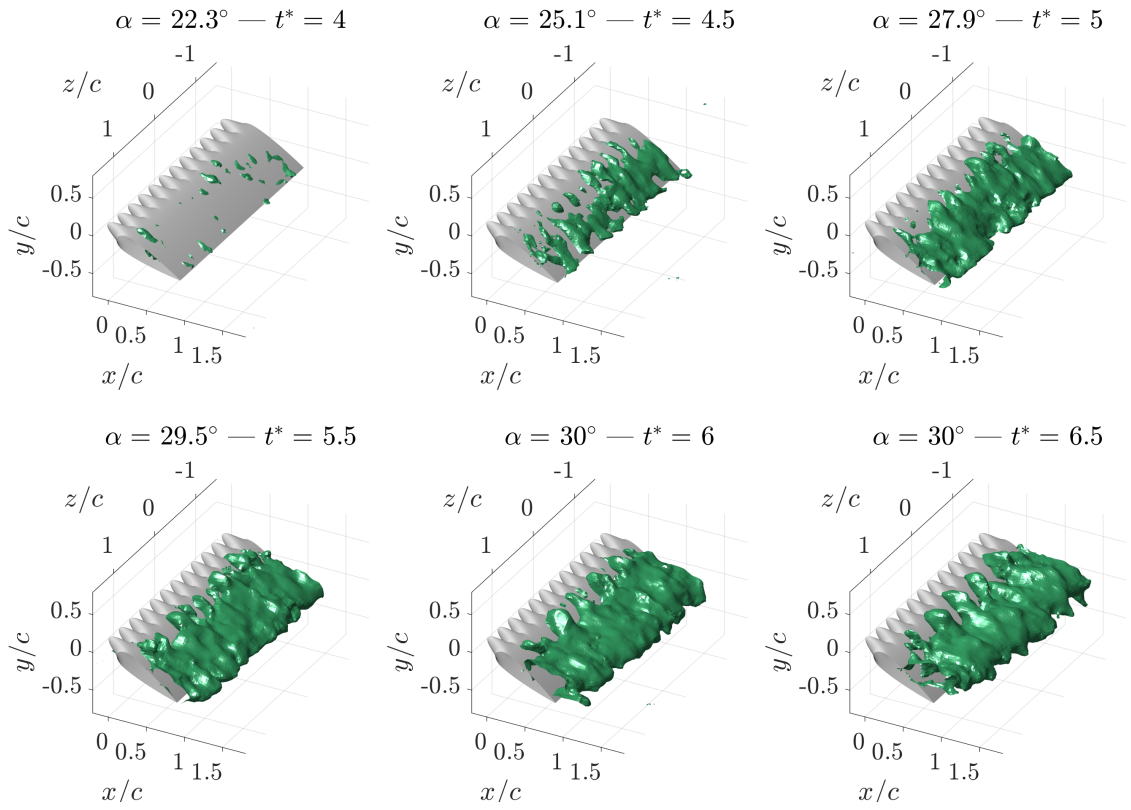

Figure 4.22: Evolution of the reverse flow iso-surface at U_x=0 m/s for the A10L25 airfoil during pre-stall regime.

4.4.2. Wake instabilities and vortex shedding

The wake evolution displayed in Figures 4.19 and 4.20 for the baseline and A10L25 airfoils illustrate an intriguing dynamic. Specifically, wake detachment occurs at t^*=8.5 for the baseline airfoil and at t^*=7.5 for the tubercled variant. Such wake dynamics have been documented in airfoils at angles of attack greater than $\alpha > 7°$ and at Reynolds numbers ranging from Re=1×10^4 to 1.5×10^5 [Chang et al. 2022; Fallahpour et al. 2023], aligning with the experimental conditions of this study. These studies indicate that at this low Reynolds numbers regime, the airfoils exhibit periodic vortex shedding, forming a vortex street downstream.

The wake detachment observed begins when the trailing-edge vortex, previously discussed in Sections 4.1 and 4.2, downwashes over the rear portion of the airfoil. As demonstrated in Figure 4.23, this downwash pushes the reverse flow region upstream, closer to the leading-edge. Subsequently, the rising trailing-edge vortex lifts the wake upwards. By t^*=9, the vortex elevates sufficiently to allow part of the free-stream flow to be pushed below it, effectively splitting the wake. After detachment, the trailing-edge vortex moves downstream too far from the airfoil to have any influence on the separated flow, and the wake stabilizes. A new spanwise vortex is then generated from the leading-edge, and the process is repeated. This alternating shedding pattern induces periodic fluctuations in the flow field, resulting in unsteady aerodynamic forces on the airfoil, as discussed in Section 4.5. Note that in Figure 4.23, a slice at $z/c = 0.75$ has been chosen for convenience to facilitate the explanation of the wake detachment process. In other span positions, this flow mechanism is not as clearly observed, or the wake does not detach at all. This is because the wake is highly unstable and exhibits variability across the span, complicating the observation of detachment in the instantaneous flow field at specific span locations. However, the phase-averaged flow field, which represents data averaged over multiple cycles, reveals a consistent pattern of wake detachment along the span. This demonstrates that while the precise locations of wake detachment may vary from cycle to cycle due to the flowfield unsteady nature, the general mechanism of wake detachment remains a consistent feature across cycles.

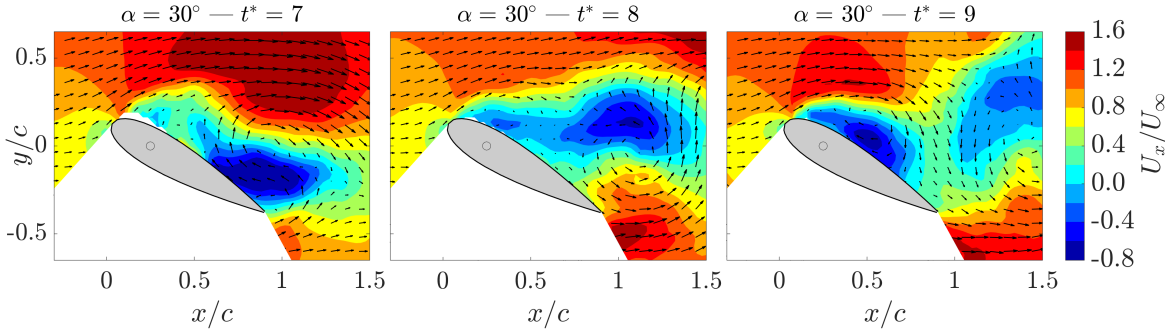

Figure 4.23: U_x flowfield for baseline airfoil at z/c=0.75.

Figure 4.24 presents the periodic vortex shedding by showing the vorticity iso-surfaces at both $\omega_z c/U_\infty$=-7 (blue) and $\omega_z c/U_\infty$=7 (red) for the baseline airfoil, based on PTV data. To improve the coherence of the vortices and thus aid the visualization and analysis, these iso-surfaces have been derived from the phase-averaged velocity field. The DSV is the most prominent vortex, distinctly visible at t^*=6.5. After dissipating by t^*=7.5, the trailing-edge vortex is formed as it rolls over the aft region of the suction side. By t^*=9.5, a second leading-edge vortex has already formed, though its strength is notably less than that of the DSV. This reduction in strength is primarily because the second leading-edge vortex does not benefit from the pitch-up motion that significantly enhances the circulation of the DSV.

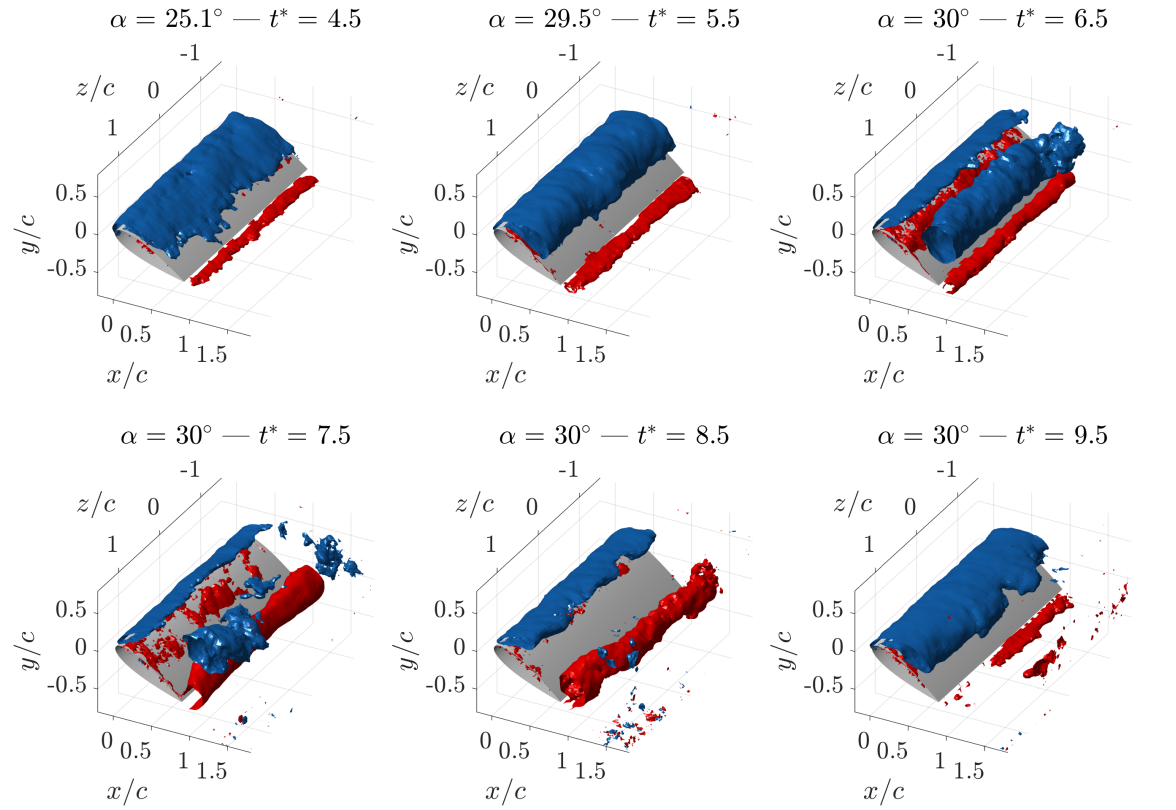

Figure 4.24: Baseline vorticity iso-surfaces at $\omega_z c/U_\infty$=-7 (blue) and $\omega_z c/U_\infty$=7 (red) showing the leading and trailing-edge spanwise vortices.

Figure 4.25 showcases the leading and trailing-edge vortices for the A10L25 airfoil, using the same thresholds for the iso-surfaces as those of the baseline. Two primary differences emerge: first, the DSV for the A10L25 airfoil forms further downstream, leading to its earlier convection past the trailing-edge compared to the baseline case. As a result, the trailing-edge vortex rolls up more rapidly, and the wake detachment occurs sooner. Although this vortical structure is stronger than that of the baseline, the second leading-edge vortex is substantially weaker. While the trailing-edge vortex exerts minimal impact on the aerodynamic forces of the airfoil, the leading-edge vortex, which is convected similarly to the DSV, significantly increases the lift.

These observations suggest that the baseline airfoil likely experiences more pronounced unsteady aerodynamic forces due to vortex shedding in the deep stall regime. Consequently, under deep stall conditions, the baseline airfoil may exhibit oscillations in lift and drag levels, whereas the tubercled airfoil displays a more stable response.

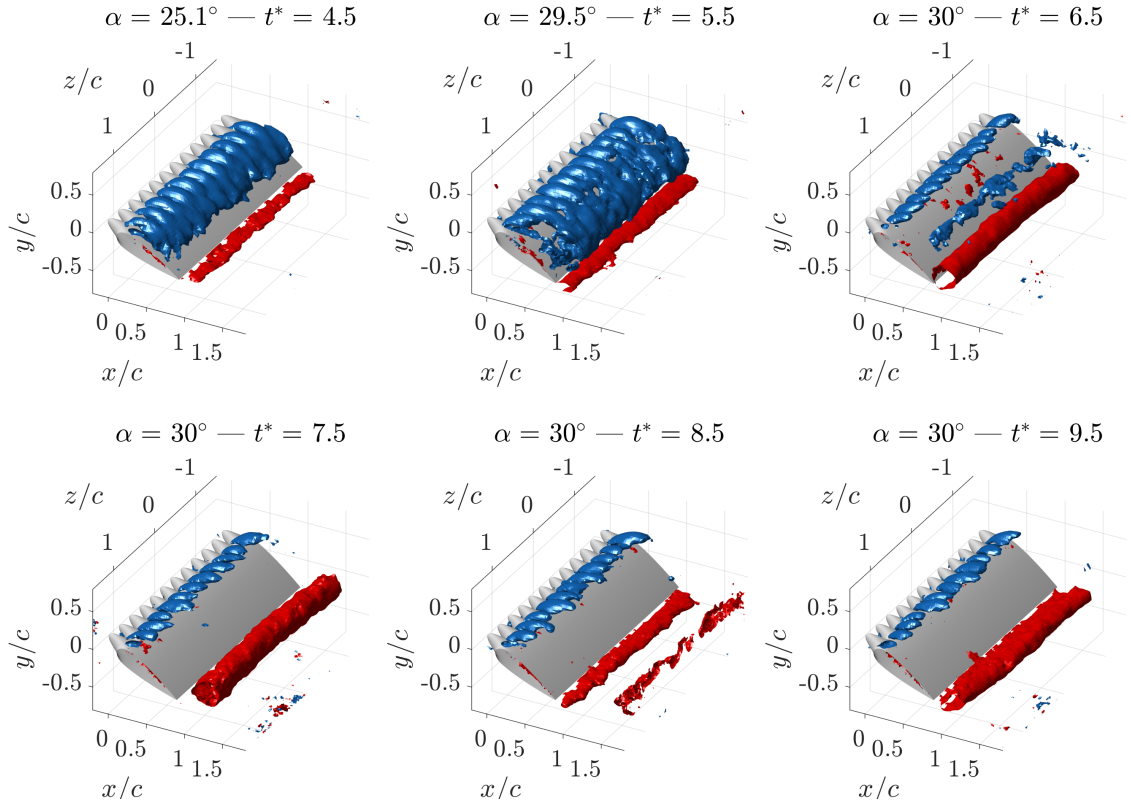

Figure 4.25: A10L25 vorticity iso-surfaces at $\omega_z c/U_\infty$=-7 (blue) and $\omega_z c/U_\infty$=7 (red) showing the leading and trailing-edge spanwise vortices.

4.5. Aerodynamic forces

While the experimental setup did not allow for direct measurement of aerodynamic forces, insights into the evolution of these forces during airfoil motion have been derived from the flowfield observations in both experimental and CFD analyses. These flowfield examinations have led to several key conclusions regarding the impact of tubercles on the dynamic stall phenomenon:

- Tubercles shift the formation of the DSV downstream.
- Tubercles decrease the circulation of the DSV during its convection phases.
- Tubercles diminish the strength of both leading- and trailing-edge vortices shed during the deep stall regime.
- Tubercles pin the stall cells at the troughs reducing the wake oscillations.

Given these findings, this chapter utilizes CFD-derived aerodynamic forces to quantify the specific impact of tubercles on the airfoil aerodynamic forces and evaluate whether the conclusions drawn from the flowfield are consistent with the aerodynamic forces. This approach complements the limitations of the experimental method providing a detailed understanding of how tubercles alter the aerodynamic performance throughout the pitch-up and hold motion, which is crucial for understanding the aerodynamic benefits of tubercles on airfoils in dynamic stall conditions.

The CFD methodology, as detailed in Section 3.2, has been employed to analyze the dynamic behavior of the three studied airfoils: baseline, A05L25 and A10L25, at k=0.05 and α_1=30°. Although the CFD aerodynamic forces depicted in Figure 4.26 may not align perfectly with the hypothetical experimental data, a comparative review of the PTV and CFD flowfield discussions presented in Sections 4.1 and 4.2 confirms that both methods converge on similar conclusions. Consequently, the aerodynamic forces predicted by CFD are considered a trustworthy representation of the experimental scenario.

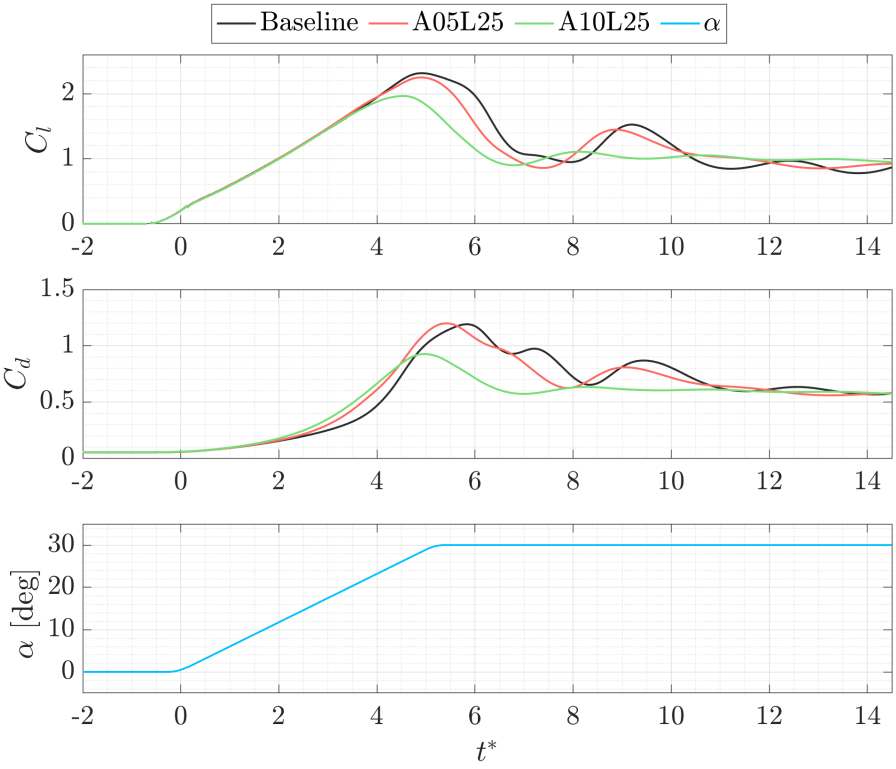

Figure 4.26: Aerodynamic forces computed with CFD for baseline, A05L25, and A10L25 airfoils undergoing pitch up and hold motion with $k = 0.05$ and $\alpha_1 = 30°$.

The aerodynamic loads derived from the CFD flowfield are consistent with the conclusions drawn from the flowfield analyses. The smooth leading-edge airfoil exhibits the strongest lift overshoot, correlating with the highest DSV circulation levels among the three airfoils studied. Furthermore, because the baseline DSV forms further upstream and remains over the airfoil for a more extended period, the lift overshoot persists for nearly two convective times. In contrast, this effect is significantly diminished in airfoils with tubercles, where the DSV forms closer to the trailing-edge, thus reducing the duration of lift enhancement. The increase drag for the baseline airfoil is a direct consequence of of the DSV low pressure core which increases the pressure drag of the airfoil. Notably, the A05L25 airfoil, which features tubercles at half the amplitude of those on the A10L25, exhibits an intermediate behavior between the baseline and the A10L25 airfoils. This observation, previously pointed out in the tubercle amplitude study presented in Section 4.1.4, is now further confirmed by the CFD data, confirming the gradual influence of tubercle amplitude on aerodynamic performance.

In deep stall regime, which begins around t^*=8, the A10L25 airfoil exhibits the most stable aerodynamic lift response. This stability is contrasted with smaller, yet noticeable, load oscillations in the A05L25 airfoil and significant fluctuations in the baseline airfoil. As discussed in Section 4.4.1, the stability in the A10L25 can be attributed to the flow reversal regions being consistently pinned at the troughs, which helps mitigate aerodynamic fluctuations. However, while the wake oscillations justify the lift oscillations after t^*=10, the second lift peak observed for the baseline and A05L25 airfoils is too pronounced to be solely caused by wake oscillations. Instead, this second peak is triggered by the shedding of a second leading-edge vortex after the trailing-edge vortex has split the wake, as described in Section 4.4.2. This peak is of reduced strength because the leading-edge vortex possesses significantly less vorticity than the DSV and does not benefit from the pitch-up motion during the growth phase.

From the evolution of aerodynamic forces, it can be inferred that the large unsteadiness associated with periodic vortex shedding lasts for two periods. After the second trailing-edge vortex is shed around t^*=12, the aerodynamic forces on the three airfoils stabilize, mirroring their behavior under static conditions. This does not imply that periodic vortices are no longer shed, but instead, their circulation is significantly reduced and has a rather small effect on the total lift. At this point, although the A10L25 airfoil shows slightly higher lift levels, the differences among the airfoils are almost negligible. This minimal variation can be attributed to the airfoil being pitched up to an angle of attack α_1=30°, which is well beyond the static stall angle. At such high angles, the benefits of tubercles are significantly diminished. This observation aligns with previous research on tubercled airfoils in static conditions. Cai et al. (2017) studied a tubercled airfoil A10L25 with a NACA 63_4-021 cross-section at a Reynolds number of 1.8×10^5 and concluded that at α=30°, the tubercles offer minimal lift advantage compared to a smooth leading-edge wing. This limited advantage is due to the fact that, although the compartmentalization effect was visible, the attached flow regions did not extend beyond $x_{AF}/c \approx 0.5$, significantly reducing negative pressure along the tubercled airfoil's leading-edge. Similarly, Yasuda et al. (2019) pointed out that the benefits of tubercles vanish around α_1=30°. Their CFD simulations were conducted at Reynolds numbers ranging from $1\times10^4 \leq Re \leq 6\times10^4$, similar to the Reynolds number of 3.3×10^4 used in the current research. In line with these findings, it is to be expected that if the airfoil is pitched to angles of attack above the static stall angle but lower than α_1=30°, the tubercled airfoil may present significantly higher lift levels than the smooth-leading airfoil.

4.5.1. Pressure field

A significant advantage of using CFD over PTV experiments is the availability of the pressure field. Figure 4.27 illustrates the pressure field for the baseline airfoil alongside the trough and peak planes of the A10L25 airfoil at t^*=5, which corresponds to the moment when the baseline airfoil exhibits the maximum lift coefficient. Figure 4.28 displays the vorticity field at the same time instant. At this moment, the baseline DSV remains attached to the leading-edge vorticity source, and the secondary vortex has not pushed it upward yet. The DSV low pressure region is notably compact, aligning closely with the vorticity field and extending from the leading-edge to approximately $x_{AF}/c \approx 0.6$. In contrast, the DSV of the A10L25 airfoil is situated further downstream around $x_{AF}/c \approx 0.8$.

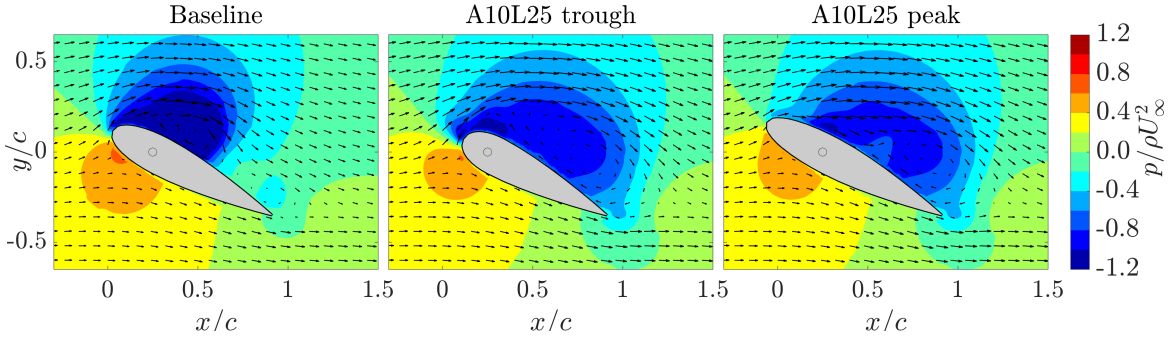

Figure 4.27: Pressure field at t^*=5 for the baseline airfoil and the trough and peak planes of the A10L25 airfoil, corresponding to the time at which the baseline presents the maximum lift coefficient.

Analysis of the velocity field vectors shows that while the rotational field associated to the A10L25 DSV is well-defined, the DSV vorticity is significantly lower compared to that of the baseline. Additionally, the low pressure region associated with the A10L25 is more dispersed and less intense, resulting in a lower lift coefficient.

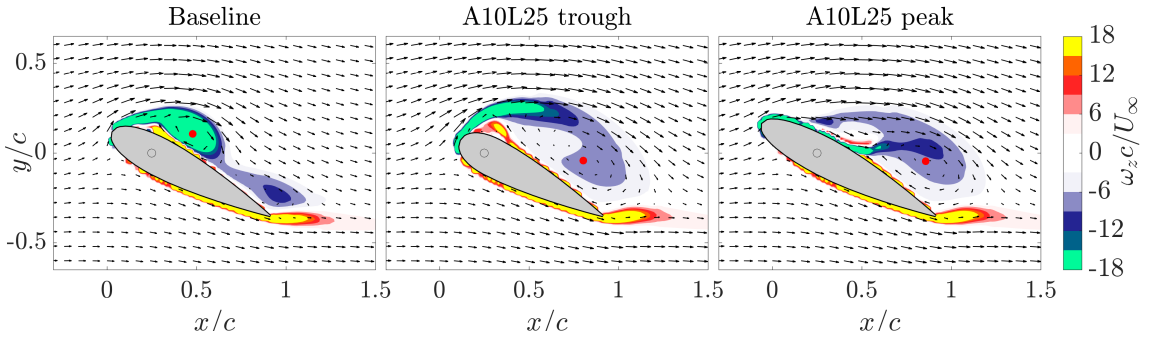

Figure 4.28: Vorticity field at t^*=5 for the baseline airfoil and the trough and peak planes of the A10L25 airfoil, corresponding to the time at which the baseline presents the maximum lift coefficient. The DSV core positions are indicated with red dots.

At t^*=6, the A10L25 has already lost almost all the lift caused by the low pressure core of the DSV (see Figure 4.29), while the baseline airfoil still maintains a lift coefficient of $C_l = 0.86C_{l,max}$. Figure 4.30 illustrates the vorticity field at this same instant. For the tubercled airfoil, the DSV has almost dissipated, but for the baseline, the vortex remains well-defined and cohesive at approximately $x_{AF}/c \approx 0.6$. Its low-pressure core continues to extend over almost the entire suction side, sustaining significant lift.

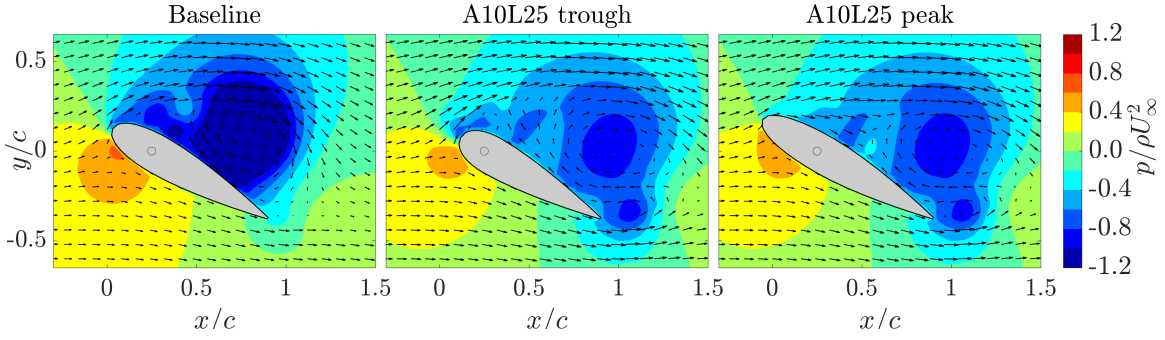

Figure 4.29: Pressure field at t^*=6 for the baseline airfoil and the trough and peak planes of the A10L25 airfoil.

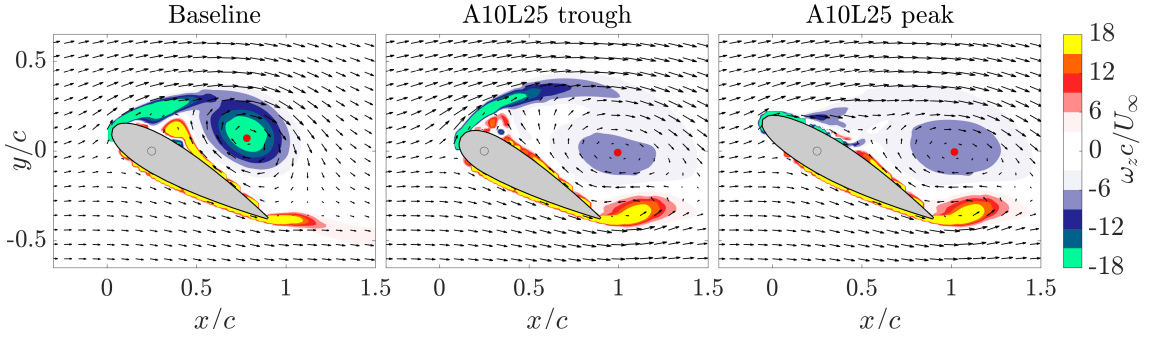

Figure 4.30: Vorticity field at t^*=6 for the baseline airfoil and the trough and peak planes of the A10L25 airfoil. The DSV core positions are indicated with red dots.

This pressure field analysis validates the direct relationship between DSV circulation and the low pressure within its core. Notably, the baseline DSV exhibits a core with lower pressure compared to those in tubercled airfoils. Additionally, the proximity of the DSV formation position to the leading-edge in the baseline airfoil enhances pressure propagation across the entire airfoil chord. This detailed understanding of pressure dynamics further supports the effectiveness of CFD in capturing the unsteady flow features associated with the dynamic stall phenomenon.

4.6. Tubercle performance across different pitching conditions

The previous analyses in this thesis have examined the impact of tubercles at specific pitch-up and hole motion settings, with a pitching rate of k=0.05 and a maximum amplitude of α_1=30°. This section extends the study to higher pitching rates and amplitudes, specifically to k=0.1 and α_1=55°. The objective is to determine how the effect of tubercles varies with changes in motion parameters, thereby broadening the understanding of their influence under different dynamic conditions.

4.6.1. Pitching rate effect

The influence of pitching rate on smooth leading-edge airfoils undergoing dynamic stall has been detailed in Section 2.1.2. Research has established that changes in pitching rate significantly influence both the onset and progression of dynamic stall on airfoils. Specifically, increasing the pitching rate leads to a noticeable delay in stall onset. This change is coupled with substantial alterations in the DSV, impacting its strength and altering the timing of its formation. Notably, higher pitching rates cause the DSV to form closer to the leading-edge and with increased circulation. Previously, these effects were mainly observed in airfoils with smooth leading-edges. However, the study by Hrynuk and Bohl (2020) extends these findings to tubercled airfoils, demonstrating that the effects of pitching rate on dynamic stall characteristics are consistent, regardless of variations in leading-edge geometry.

The experimental flowfields are evaluated to determine if the findings from prior literature apply to this research, and to assess whether conclusions drawn from motions with k=0.05 and a maximum amplitude of α_1=30° are valid at different pitching rates. In this context, Figure 4.32 displays the DSV path for both the baseline and A10L25 airfoils at k=0.05 and 0.1. To aid in understanding the results presented in this section, Figure 4.31 shows the temporal evolution of the angle of attack during the airfoil motion for both cases.

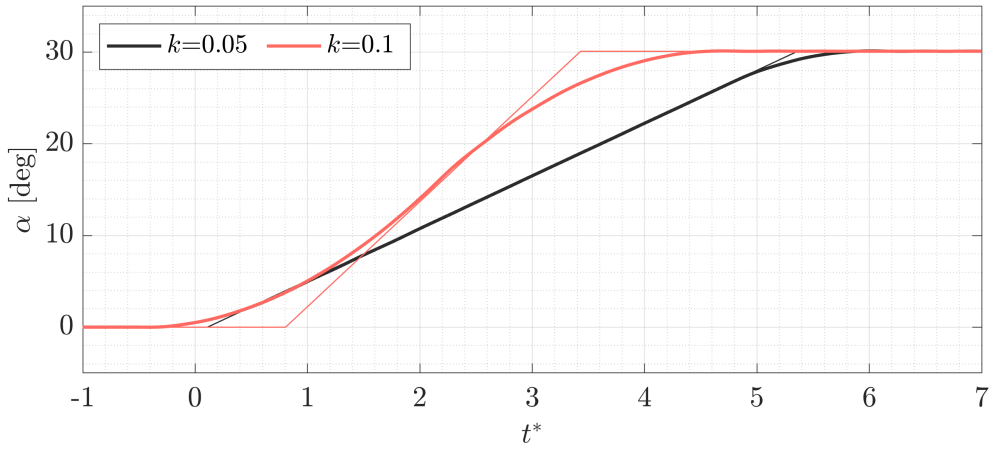

Figure 4.31: Stage motion for pitch-up and hold motion with k=0.05 and 0.1.

Consistent with existing research, an increase in pitching rate results in an upstream shift of the DSV position of formation. However, a delay in the onset of dynamic stall is not observed, as the DSV forms at the end of the pitch-up phase when the maximum angle of attack is reached for both pitching rates.

The impact of the pitching rate on the DSV strength is shown in Figure 4.33, where DSV circulation is presented for both the baseline and the A10L25 airfoils. Analyzing the inner core circulation Γ_{const}, it is apparent that the DSV core exhibits higher circulation for the highest pitching rate. Yet, this enhanced circulation is not evident when the estimated DSV radii are considered for the vorticity integration, suggesting that increasing the pitching rate leads to a more cohesive DSV structure rather than a stronger one. It is important to note that due to limitations in the maximum acceleration achievable by the rotary stage, the motion at k=0.1 did not closely match the controller input, resulting in extended periods of acceleration and deceleration. This discrepancy could potentially hinder the impact of increasing the pitching rate since, although the airfoil underwent a quicker pitch-up motion, it spent a significant portion of the cycle in acceleration and deceleration phases rather than maintaining maximum speed.

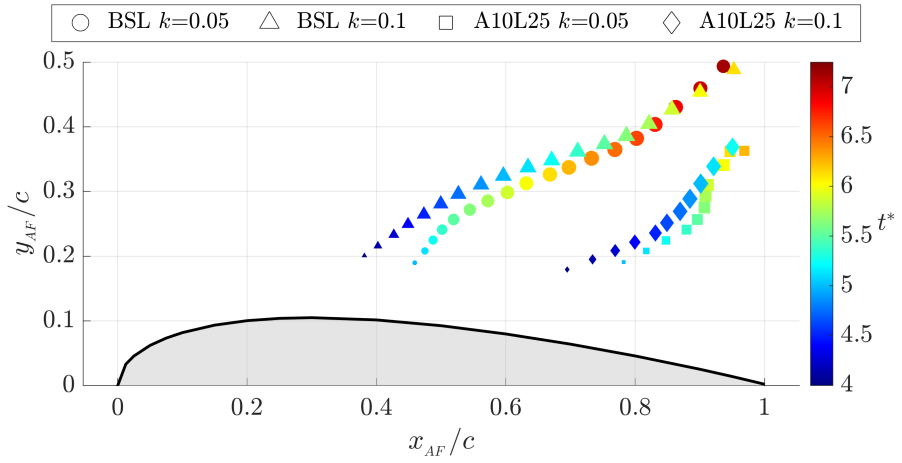

Figure 4.32: DSV tracking for k=0.05 and 0.1 with α_1=30°. Marker size is proportional to Γ_{core}.

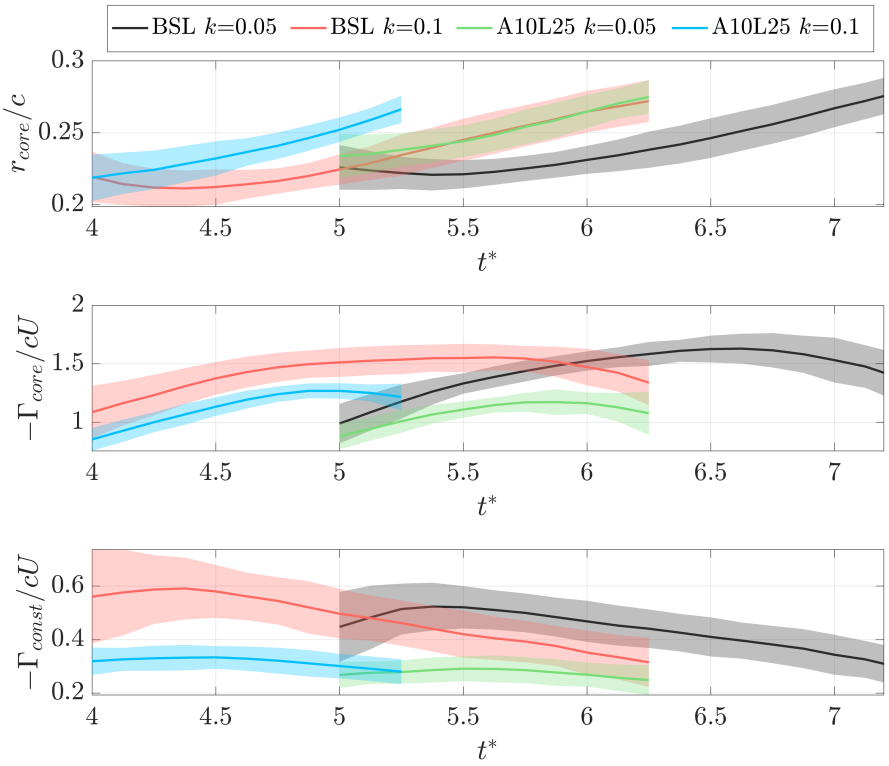

Figure 4.33: DSV circulation for k=0.05 and 0.1 with α_1=30°.

Notably, the impact of tubercles on dynamic stall characteristics remains consistent across varying pitching rates. This consistency suggests that even at a higher pitching rates of k>0.1, tubercles are likely to result in a weaker and shorter lift overshoot, similar to the effects observed at lower pitching rates.

4.6.2. Amplitude effect

During the experiments, the airfoils were pitched to angles of attack up to α_1=30° and 55°. Consequently, the experimental data have enabled a comprehensive assessment of the impact of the motion amplitude on the DSV and the effect of tubercles. For clarity, Figure 4.34 illustrates the evolution of the angle of attack throughout both motions.

Figure 4.35 presents the DSV paths for both the baseline and A10L25 tubercled airfoils at a reduced frequency k=0.1. To support the following discussion, this figure also includes the direction of the free-stream for the scenario with α_1=55°. Highlight the fact that this is not needed for the airfoil pitching up to 30°, since the DSV is only tracked after the maximum amplitude has been reached.

This figure clearly demonstrates that the convective path of the DSV is significantly altered when the amplitude of the motion changes. For the airfoils pitched to α_1=30°, the DSV remains proximate to the airfoil for an extended duration compared to those at 55°, despite both scenarios initiating the DSV formation simultaneously. This variance in DSV trajectories results from the prolonged motion at the higher angle of attack. Specifically, at t^*=4, while the airfoil pitching to α_1=55° continues its upward pitch, the movement has already finished for the α_1=30° scenario. This results in the airfoil chord region downstream of the pitching axis at x_{AF}/c=0.25 effectively moving away from the DSV as it convects downstream for α_1=55° case. After t^*=5.5, as the airfoil begins to slow its motion, the DSV path better aligns with the free-stream direction, as denoted by the red arrow.

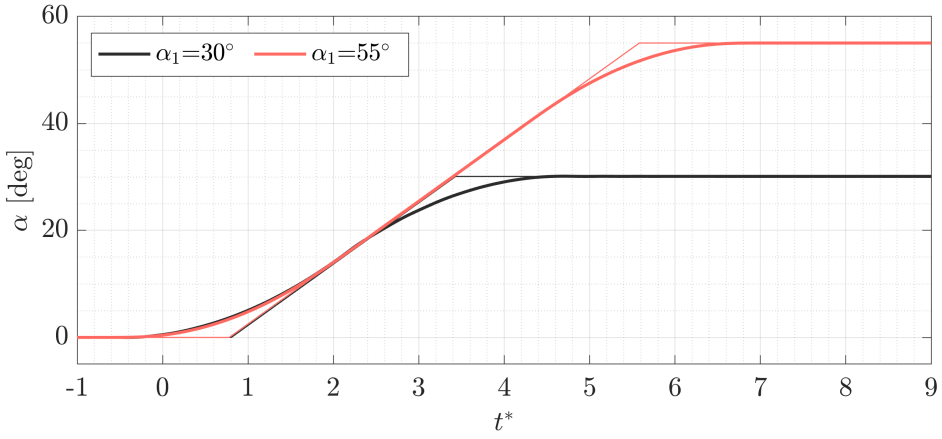

Figure 4.34: Stage motion for pitch-up and hold motion with α_1=30° and 55°. The arrows indicated the free-stream direction for the case of α_1=55°.

The influence of motion amplitude on the circulation characteristics of the DSV is distinctly illustrated in Figure 4.36. For both the baseline and the tubercled airfoils, it has been observed that increasing the final angle of attack results in a more pronounced DSV, characterized by a larger size and enhanced circulation. Furthermore, the experimental results have demonstrated that the effect of tubercles on the DSV remains consistent, irrespective of the increase in motion amplitude, suggesting that the influence of tubercles on the behavior of the DSV, particularly in terms of vortex formation, and convective path, does not vary significantly with changes in amplitude. Consequently, it can be asserted that the conclusions drawn from experiments conducted with α_1=30° are equally applicable to scenarios involving larger amplitudes.

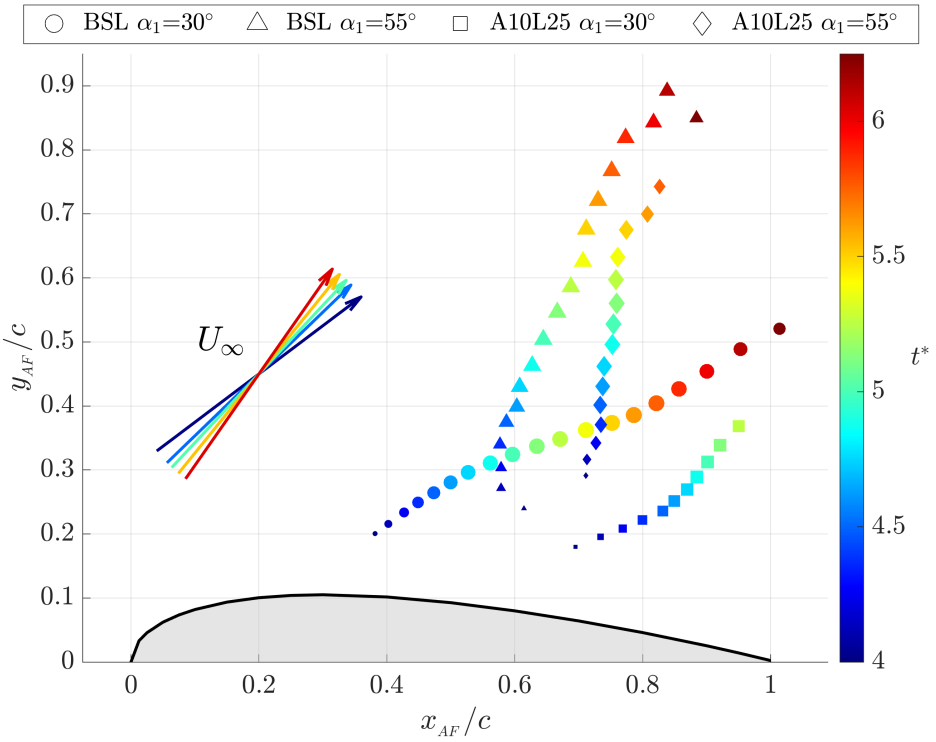

Figure 4.35: DSV tracking for α_1=30° and 55° with k=0.1. Marker size is proportional to Γ_{core}.

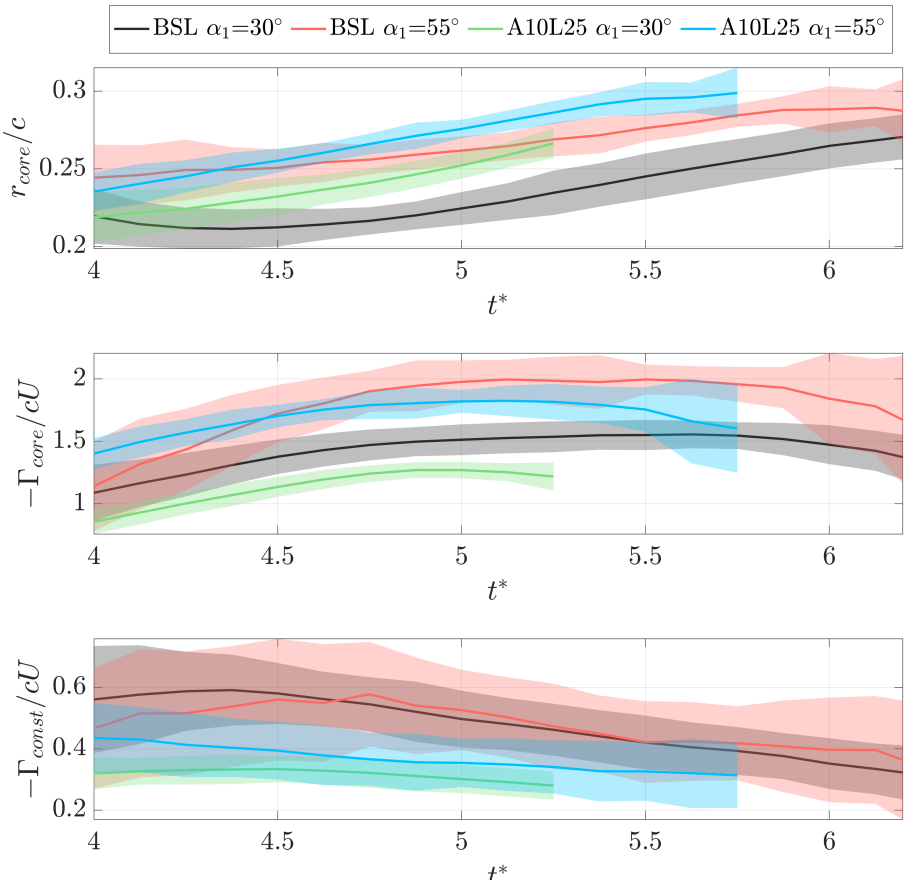

Figure 4.36: DSV circulation for α_1=30° and 55° with k=0.1.

5

Conclusions and Recommendations

5.1. Conclusions

This thesis has explored the effects of leading-edge tubercles on the aerodynamic performance of airfoils experiencing dynamic stall conditions as a result of pitch-up and hold motions. The study combined experimental analysis using particle tracking velocimetry (PTV) and computational fluid dynamics (CFD) simulations to examine the flow mechanisms affected by the addition of tubercles.

The goal of this research was to investigate changes in dynamic stall behavior and overall aerodynamic performance due to the leading-edge tubercles. This has been achieved by performing a three-dimensional characterization of the dynamic stall vortex (DSV), evaluating aspects of the DSV such as the timing and chordwise position of formation, its convective path, and its circulation. Furthermore, the impact of tubercles in the deep stall regime has been examined by analyzing the temporal evolution of stall cells and their interaction with the DSV. The results from both experiments and simulations provide valuable insights into the flow dynamics of pitching airfoils with and without tubercles, highlighting potential benefits for airfoils that frequently encounter dynamic stall conditions.

The conclusions of this work are divided into two main parts. First, the research questions are answered providing a detailed summary of the effects of tubercles on airfoils during pitch-up and hold motions, building on the discussion from the results chapter. The second part discusses the experimental and computational methods, summarizing key findings regarding the suitability of each method for investigating dynamic stall on smooth leading-edge and tubercled airfoils.

5.1.1. Research questions

The research questions outlined in the introduction (see Section 1.1) are revisited hereinafter. Each question is addressed individually, with the aim of conducting a thorough examination and ensuring that the conclusions drawn are well-supported by the results.

1. How do tubercles affect the dynamic stall phenomenon?

1.1. Do tubercles delay the formation of the DSV?

Based on the results presented in this thesis, it is evident that tubercles on airfoils cause a spatial delay in the formation of the dynamic stall vortex. This delay is characterized by the DSV forming further downstream closer to the trailing-edge compared to the baseline configuration without tubercles.

The introduction of tubercles alters the aerodynamic flow around the airfoil, affecting how and where the DSV develops during dynamic stall conditions. Specifically, the tubercles create streamwise counter-rotating vortex pairs that produce downwash at peak span locations and upwash at troughs. This significantly impacts the peak planes, where downwash prevents boundary layer roll-up and the subsequent spanwise vorticity concentration near the leading-edge, which typically leads to DSV formation. Consequently, the DSV forms only when a noticeable region of reverse flow near the trailing-edge appears at the peak locations. At the troughs, although the leading-edge separation

occurs significantly earlier than at the baseline and peaks, the upwash triggers the early separation of the DSV from the airfoil. Furthermore, the leading-edge vorticity source is almost perpendicular to the free-stream, making it difficult to form a coherent vortical structure near the leading-edge, as observed with the baseline airfoil.

Tracking the DSV with the Γ_1 method provides robust evidence of these changes. The tracking results show that the baseline DSV forms at approximately $x_{AF}/c \approx 0.4$, while for the A05L25 and A10L25 airfoils, it forms at $x_{AF}/c \approx 0.6$ and 0.8, respectively. This suggests that the spatial delay in DSV formation is proportional to the tubercle amplitude. Additionally, successful tracking of the DSV after $t^*=5$ for all three airfoils indicates that there is no temporal delay in DSV formation when the airfoil features tubercles. However, it is important to note that because the tubercles shift the DSV formation point downstream, the tubercled airfoils experience the consequences of the DSV for a shorter period of time. Highlight that the downstream shift in the DSV formation position has been consistently observed for different pitch-up motions ranging from k=0.05 to 0.1 and α_1=30° and 55°.

1.2. Do tubercles affect the strength of the DSV?

Due to their undulated shape, tubercles alter the vorticity dynamics during the growth stage of the DSV by reducing the amount of shed spanwise and increasing the amount of streamwise vorticity, expressed as counter-rotating pairs of vortices. This trade in vorticity moves the formation point of the DSV closer to the trailing-edge and reduces the overall spanwise vorticity available to form the DSV. Three-dimensional visualizations of spanwise vorticity clearly illustrate this phenomenon, showing that the troughs are the primary source of spanwise vorticity feeding into the system, with discontinuities representing the vorticity used to form the streamwise vortices.

The circulation of the DSV has been assessed by integrating the vorticity within its radius. The results reveal that the DSV of the smooth leading-edge airfoil consistently exhibits higher levels of circulation. Furthermore, there is a clear trend indicating that the larger the tubercle amplitude, the weaker the DSV, as observed from the circulation calculations and 3D vorticity iso-surfaces.

The impact of tubercles also extends to the pressure characteristics within the vortex cores. The baseline DSV, which is stronger and more cohesive as evidenced by both experimental and CFD data, exhibits the lowest pressure levels within its core, as confirmed by CFD pressure field analyses. This indicates a more pronounced impact on the aerodynamic forces. In contrast, with tubercled airfoils, the low-pressure core is observed to be weaker and more diffuse, reflecting a diminished aerodynamic influence. Emphasize that a consistent DSV circulation reduction has been observed when comparing the tubercled and smooth leading-edge airfoils across various pitch-up motions, spanning from $k = 0.05$ to 0.1, and at angles of attack $\alpha_1 = 30°$ and 55°.

1.3. Do tubercles alter the convection of the DSV?

Among the various DSV parameters evaluated, including formation position, strength, and convection, it seems that tubercles have the least impact on convection. Tracking of the DSV core using the Γ_1 method across the three airfoils indicates that the convection rate remains fairly similar in all cases. Nevertheless, as aforementioned in the first sub-question 1.1, the impact of tubercles on the DSV formation position, which is significantly closer to the trailing-edge compared to the baseline configuration, indeed affects the DSV trajectory relative to the airfoil. The DSV of the baseline airfoil remains over the airfoil's suction side for a longer duration. Additionally, when considering the airfoil's thickness, the DSV is positioned much closer to the suction side surface in the baseline configuration. This proximity results in a more pronounced influence of the DSV low-pressure core on the airfoil, enhancing its aerodynamic effects.

2. Is the stall compartmentalization mechanism still observable under dynamic stall conditions?

For the tubercled airfoil, the stall compartmentalization mechanism remains observable even under dynamic stall conditions. During the pitch-up motion, the troughs begin to exhibit reverse flow as a result of the upwash generated at these span locations by the counter-rotating pairs of vortices. As the DSV detaches from the leading-edge vorticity source, the separated regions reorganize to form so-called stall cells, typically showing a distance of λ^*/λ=2 between consecutive stall cells. Once the DSV has convected beyond the trailing-edge, the stall cells become well-defined, with clear attached

regions between them. Interestingly, while the position of the stall cells remains consistent during the pitch-up motion, it varies from cycle to cycle, suggesting that the formation of troughs where the cells originate has a random component. It is noteworthy that the baseline airfoil also exhibits stall cells; however, these cells tend to be larger and more unstable compared to those on the tubercled airfoil.

It has been observed that due to the large final angle of attack of the motions α_1=30°, the attached regions between stall cells have minimal impact on the total lift of the airfoil. Consequently, tubercled airfoils offer limited advantages in terms of lift in the deep stall regime. However, it is important to note that if the motion is to end at lower angles of attack still beyond the static stall angle of attack, the tubercled airfoils are expected to provide significantly higher lift levels compared to smooth leading-edge airfoils, as has already been observed in static scenarios. Essentially, in the deep stall regime, after the transient effects of the DSV have subsided, the known benefits of tubercles in static conditions can be applied.

3. What is the impact of the tubercle amplitude on dynamic stall mitigation?

From the previous research questions, it has been concluded that tubercles on airfoils impact the position at which the DSV forms, its strength, and its convection. These points can be summarized as follows:

- Tubercles shift the DSV formation position downstream closer to the trailing-edge, altering the timing and location of the aerodynamic disruptions caused by the DSV.
- Tubercles reduce the strength of the DSV consistently throughout its formation and convective phases, thereby diminishing the aerodynamic disturbances during dynamic stall.
- Although the DSV convection rate is not affected by the tubercles, the baseline DSV remains over the airfoil for a longer duration, influencing its aerodynamic performance for an extended period.
- The stall cells coexist with the DSV and are fully developed after the DSV has convected beyond the trailing-edge.

These factors lead to the conclusion that while the baseline airfoil experiences a stronger and more prolonged lift overshoot, the tubercled airfoils return faster to a conventional deep stall regime once the DSV has convected past the trailing-edge. In this regime, tubercles demonstrate their primary advantage by offering higher and more stable lift levels over time compared to smooth leading-edge airfoils. This observation has been further validated by the predicted aerodynamic forces from CFD simulations. Thus, it can be concluded that tubercles serve effectively as dynamic stall mitigation devices. They not only diminish the intensity and duration of lift overshoots but also enhance overall aerodynamic stability during dynamic stall conditions.

Comparing the A05L25 and A10L25 airfoils, the relationship between tubercle amplitude and alterations in the DSV appears somewhat linear. This suggests that increasing the amplitude of the tubercles proportionally affects the formation of the DSV and its characteristics. With greater tubercle amplitude, the DSV not only forms weaker but also further downstream, leading to a reduced and less intense lift overshoot, which effectively mitigates the effects of dynamic stall. Once the DSV has moved beyond the trailing-edge and the airfoil transitions into a deep stall regime, the tubercles facilitate stall compartmentalization, enhancing aerodynamic force stability. As the amplitude of the tubercles increases, the airfoil reaches the deep stall phase more rapidly, resulting in reduced fluctuations in the airfoil's aerodynamic forces.

5.1.2. Methodology

After exploring the research questions, it is imperative to critically assess the methodologies employed in this study. Initially, it was assumed that both experimental and computational approaches would be adequate to fulfill the objectives of the thesis and effectively address the research questions. Indeed, the combination of experimental and computational techniques used has provided a solid foundation for understanding the effect of the tubercles on dynamic stall. However, during the course of the research, it became evident that certain choices regarding the methodology introduced limitations and highlighted areas for potential improvement. Thus, this section aims to summarize and reflect on the adequacy and implications of the chosen research methods.

Experimental methodology
The experiments were conducted in a controlled environment using the W-Tunnel at the Aerodynamics Laboratory of TU Delft. This setup included a calibrated particle tracking system with four high-speed cameras, providing precise flowfield measurements. This technique effectively captured the main flowfield characteristic associated with the dynamic stall on airfoils and the tubercles. Particularly, for pitch-up and hold motions with reduced frequency ranging from k=0.05 to 0.1 and a maximum angle of attack between α_1=30° and 55°, the DSV has been successfully characterized with a time-resolution of 0.5 ms within a measurement volume of 180×120×300 mm^3.

The airfoil was positioned within the experimental flowfield using a Matlab image recognition approach that tracked white trackers painted on the airfoil. This method proved robust, even in high particle concentrations, provided that the airfoil and the wind tunnel wall opposite the cameras were painted black for contrast. This approach was crucial for accurately locating the flow structures relative to the airfoil, allowing preliminary hypotheses about the effects of the DSV and stall cells on aerodynamic forces even before analyzing the CFD force data.

Phase-averaging was used to smooth out the flowfield and accurately represent the dynamics of the DSV, especially during its formation and convection phases, where cycle repeatability was high for both smooth and tubercled airfoils. However, this approach was less effective during the DSV dissipation and breakdown phase, where cycle repeatability decreased significantly, and phase-averaging failed to represent actual vortex breakdown phenomena. Furthermore, phase-averaging was not justified when studying stall cells in the tubercled airfoil case, as their trough positions varied from cycle to cycle.

CFD methodology
The CFD simulations were configured to closely replicate the wind tunnel environment, capturing the flowfield characteristics of smooth leading-edge and tubercled airfoils. A high-quality hexahedral mesh was created using SnappyHexMesh, and a sliding mesh approach was employed to facilitate the airfoil rotation during the pitch-up motion. This setup was instrumental in accurately simulating both static and dynamic stall behaviors, maintaining the same setup for both scenarios.

The turbulence was modeled using the $k-\omega$ SST model, chosen for its robustness in predicting flow separation across various Reynolds numbers. Adjustments to the turbulence parameters were necessary to accurately predict separation at the baseline static stall angle of attack, α_{ss}=15°. Although these parameters were successfully tuned to match this specific condition, they were less effective at lower angles of attack. Overall, the turbulence model successfully replicated the experimental results. However, the predicted flowfield aligned with the phase-averaged experimental data, a result anticipated due to the limitations of URANS in capturing highly transient flow details.

A grid sensitivity analysis was performed to determine the optimal mesh density that balances computational expense with solution fidelity. For dynamic simulations, a time-step sensitivity study was conducted. Although complete time-step solution independence was not achieved, the chosen time-step ensured convergence of residuals and stability, while accurately representing the experimental flowfield.

The simulations were validated against PTV data, showing a high degree of agreement for both baseline and tubercled airfoils. This successful validation enhances confidence in the CFD simulations as a predictive tool for deriving aerodynamic forces of the airfoils, complementing the experimental results.

Γ_1 method for DSV tracking
The Γ_1 method, or Normalized Angular Momentum criterion, was emplyed for tracking the DSV in both experimental and CFD flowfields. This method was enhanced by incorporating an iterative mesh refinement approach, which was essential for accurately locating the center of the DSV.

This refined approach enabled precise quantification of the effects of tubercles on the DSV convective path and strength. Additionally, it proved invaluable in validating the CFD dynamic simulations by facilitating comparisons between the DSV trajectories derived from PTV and CFD data.

5.2. Recommendations

In the course of this research, all research questions have been addressed, yet it remains evident that certain areas could benefit from further elaboration. While the primary questions have been resolved, there is potential for deeper exploration to enhance the comprehensiveness of the presented findings. Consequently, the following recommendations are provided to guide future investigations.

Large Eddy Simulation (LES)

Although the CFD results are in good agreement with the phase-averaged experimental flowfield, transitioning from URANS (Unsteady Reynolds-Averaged Navier-Stokes) to LES (Large Eddy Simulation) represents a logical next step for the simulations. This change can bring significant advancements, particularly in capturing the complex and transient flow phenomena associated with dynamic stall events. Such improvements can deepen the understanding of flow separation, the dynamics of the DSV, and their interaction with tubercles, leading to more cohesive and comprehensive insights.

Measuring experimental aerodynamic forces

Aerodynamic forces were not measured during the experiments; instead, CFD simulations were used to investigate the impact of tubercles on lift overshoot and the subsequent lift levels in the deep stall regime. Future research should aim to develop a setup capable of measuring the forces experienced by the airfoil during dynamic motion. This task is challenging as it is essential to differentiate between actual aerodynamic forces and extraneous forces introduced by the mechanical setup. Such a distinction is critical due to potential "contamination" from mechanical vibrations or inertial effects, which can distort the measurement data. A comprehensive approach that integrates experimental force measurements with CFD simulations would not only enhance the validation of CFD models through direct aerodynamic forces comparison but also deepen the understanding of the dynamic stall phenomena on tubercled airfoils.

Effect of tubercles in the reattachment phase

Due to the characteristics of the motion employed in this research to study the formation and convection phases of the DSV, the reattachment phase has not been examined. Thus, the existing setup from the present research could be adapted to study airfoils undergoing sinusoidal pitching motions. This adjustment would allow for the evaluation of the tubercles' effect during the reattachment phase. The CFD methodology developed for this research is already able to handle sinusoidal motions; therefore, no further modifications would be required. Consequently, aerodynamic forces could be obtained to complement the experimental findings.

Large-scale experimental setup

One of the main limitations identified in the PTV data was the low resolution near the airfoil surface. Additionally, within the DSV core, the concentration of particles was considerably low. As a result, large spatial and temporal binning windows had to be employed. To address these issues, a larger airfoil model could be utilized while maintaining the same number of particles to fill the measurement volume. This change would enhance the resolution of the final flowfield since the spatial bins relative to the airfoil size would be smaller, yet still contain enough particles. This approach is now viable since it has been demonstrated that the development of the DSV is predominantly two-dimensional, eliminating the need to have the 12 tubercle wavelengths within the field of view as in the current experiments. Moreover, using a larger model offers two additional advantages: first, higher Reynolds numbers can be achieved with the same free-stream velocity; secondly, the same reduced frequency can be achieved with a lower pitching rate, resulting in more accurate motion, especially considering the current actuator's limited maximum acceleration.

Wavelength effect on dynamic stall

This research has evaluated the impact of tubercle amplitude for a fixed wavelength of λ/c=0.25. However, research on tubercles in static conditions has shown that for constant tubercle amplitudes, smaller wavelengths lead to higher maximum lift coefficients. Therefore, in the future, it could be interesting to include an airfoil with a smaller wavelength to evaluate the influence of this parameter.

Tapered finite-wing

The experiments and simultions were conducted using a full-span wing where tip effects are known to be negligible. It has been concluded that in this scenario, tubercles reduce the strength of the DSV, thus mitigating lift overshoot and its duration. However, it is important to note that humpback whale flippers deviate from this ideal scenario in several aspects. Firstly, because the flippers are finite, they are influenced by the tip vortex. Secondly, the flippers are tapered, significantly impacting stall evolution. In static conditions, this results in stall initiation at the wingtip due to its shorter chord, which then propagates inboard as the angle of attack increases. Tubercles are known to compartmentalize this stall, maintaining it close to the tip and therefore extending the operational envelope of the flipper, leading to increased maximum lift coefficients.

Understanding how tubercles would impact the DSV under these conditions remains uncertain and challenging to hypothesize based solely on the data obtained in the current research. It is recommended to apply the same CFD simulations and experimental setup to a wing resembling the idealized flipper shape used in previous research on tubercles in static conditions. This would aim to gain insight into the three-dimensional effects induced by the wingtip and their interaction with the DSV and streamwise vorticity generated by the tubercles.

Varied Motion Exploration

In this study, an experimental analysis of the effects of leading-edge tubercles on airfoil during dynamic stall evolution was conducted by inducing the formation of the DSV through a pitching up motion centered at the quarter chord position. For future research, it is recommended to explore the impact of changing the pitching axis to different positions along the airfoil. This adjustment will help determine whether the influence of the tubercles on aerodynamic performance remains consistent under varying dynamic conditions. Additionally, the investigation could be expanded to include flapping or plunging motions, which may offer further insights into the aerodynamic interactions under more complex motion regimes. However, incorporating these motions would likely increase the complexity of the actuators required to facilitate dynamic movements of the airfoil or wing. Evaluating these modifications could provide a deeper understanding of the potential applications and limitations of leading-edge tubercles in advanced aerodynamic designs.

References

Bangga, G., S. Hutani, and H. Heramarwan (2021). "The Effects of Airfoil Thickness on Dynamic Stall Characteristics of High-Solidity Vertical Axis Wind Turbines". en. In: *Advanced Theory and Simulations* 4.6, p. 2000204.

Bohl, D. G. and M. M. Koochesfahani (2009). "MTV measurements of the vortical field in the wake of an airfoil oscillating at high reduced frequency". en. In: *Journal of Fluid Mechanics* 620, pp. 63–88.

Bolzon, M. D., R. M. Kelso, and M. Arjomandi (2016). "Tubercles and Their Applications". en. In: *Journal of Aerospace Engineering* 29.1, p. 04015013.

Borg, J. (2012). "The Effect of Leading Edge Serrations on Dynamic Stall". en. PhD thesis. Southampton: University of Southampton, Faculty of Engineering and the Environment.

Butterfield, C. P., A. C. Hansen, D. Simms, and G. Scott (1991). "Dynamic Stall on Wind Turbine Blades". en. In: *Prepared for Windpower Conference and Exposition*. Palm Springs, California.

Cai, C., Z. G. Zuo, S. H. Liu, Y. L. Wu, and F. B. Wang (2013). "Numerical evaluations of the effect of leading-edge protuberances on the static and dynamic stall characteristics of an airfoil". en. In: *IOP Conference Series: Materials Science and Engineering* 52.5, p. 052006.

Cai, C., Z. Zuo, T. Maeda, Y. Kamada, Q. Li, K. Shimamoto, and S. Liu (2017). "Periodic and aperiodic flow patterns around an airfoil with leading-edge protuberances". en. In: *Physics of Fluids* 29.11, p. 115110.

Cai, C., Z. Zuo, M. Morimoto, T. Maeda, Y. Kamada, and S. Liu (2018). "Two-Step Stall Characteristic of an Airfoil with a Single Leading-Edge Protuberance". en. In: *AIAA Journal* 56.1, pp. 64–77.

Carr, L. W., K. W. Mcalister, and W. J. Mccroskey (1977). *Analysis of the development of dynamic stall based on oscillating airfoil experiments*. Tech. rep. A-6674. Washington, D. C: Ames Research Center and U.S. Army Air Mobility R&D Moffett Field.

Carreira Pedro, H. and M. Kobayashi (2008). "Numerical Study of Stall Delay on Humpback Whale Flippers". en. In: Reno, Nevada: American Institute of Aeronautics and Astronautics.

Chang, J., Q. Zhang, L. He, and Y. Zhou (2022). "Shedding vortex characteristics analysis of NACA 0012 airfoil at low Reynolds numbers". In: *Energy Reports*. 2021 International Conference on New Energy and Power Engineering 8, pp. 156–174.

Choudhry, A., M. Arjomandi, and R. Kelso (2014a). "Lift Curve Breakdown for Airfoil undergoing Dynamic Stall". en. In: *19th Australasian Fluid Mechanics Conference*. Melbourne, Australia.

Choudhry, A., R. Leknys, M. Arjomandi, and R. Kelso (2014b). "An insight into the dynamic stall lift characteristics". en. In: *Experimental Thermal and Fluid Science* 58, pp. 188–208.

Choudhuri, P. G. and D. D. Knight (1996). "Effects of compressibility, pitch rate, and Reynolds number on unsteady incipient leading-edge boundary layer separation over a pitching airfoil". en. In: *Journal of Fluid Mechanics* 308. Publisher: Cambridge University Press, pp. 195–217.

Conger, R. N. and B. R. Ramaprian (1994). "Pressure measurements on a pitching airfoil in a water channel". In: *AIAA Journal* 32, pp. 108–115.

Custodio, D. (2007). "The Effect of Humpback Whale-Like Leading Edge Protuberances on Hydrofoil Performance". en. PhD thesis. Worcester, Massachusetts: Worcester Polytechnic Institute.

Dellacasagrande, M., D. Barsi, D. Lengani, D. Simoni, and J. Verdoya (2020). "Response of a flat plate laminar separation bubble to Reynolds number, free-stream turbulence and adverse pressure gradient variation". en. In: *Experiments in Fluids* 61.6, p. 128.

Dropkin, A., D. Custodio, C. W. Henoch, and H. Johari (2012). "Computation of Flow Field Around an Airfoil with Leading-Edge Protuberances". en. In: *Journal of Aircraft* 49.5, pp. 1345–1355.

Du, X., T. Lee, F. Mokhtarian, and F. Kafyeke (2002). "Flow Past an Airfoil with a Leading-Edge Rotation Cylinder". en. In: *Journal of Aircraft* 39.6, pp. 1079–1084.

Ellington, C. P. (1999). "The novel aerodynamics of insect flight: applications to micro-air vehicles". In: *Journal of Experimental Biology* 202.23, pp. 3439–3448.

Elsinga, G. E., F. Scarano, B. Wieneke, and B. W. Van Oudheusden (2006). "Tomographic particle image velocimetry". en. In: *Experiments in Fluids* 41.6, pp. 933–947.

Ericsson, L. and J. Reding (1988). “Fluid mechanics of dynamic stall part I. Unsteady flow concepts”. en. In: *Journal of Fluids and Structures* 2.1, pp. 1–33.

Faleiros, D. E., M. Tuinstra, A. Sciacchitano, and F. Scarano (2019). “Generation and control of helium-filled soap bubbles for PIV”. en. In: *Experiments in Fluids* 60.3, p. 40.

Fallahpour, N., M. Mani, and M. Lorestani (2023). “Experimental investigation of vortex shedding of an airfoil at post-stall incidences”. en. In: *Proceedings of the Institution of Mechanical Engineers, Part G: Journal of Aerospace Engineering* 237.4. Publisher: IMECHE, pp. 883–898.

Fish, F. E. and J. J. Rohr (1999). *Review of Dolphin Hydrodynamics and Swimming Performance*. en. Tech. rep. 1801. Fort Belvoir, VA: Defense Technical Information Center.

Fish, F. E. (2020). “Biomimetics and the Application of the Leading-Edge Tubercles of the Humpback Whale Flipper”. en. In: *Flow Control Through Bio-inspired Leading-Edge Tubercles*. Cham: Springer International Publishing, pp. 1–39.

Fish, F. E. and J. M. Battle (1995). “Hydrodynamic design of the humpback whale flipper”. en. In: *Journal of Morphology* 225.1, pp. 51–60.

Gendrich, C. P. (1999). “Dynamic stall of rapidly pitching airfoils”. PhD thesis. Department of Mechanical Engineering: Michigan State University.

Ham, N. D. and M. S. Garelick (1968). “Dynamic Stall Considerations in Helicopter Rotors”. In: *Journal of the American Helicopter Society* 13.2, pp. 49–55.

Hansen, K. L., R. M. Kelso, and B. B. Dally (2009). “The effect of leading edge tubercle geometry on the performance of different airfoils”. en. In: *ExHFT-7 : 7th World Conference on Experimental Heat Transfer, Fluid Mechanics and Thermodynamics*. Krakow, Poland.

Hansen, K. L. (2012). “Effect Of Leading Edge Tubercles On Airfoil Performance”. en. PhD thesis. Adelaide, South Australia: University of Adelaide.

Holzmann, T. (2016). *Mathematics, Numerics, Derivations and OpenFOAM®*. 4th ed. Leoben.

Hrynuk, J. T. and D. G. Bohl (2020). “The effects of leading-edge tubercles on dynamic stall”. en. In: *Journal of Fluid Mechanics* 893, A5.

Johari, H., C. Henoch, D. Custodio, and A. Levshin (2007). “Effects of Leading-Edge Protuberances on Airfoil Performance”. en. In: *AIAA Journal* 45.11, pp. 2634–2642.

Jumper, E., S. Schreck, and R. Dimmick (1987). “Lift-curve characteristics for an airfoil pitching at constant rate”. en. In: *Journal of Aircraft* 24.10, pp. 680–687.

Jurasz, C. M. and V. P. Jurasz (1979). “Feeding modes of the humpback whale, Megaptera novaeangliae, in southeast Alaska”. In: *Scientific Reports of the Whales Research institute* 31, pp. 69–83.

Kiefer, J., C. E. Brunner, M. O. Hansen, and M. Hultmark (2022). “Dynamic stall at high Reynolds numbers induced by ramp-type pitching motions”. en. In: *Journal of Fluid Mechanics* 938, A10.

Kim, H., J. Kim, and H. Choi (2018). “Flow structure modifications by leading-edge tubercles on a 3D wing”. en. In: *Bioinspiration & Biomimetics* 13.6, p. 066011.

Koochesfahani, M. M. and V. Smiljanovski (1993). “Initial acceleration effects on flow evolution around airfoils pitching to high angles of attack”. In: *American Institute of Aeronautics and Astronautics* 31.8, pp. 1529–1531.

Kramer, M. (1932). *Increase in the maximum lift of an airplane wing due to a sudden increase in its effective angle of attack resulting from a gust*. en. Tech. rep. 678. Washington, D.C.: National committee for aeronautics.

Leknys, R. R., M. Arjomandi, R. M. Kelso, and C. Birzer (2016). “Dynamic Stall on Airfoils Exposed to Constant Pitch-Rate Motion”. en. In: *20th Australasian Fluid Mechanics Conference*. Perth, Australia.

Lin, J. C. (2002). “Review of research on low-profile vortex generators to control boundary-layer separation”. en. In: *Progress in Aerospace Sciences* 38.4-5, pp. 389–420.

Liu, H., S. Wang, and T. Liu (2024). “Vortices and Forces in Biological Flight: Insects, Birds, and Bats”. en. In: *Annual Review of Fluid Mechanics* 56.1, pp. 147–170.

Lorber, P. F. and F. O. Carta (1987). “Airfoil dynamic stall at constant pitch rate and high Reynolds number”. en. In: *Journal of Aircraft* 25.6, pp. 548–556.

McAlister, K. W. and L. W. Carr (1979). “Water Tunnel Visualizations of Dynamic Stall”. In: *Journal of Fluids Engineering* 101.3, pp. 376–380.

McCroskey, W. J. (1981). *The phenomenon of dynamic stall*. Tech. rep. A-8464. Moffett Federal Airfield, Mountain View: Ames Research Center.

McCroskey, W. J. (1982). “Unsteady Airfoils”. In: *Annual Review of Fluid Mechanics* 14, pp. 285–311.

McCroskey, W. J., K. W. McAlister, L. W. Carr, S. L. Pucci, O. Lambert, and R. F. Indergrand (1981). "Dynamic Stall on Advanced Airfoil Sections". en. In: *Journal of the American Helicopter Society* 26.3, pp. 40–50.

Melling, A. (1997). "Tracer particles and seeding for particle image velocimetry". en. In: *Measurement Science and Technology* 8.12, p. 1406.

Michard, M., L. Graftieaux, L. Lollini, and N. Grosjean (1997). "Identification of Vortical Structures by a Non-Local Criterion - Application of PIV Measurements and DNS-LES Results of Turbulent Rotating Flows." en. In: *11th Symposium on Turbulent Shear Flows*. Grenoble, France.

Miklosovic, D. S., M. M. Murray, L. E. Howle, and F. E. Fish (2004). "Leading-edge tubercles delay stall on humpback whale (*Megaptera novaeangliae*) flippers". en. In: *Physics of Fluids* 16.5, pp. 39–42.

Miklosovic, D. S., M. M. Murray, and L. E. Howle (2007). "Experimental Evaluation of Sinusoidal Leading Edges". en. In: *Journal of Aircraft* 44.4, pp. 1404–1408.

Mueller, T. (2000). *Aerodynamic Measurements at Low Raynolds Numbers for Fixed Wing Micro-Air Vehicles*. en. Tech. rep. ADP010760. Section: Technical Reports. Notre Dame University.

Mulleners, K. and M. Raffel (2012). "The onset of dynamic stall revisited". en. In: *Experiments in Fluids* 52.3, pp. 779–793.

Mulleners, K. and M. Raffel (2013). "Dynamic stall development". en. In: *Experiments in Fluids* 54.2, p. 1469.

Nayman, M. N. and R. E. Perez (2022). "Improving Dynamic Stall Effects Using Leading Edge Tubercles". en. In: *AIAA AVIATION 2022 Forum*. Chicago, IL & Virtual: American Institute of Aeronautics and Astronautics.

Raffel, M., C. E. Willert, F. Scarano, C. J. Kähler, S. T. Wereley, and J. Kompenhans (2018). *Particle Image Velocimetry: A Practical Guide*. en. Cham: Springer International Publishing.

Reynolds, W. C. and L. W. Carr (1985). "Review of Unsteady, Driven, Separated Flows". In: *Shear Flow Control Conference*. Shear Flow Conference. American Institute of Aeronautics and Astronautics.

Rival, D. and C. Tropea (2010). "Characteristics of Pitching and Plunging Airfoils Under Dynamic-Stall Conditions". In: *Journal of Aircraft* 47.1, pp. 80–86.

Rohmawati, I., H. Arai, T. Nakashima, H. Mutsuda, and Y. Doi (2020). "Effect of Wavy Leading Edge on Pitching Rectangular Wing". In: *Journal of Aero Aqua Bio-mechanisms* 9.1, pp. 1–7.

Rostamzadeh, N., K. L. Hansen, R. M. Kelso, and B. B. Dally (2014). "The formation mechanism and impact of streamwise vortices on NACA 0021 airfoil's performance with undulating leading edge modification". en. In: *Physics of Fluids* 26.10, p. 107101.

Salam, M. A., M. T. Ali, and M. Q. Islam (2020). "Experimental Analysis of Aerodynamic Performance on asymmetric NACA 23018 Aerofoil incorporating a Leading-Edge Rotating Cylinder". en. In: *3rd International Conference on Advances in Mechanical Engineering (ICAME 2020)*. Vol. 912. Chennai, India, p. 042027.

Schanz, D., S. Gesemann, and A. Schröder (2016). "Shake-The-Box: Lagrangian particle tracking at high particle image densities". en. In: *Experiments in Fluids* 57.5, p. 70.

Segre, P. S., S. M. Seakamela, M. A. Meÿer, K. P. Findlay, and J. A. Goldbogen (2017). "A hydrodynamically active flipper-stroke in humpback whales". en. In: *Current Biology* 27.13, R636–R637.

Shipley, D. E., M. S. Miller, and M. C. Robinson (1995). *Dynamic stall occurrence on a horizontal axis wind turbine blade*. English. Tech. rep. NREL/TP-442-6912; CONF-950116-8. Golden, Colorado: National Renewable Energy Lab. (NREL).

Shyy, W., Y. Lian, J. Tang, D. Viieru, and H. Liu (2007). *Aerodynamics of Low Reynolds Number Flyers*. en. 1st ed. New York: Cambridge University Press.

Sudhakar, S., N. Karthikeyan, and P. Suriyanarayanan (2019). "Experimental Studies on the Effect of Leading-Edge Tubercles on Laminar Separation Bubble". en. In: *AIAA Journal* 57.12, pp. 5197–5207.

Taylor, K. and M. Amitay (2016). "A Statistical Approach to the Identification of Vortical Structures During Dynamic Stall with Flow Control". In: *54th AIAA Aerospace Sciences Meeting*. AIAA SciTech Forum. American Institute of Aeronautics and Astronautics.

Van Nierop, E. A., S. Alben, and M. P. Brenner (2008). "How Bumps on Whale Flippers Delay Stall: An Aerodynamic Model". en. In: *Physical Review Letters* 100.5, p. 054502.

Visbal, M. and J. Shang (1989). “Investigation of the Flow Structure Around a Rapidly Pitching Airfoil”. In: *Aiaa Journal - AIAA J* 27, pp. 1044–1051.

Visbal, M. R. and D. J. Garmann (2018). “Analysis of Dynamic Stall on a Pitching Airfoil Using High-Fidelity Large-Eddy Simulations”. en. In: *AIAA Journal* 56.1, pp. 46–63.

Wahba, G. (1965). “A Least Squares Estimate of Satellite Attitude”. In: *SIAM Review* 7.3. Publisher: Society for Industrial and Applied Mathematics, pp. 409–409.

Walker, J., H. Helin, and D. Chou (1985). “Unsteady Surface Pressure Measurements on a Pitching Airfoil”. en. In: *AIAA Shear Flow Control Conference*. Boulder, Colorado: F.J. Seiler Research Laboratory USAF Academy.

Wang, Y.-y., W.-r. Hu, and S.-d. Zhang (2014). “Performance of the bio-inspired leading edge protuberances on a static wing and a pitching wing”. en. In: *Journal of Hydrodynamics* 26.6, pp. 912–920.

Weber, P. W., L. E. Howle, and M. M. Murray (2010). “Lift, Drag, and Cavitation Onset On Rudders With Leading-edge Tubercles”. en. In: *Marine Technology and SNAME News* 47.01, pp. 27–36.

Weber, P. W., L. E. Howle, M. M. Murray, and D. S. Miklosovic (2011). “Computational Evaluation of the Performance of Lifting Surfaces with Leading-Edge Protuberances”. en. In: *Journal of Aircraft* 48.2, pp. 591–600.

Wu, L. and X. Liu (2021). “Dynamic Stall Characteristics of the Bionic Airfoil with Different Waviness Ratios”. en. In: *Applied Sciences* 11.21, p. 9943.

Yasuda, T., K. Fukui, K. Matsuo, H. Minagawa, and R. Kurimoto (2019). “Effect of the Reynolds Number on the Performance of a NACA0012 Wing with Leading Edge Protuberance at Low Reynolds Numbers”. en. In: *Flow, Turbulence and Combustion* 102.2, pp. 435–455.

Zhang, M. M., G. F. Wang, and Xu (2014). “Experimental study of flow separation control on a low-Re airfoil using leading-edge protuberance method”. en. In: *Experiments in Fluids* 55.4, p. 1710.

Zhang, X. and J. U. Schlüter (2012). “Numerical study of the influence of the Reynolds-number on the lift created by a leading edge vortex”. en. In: *Physics of Fluids* 24.6, p. 065102.